Universidade de Aveiro
2017

Departamento de Engenharia de Materiais e Cerâmica

André Pereira dos Santos

Strain Effect on the Properties of $K_{0.5}Na_{0.5}NbO_3$ Films

Efeito das Tensões nas Propriedades de Filmes de $K_{0.5}Na_{0.5}NbO_3$

Universidade de Aveiro
2017

Departamento de Engenharia de Materiais e Cerâmica

André Pereira dos Santos

Strain Effect on the Properties of $K_{0.5}Na_{0.5}NbO_3$ Films

Efeito das tensões nas propriedades de filmes de $K_{0.5}Na_{0.5}NbO_3$

Dissertação apresentada à Universidade de Aveiro para cumprimento dos requisitos necessários à obtenção do grau de Mestre em Engenharia de Materiais, realizada sob a orientação científica do Doutor Oleksandr Tkach, Investigador Auxiliar do Departamento de Engenharia de Materiais e Cerâmica da Universidade de Aveiro.

Dissertation presented to the University of Aveiro to fulfil the requirements necessary for the awarding of the degree of Master in Materials Engineering, carried out under the scientific guidance of Doctor Oleksandr Tkach, Auxiliary Researcher of the Department of Materials and Ceramics Engineering of the University of Aveiro.

o júri

presidente

Prof. Doutor Pedro Manuel Lima de Quintanilha Mantas

Professor Auxiliar da Universidade de Aveiro

Prof. Doutor José Ramiro Afonso Fernandes

Professor Auxiliar da Universidade de Trás-os-Montes e Alto Douro

Doutor Oleksandr Tkach

Investigador Auxiliar da Universidade de Aveiro

Acknowledgments

I am mostly grateful to my supervisor Dr. Oleksandr Tkach for his support, wisdom and guidance during this work.

I would like to thank the staff members of the University: Professor Paula Vilarinho, Professor Elisabete Costa, Artur Sarabando, Ana Ribeiro, Célia Miranda, Marta Ferro, Tiago Vieira da Silva, Jacinto Alves, Octávio Contente, Luísa Costa, Dr. Rosário Soares, Dr. Igor Bdikin and Dr. Olena Okhay for their effort and sympathy.

I am very grateful to all my colleagues: Pedro Duarte, Pedro Marques, Manuela Fernandes, Ricardo Serrazina, Alexandre Santos, Marta Branco, Inês Oliveira and João Carvalheiras for their positive attitude, friendly working environment and for their skills and knowledge which help me in difficult times.

I would like to thank to Dr. Sebastian Zlotnik for his time, patience and his kind guidance during this work.

I am also very grateful to all my friends who have listened, supported and gave me strength in hard times. To all of them: thank you!

Por fim, gostaria de agradecer aos meus pais e à Carolina Viceto por todo o suporte e confiança depositados em mim ao longo de todos estes anos. Definitivamente sem eles não seria possível para mim apresentar este trabalho hoje. Muito obrigado por tudo.

André Pereira dos Santos
Aveiro, Portugal

palavras-chave

Niobato de sodio e potassio, $K_{0.5}Na_{0.5}NbO_3$, KNN, filmes, caracterização estrutural, tensões da rede, propriedades dieléctricas e ferroelectricas

resumo

Este trabalho é sobre materiais cerâmicos isentos de chumbo destinados a aplicações electromecânicas e candidatos à substituição de electrocerâmicos à base de chumbo.

O titanato zirconato de chumbo (PZT) é o cerâmico piezoeléctrico mais utilizado em todo o mundo. No entanto, contém mais de 60 % de chumbo que é um elemento tóxico para os seres humanos e para o ambiente. Em 2003, a União Europeia aprovou uma directiva que proíbe e restringe o uso de elementos potencialmente perigosos, tais como o chumbo. Devido à inexistência de materiais aptos para a substituição do PZT, foi feita uma exceção até ser encontrado um material alternativo competitivo.

O niobato de potássio e sódio (KNN), devido à sua elevada temperature de Curie e propriedades piezoeléctricas moderadas, é um dos materiais isentos de chumbo mais promissores para substituição do PZT. No entanto, a sua efetiva adopção industrial requer, entre outros aspectos, a optimização das suas propriedades.

A maioria da literatura está focada em materiais cerâmicos densos com base em KNN. Recentemente, os filmes de KNN receberam bastante atenção, pois é uma das alternativas mais promissoras para várias aplicações, como por exemplo, sensores, atuadores, sistemas de colheita de energia e sistemas microelectromecânicos (MEMS). Essa atenção deve-se às altas propriedades piezoelétricas nas suas contrapartidas cerâmicas. No entanto, duas questões principais ainda impedem a fabricação de filmes de KNN de alta qualidade: tensão exercida entre o filme de KNN e o substrato e a perda de óxidos alcalinos durante a sua preparação.

Neste contexto, este trabalho tem como objectivo o estudo da influência de tensões existentes nos filmes de KNN nas propriedades elétricas.

Para este fim, filmes de KNN com i) 20% de excesso de potássio e sódio e uma concentração molar de 0,4; ii) 20% de excesso de potássio e sódio e concentração molar de 0,2; iii) 5% de potássio com concentração molar de 0,4 e iv) 5% de potássio e concentração molar de 0,2 foram depositados em substratos de Si/SiO_2, $Al2O_3$ policristalino, $Si/SiO_2/TiO_2/Pt$, Al_2O_3/Pt e $SrTiO_3/Pt$.

Verificou-se que os filmes finos de KNN têm uma estrutura perovskita sem fases secundárias. Os filmes finos de KNN com 20% de excesso de potássio e sódio depositado nos substratos de Al_2O_3/Pt e $SrTiO_3/Pt$ mostram uma orientação preferencial ao longo do pico (100), tendo um fator de Lottering maior que 38% (f_{100}> 38%).

Os filmes finos de KNN depositados nos substratos de $Si/SiO_2/TiO_2/Pt$ encontram-se sob uma tensão de tracção, enquanto que os filmes finos de KNN depositados nos substratos de $SrTiO_3/Pt$ e Al_2O_3/Pt estão sob uma tensão compressiva.

Entre os filmes finos de KNN com 20% de excesso de potássio e sódio e concentração de 0,2 M, o filme que apresenta a permitividade mais elevada (ε' = 585 (10 kHz) with $tan\delta$ = 0.182) é filme depositado no subtrato de $SrTiO_3/Pt$ e o filme depositado em $Si/SiO_2/TiO_2/Pt$ é o que apresenta as perdas mais baixas (ε' = 382 (10 kHz) com $tan\delta$ = 0,093). O ultimo filme, apresenta valores de polarização remanescente mais elevados (P_r = 9,57 μC/cm^2 (a 50 Hz) com E_c = 36 kV/cm). Os filmes finos de KNN com 5% de excesso de potássio com uma concentração molar de 0,2 têm o P_r mais elevado nos filmes depositados nos substratos de $SrTiO_3/Pt$ (P_r = 4,55 μC/cm^2 (a 50 Hz) com E_c = 34 kV/cm). Os filmes depositados em Al_2O_3/Pt têm a menor permitividade e polarização moderada, mas são os que mais sustentam altos campos elétricos, mostrando "loops" de histerese quadrados.

As imagens de PFM mostram que os filmes finos de KNN com uma concentração molar de 0,4 depositados nos substratos de Al_2O_3/Pt e $SrTiO_3/Pt$ têm domínios bem definidos, com um tamanho médio que varia entre os 75 e os 100 nm, sendo separados por paredes com um domínio de 180º. Para os filmes com uma concentração molar de 0,2, são observados domínios com escala micrométrica e obtidas curvas de histerese piezoeléctricas locais.

Os resultados deste estudo contribuem definitivamente para o conhecimento no campo dos materiais piezoelétricos sem chumbo.

keywords

Potassium sodium and niobate, $K_{0.5}Na_{0.5}NbO_3$, KNN, films, structural caracterization, strain/stress, dielectric and ferroelectric properties.

abstract

This work is about lead-free piezoelectric materials intended for electromechanical and energy harvesting applications.

One of the most widely used piezoelectric ceramics is lead zirconate titanate (PZT). However, it contains more than 60% of lead that is toxic for humans and environment. In 2003, a directive from European Union has prohibited the use of potentially hazardous elements as lead. Due to the lack of competitive materials for PZT replacement an exception was created until a competitive alternative be found.

Potassium and sodium niobate (KNN) due to its high Curie temperature and moderate piezoelectric properties is currently one of the most promising lead-free materials for PZT substitution. However, its effective industrial adoption requires, among others, optimization of its properties.

Most literature is focused on KNN-based bulk materials. Recently, KNN based films have received more attention as one of the promising alternatives in various applications, such as sensors, actuators, energy harvesting systems and microelectromechanical systems (MEMS). This attention is due to the high piezoelectric properties in their bulk counterparts. However, two main issues still inhibit the fabrication of high-quality KNN-based films: stress/strain exerted between the KNN film and the substrate and the loss of alkali oxides during its preparation.

In this context, in this work the influence of stress/strain applied to KNN films on the electrical properties is studied.

For this purpose, KNN films with i) 20% excess of potassium and sodium and 0.4 M concentration, ii) 20% excess of potassium and sodium and 0.2 M concentration, iii) 5% of potassium and 0.4 M concentration and iv) 5% of potassium and 0.2 M concentration were deposited on: Si/SiO_2, polycrystalline Al_2O_3, $Si/SiO_2/TiO_2/Pt$, Al_2O_3/Pt and $SrTiO_3/Pt$ substrates.

It was found that KNN thin films have a perovskite structure without secondary phases. KNN thin films with 20% excess of potassium and sodium deposited on Al_2O_3/Pt and $SrTiO_3/Pt$ substrates show a preferential orientation along (100) direction and have Lottering factor higher than 38% ($f_{100} > 38\%$).

KNN thin films deposited on $Si/SiO_2/TiO_2/Pt$ substrates are found to be under a tensile strain, while the KNN films deposited on $SrTiO_3/Pt$ and Al_2O_3/Pt substrates are under a compressive strain.

Among the KNN thin films with 20% excess of potassium and sodium and 0.2 M concentration, the film that show the highest permittivity (ε´ = 585 (10 kHz) with *tanδ* = 0.182) is that on $SrTiO_3$/Pt, while the one deposited on Si/SiO_2/TiO_2/Pt substrate possesses the lowest losses (ε´ = 382 (10 kHz) with *tanδ* = 0.093). The later film shows as well the highest values of remnant polarization (P_r = 9.57 μC/cm^2 (at 50 Hz) with E_c = 36 kV/cm). However, the KNN thin films with 5% excess of potassium and 0.2 M concentration that has the highest P_r is the film deposited on $SrTiO_3$/Pt substrates (P_r = 4.55 μC/cm^2 (at 50 Hz) with E_c= 34 kV/cm). The films deposited on Al_2O_3/Pt have the lowest permittivity and moderate polarization, but they are the most sustainable to high electric field, showing square-like hysteresis loops.

The PFM images shows that the KNN thin films with 0.4 M concentration deposited on $SrTiO_3$/Pt and Al_2O_3/Pt substrates have well defined domains with average size between 75 and 100 nm, separated by 180^o domain walls. For the films with 0.2 M concentration micrometre scale domains are observed and local piezoelectric loops are obtained.

The results of this study definitely contribute to the knowledge in the field of lead-free piezoelectric materials.

Table of Contents

Table of Figures

List of Tables

List of Symbols

A - Area

a_{film} - Lattice parameter of film

$a_{substrate}$ - Lattice parameter of substrate

C - Curie constant

C_p - Capacitance of parallel plate capacitor

d - Space between the planes (lattice spacing)

d_{ψ} - Lattice spacing for each ψ

D - Electric displacement field

d - Piezoelectric coefficient

d_{33} - Longitudinal piezoelectric coefficient

E - Electric field

E_c - Coercive electric field

E_Y - Young's modulus

e_{31} - Transverse coefficient

g - Piezoelectric voltage constant

hkl - Miller indices

k_{ij} - Electromechanical coupling factor

OR - Reactive alkoxy group

$\vec{P}$ - Polarization

P_r - Remnant polarization

P_S - Spontaneous polarization

$\vec{p}$ - Dipole moment

p - Pyroelectric coefficient

T - Temperature

$tan\delta$ - Dielectric loss or dissipation factor

T_C - Curie temperature

t - Thickness

V - Volume

α_{film} - Thermal expansion coefficient (TEC) of film

$\alpha_{substrate}$ - Thermal expansion coefficient (TEC) of substrate

ε_r - Relative dielectric permittivity

ε_0 - Dielectric permittivity of vacuum (8.854×10^{-12} F/m)

ε_r - Real part of dielectric permittivity

ε'' - Imaginary part of dielectric permittivity

ε - Mechanical strain

θ - Diffraction angle

λ - Wavelength

v - Poisson ratio

ξ - Electrostrictive coefficient

π - Constant (3.1416)

σ - Mechanical stress

σ_{th} - Thermal stress

ϕ - Thermodynamic potential

ψ - Angle 90°-δ

ω - Angular frequency

List of Abbreviations

AC - Alternating Current

AFM – Atomic Force Microscopy

BT - Barium Titanate

CVD - Chemical Vapour Deposition

DC - Direct Current

E_C – Coercive Electric Field

HIP - Hot Isostatic Pressing

HP - Hot Pressing

KN - Potassium Niobate

KNN - Potassium Sodium Niobate

MEMS - Micro-Electro-Mechanical Systems

MPB - Morphotropic Phase Boundary

NBT - Sodium Bismuth Titanate

NN - Sodium Niobate

PFM – Piezoelectric Force Microscopy

PVD - Physical Vapour Deposition

PZT - Lead Zirconate Titanate

RMS- Root Mean Square

RTA - Rapid Thermal Annealing

RoHS - Restriction of Hazardous Substances

RT - Room Temperature

SEM - Scanning Electron Microscopy

TEC - Thermal Expansion Coefficient

XRD - X-Ray Diffractometry

1. Introduction

1.1. Motivation

Piezoelectricity was discovered by Pierre and Jaques Curie in 1880, in Rochelle salt, quartz and other minerals. Over the ages, synthesized piezoelectrics have been used in several applications, such as ultra-sonic transducers, filters, piezoelectric sonars, ultrasound imaging equipment and inkjet printers.

The lead based materials have outstanding dielectric, ferroelectric and piezoelectric properties. Thus, lead zirconate titanate $Pb(Zr_{1-x}Ti_x)O_3$, commonly called as PZT, is one of the most extensively used piezoelectric ceramics [1]. PZT is one of the reference materials for Micro-Electro-Mechanical Systems (MEMS) applications, like micro-electronic and micro- or even nano-technologic electrostrictive actuators, transducers and sensors. However, PZT contains more than 60 wt. % of lead, which is a toxic element for environment. Moreover, weighty elements such as lead are extremely toxic for humans. Indeed, lead is so poisonous when absorbed into the body, that it can contaminate many organs and tissues like the heart, bones, and nervous systems [2][3][4]. For this important reason, worldwide research is now focusing on synthesis and complete characterisation of alternative lead free materials. With the purpose to protect the human health, as well as the environment, the European Union passed the Restrictions of Hazardous Substances (RoHS) law, in 2003, whereas “Household Electronic Products Recycling Law” was passed in Japan and the “Electronic Information Product Pollution Control Management Regulation” was established in China, in 2006. Similar regulations were also planned or established in North America and Korea. However, due to the inexistence of a viable material for PZT substitution, European Union made an exception in the RoHS law for PZT until a competitive alternative can be found. Alkali niobates, among the lead-free ceramics under investigation, are described as one the most promising family of compounds (Figure 1) [3][5]. $K_{0.5}Na_{0.5}NbO_3$ (KNN) became one of the most extensively investigated piezoelectrics due to its high Currie temperature (T_C) up to 420°C and owing to its high longitudinal piezoelectric coefficient (d_{33}) reported by *Saito et al.* in 2004 [6].

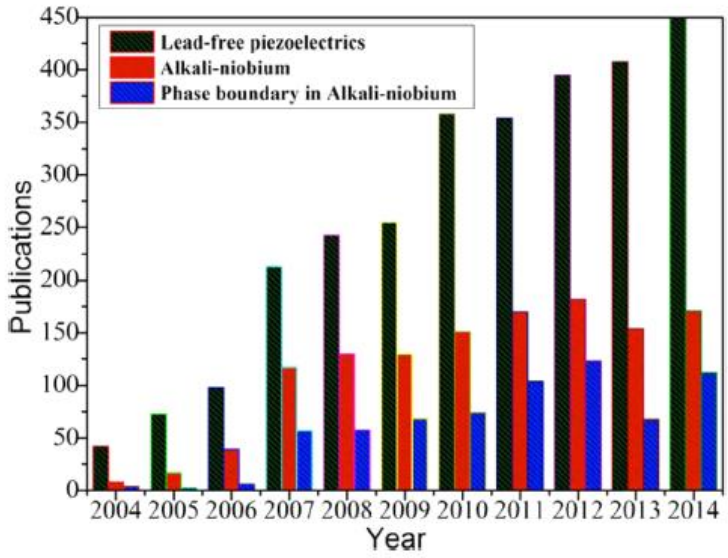

Figure 1- Publications on lead-free piezoceramics in refereed journals for the time range from 2004 to 2014 [4].

The best properties were obtained by Saito *et al.* (2004) [6] in $(K_{0.44}Na_{0.52}Li_{0.04})(Nb_{0.84}Ta_{0.10}Sb_{0.06})O_3$ textured ceramics fabricated using reactive templated grain growth method. These ceramics have a d_{33} value of 416 pC/N that is similar to the d_{33} of some PZT compositions [4][6][7]. *Shrout* and *Zhang* (2007) reported KNN as the most promising among the lead-free materials. Further research and development is necessary to turn KNN economically practicable. Moreover, it is necessary to improve the properties of KNN to make them superior to the electromechanical performance of PZT. The implementation of KNN in practical applications will rely on political actions [7].

1.2. Objectives

The aim of this dissertation is to understand whether the strain/stress induced in potassium sodium niobate (KNN) thin films, deposited on different substrates, influences their electrical properties. Thus, the microstructure of sol-gel derived KNN thin films without secondary phases was engineered by combining the use of different amounts of excess of potassium and sodium, to achieve a reduced number of cracks, which are known to prevent the electrical characterization.

2. State of the art

2.1. Dielectrics

Dielectric and insulator materials are characterized by a large electric resistivity [8][9][10]. An insulator is a material, which does not have the ability to conduct electricity due to the absence of free electric changes. Dielectrics do not conduct electricity as well, due to the very low density of free charge carriers, consequently they can perform insulating functions. However, dielectrics can exhibit also an ability to store charge in a capacitor, which is related to the polarization of the dielectrics under the electric field. When the electric field is applied to dielectrics, there is no long-distance charge transportation, but only a displacement of the positive and negative charge centres in small range, which causes the appearance of the electric dipole moments in the material. This phenomenon is known as polarization and is characteristic for dielectrics only.

Polarization ($\vec{P}$) can be defined as the total of all dipole moments ($\vec{p}$) per unit volume (V) and is demonstrated as:

$$\vec{P} = \frac{\sum_i \vec{p}}{V} \qquad \text{Equation 1}$$

Within a dielectric material several polarization mechanisms can occur, namely atomic, dipolar, ionic and space charge polarization [9][10][11]. Concluding, all dielectric materials are insulators but not all insulators are dielectric materials.

When dielectric material is placed between the plates of a capacitor, capacitance increases by a factor equal to the relative permittivity (ε_r) of the dielectric. The ε_r value can be obtained considering the sample thickness (t) and the area of the plates (A) according to:

$$\varepsilon_r = \frac{C_P t}{\varepsilon_0 A} \qquad \text{Equation 2}$$

where C_p is the capacitance of the parallel plane capacitor and ε_0 is the dielectric permittivity in vacuum or electric constant (8.85×10^{-12} F/m).

When the dc electric field (E_{dc}) is applied to the dielectric material, the charge displacements will provoke also a small change in the material dimensions. If the resultant stain (ε) is proportional to the square of the field, and can be described by [9][11]:

$$\varepsilon = \xi {E_{dc}}^2 \qquad \text{Equation 3}$$

where ξ is the electrostrictive coefficient, the effect is called electrostriction.

2.2. Piezoelectricity

Jacques and Pierre Curie discovered piezoelectricity in 1880, in Rochelle salt ($(KNaC_4H_4O_6 \cdot 4H_2O)$), quartz and other minerals. When certain crystalline minerals are subjected to a mechanical force, the crystal was found to become electrically polarized. Two effects are operative in piezoelectric materials. The direct effect (called as generator) is the phenomenon whereby electric charge (polarization) is generated from a mechanical stress, on the contrary, converse effect (designated as motor) is related to the mechanical movement generated by the application of an electric field [8]. Both effects are illustrated in Figure 2:

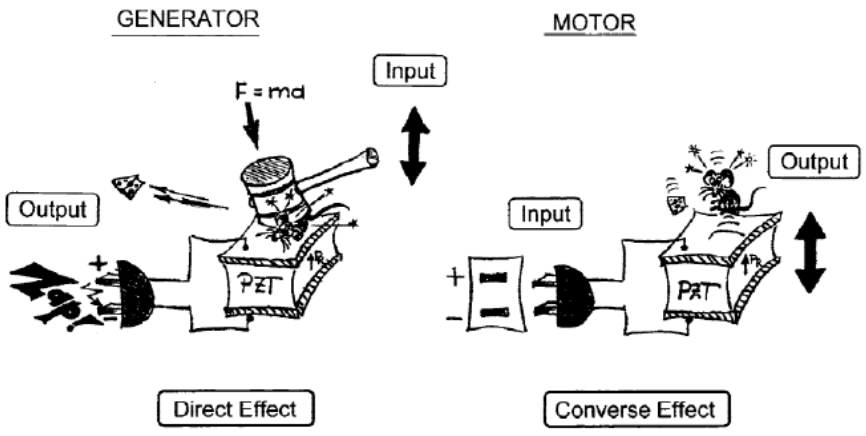

Figure 2- Illustration of the direct and converse piezoelectric effects [8]**.**

Direct effect occurs when a piezoelectric exhibits a finite polarization value, provided by a mechanical stress. The result is a polarization *P* proportional to this stress, which is described by Equation 4:

$$P \approx D = d\sigma \qquad \text{Equation 4}$$

where *D* is the electric displacement field, *d* is the piezoelectric coefficient and *σ* is the mechanical stress.

The converse effect is described by an electric field applied to a piezoelectric, generating a mechanical strain, which is proportional to the applied electric field. This effect is explained by Equation 5:

$$\varepsilon = dE_{dc} \qquad \text{Equation 5}$$

where *ε* is the mechanical strain, *d* is the piezoelectric coefficient and E_{dc} is the dc electric field. Thus, the piezoelectric coefficient, *d*, is the proportionality between the applied stimulus and the behaviour of the material. This coefficient has the same value for the direct and converse effects, which is extremely important in order to compare piezoelectric responses of materials. For materials that use vibrational devices, such as sonar and sounders, high *d* coefficients are desirable. The d_{33} is the most reported coefficient for piezoelectric measurements both for direct and converse effects.

In addition to *d* coefficients, another coefficient, *g*, is used to evaluate the ability of piezoelectric ceramics to generate voltage per unit of input stress. The *g* constant is related to the *d* constant, as it is shown in Equation 6 :

$$g = \frac{d}{\varepsilon_r \times \varepsilon_0} \qquad \text{Equation 6}$$

where ε_r is the relative dielectric permittivity, *d* is the piezoelectric coefficient and ε_0 is the dielectric permittivity in vacuum [11]. High *g* constant ceramics are normally related to ferroelectrically hard materials, which do not switch their polarization and can possess lower ε_r values. They are used in devices such as portable gas igniters [8].

2.3. Pyroelectricity

Pyroelectrics are materials that can exhibit spontaneous polarization due to their non-centro-symmetric structure, which has a strong dependence on temperature since the dipole moments vary accordingly to the crystal expansion or contraction. Therefore, an electric potential can be produced across a pyroelectric crystal when it is subjected to a small charge in temperature [12]. The pyroelectric effect is described by Equation 7:

$$P_s = pT \qquad \text{Equation 7}$$

where P_S is the spontaneous polarization, p is the pyroelectric coefficient and T is the temperature.

2.4. Ferroelectricity

Ferroelectrics are defined by the existence of spontaneous polarisation P_s at the absence of external electric field with the polarisation direction able to be switched within a polar crystal by an applied electric field. Another characteristic of ferroelectric materials is the presence of dipole clusters or domains, as a result of the orientation of the dipole moments [13][14]. Ferroelectricity was discovered in 1921 by Joseph Valasek during an investigation of anomalous dielectric properties in Rochelle salt [13][15]. In 1940, Arthur R. Von Hippel reported ferroelectricity in barium titanate ($BaTiO_3$). Nowadays, the group of ferroelectric materials has been extended up to 250 pure materials. Most of them belong to such crystallographic structures as perovskite, tungsten-bronze, pyrochlore and bismuth-layer type structures. The perovskite is widely regarded as the most common ferroelectric structure, to which belong such compositions as $BaTiO_3$, $PbTiO_3$, $Pb_{0.5}Zr_{0.5}TiO_3$ (PZT), and KNN [7][13][14].

Perovskite type ferroelectric crystal consists of two sub-lattices, one composed by cations (A) and the other by oxygen octahedra surrounding the second cation (BO_6)

(Figure 3). Cations are charged +1, +2 or +3 for A- and +3, +4 or +5 for B-site standing ions [10][16].

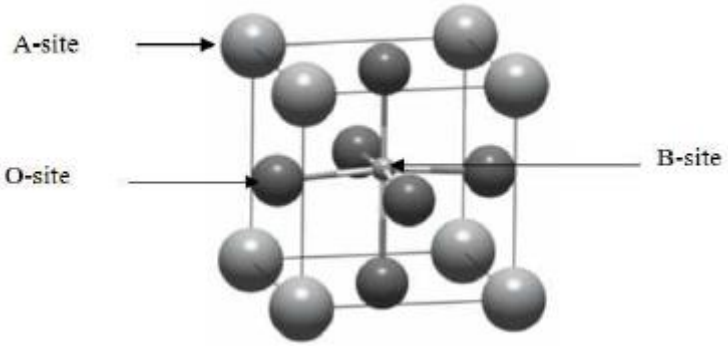

Figure 3- Perovskite ABO_3 unit cell [12]**.**

Perovskite related compounds can be synthesized in a variety of combinations of chemical elements since the perovskite structure accommodates both large A-site and small B-site cations. Moreover, distortions of the ideal cubic structure provide flexibility for incorporating cations of different sizes, whereas the structure is tolerant to vacancy formation [12][17].

In ferroelectric phase, the position of B-site cation is naturally displaced from the unit cell centre, triggering the formation of a dipole. When a group of unit cells present their dipoles aligned in the same direction and these dipoles can be reoriented to a different direction by a strong electric field, such group is called ferroelectric domain [8][11][13]. Transition into a non-polar paraelectric phase occurs due to the thermally induced instabilities of the dipoles related to the temperature increase. The Curie temperature (T_c) is the temperature at which these instabilities develop. This temperature marks the transition between the paraelectric and ferroelectric states, i.e. between centro-symmetric and non-centro-symmetric structures [11]. The piezo-, pyro- and ferroelectric properties disappear in the paraelectric phase until the cooling of the ferroelectric material below the Curie temperature.

When an electric field is applied to a polycrystalline ferroelectric ceramics below T_C, B-site cations are displaced along the electric field direction, forming a net non-zero polarization, which remains after the field removal. Figure 4 presents an illustration of this phenomenon, which is called piezoelectric activation.

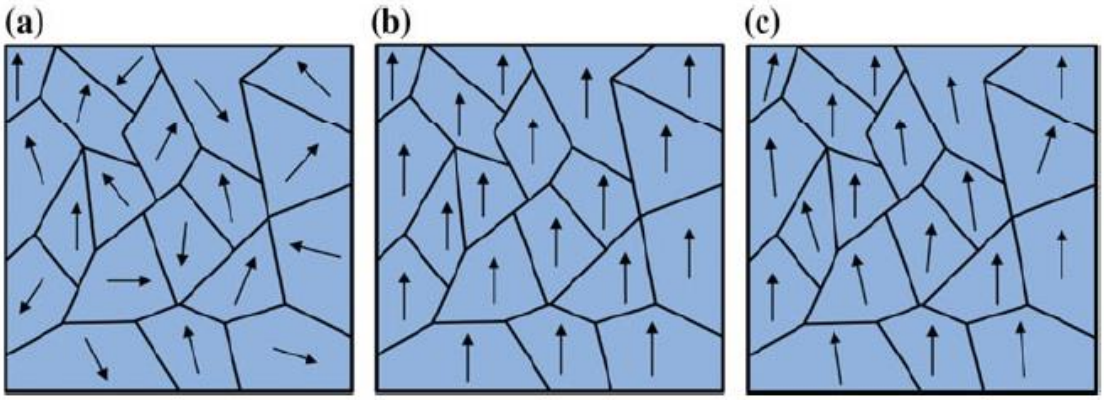

Figure 4- Schematic representation of the poling process of piezoelectric ceramics: (a) initial state, (b) polarization in dc electric field, (c) on removing the electric field, some domains revert to more energetically favourable positions [18]**.**

With the heating of material above the Curie temperature the ceramics turn into centro-symmetric phase and lose their ferroelectric properties. On further zero-field cooling below the Curie temperature it is possible to obtain the ferroelectric state with randomly oriented domains. This phenomenon is denominated as depolling (Figure 5) [19].

The study of the ferroelectric domains in piezoelectric materials is extremely important to understand their properties. There are several techniques to study the structure and distribution of domains including scanning probe, optical, polarization light, transmission electron and scanning electron microscopy [3][20].

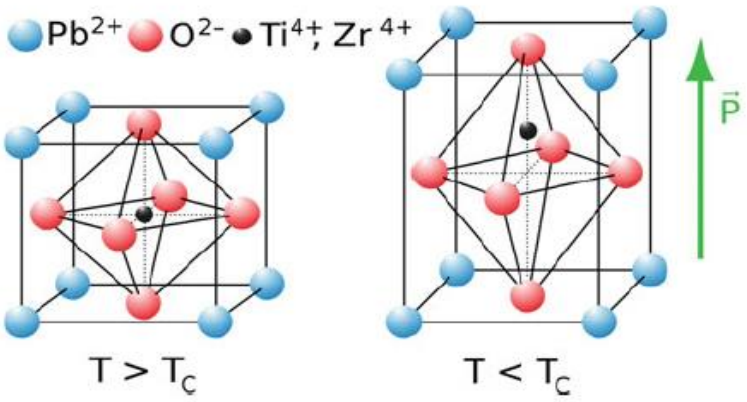

Figure 5- Intrinsic piezoelectric effect in lead zirconate titanate, showing a crystalline unit cell above and below the Curie temperature (T_C), where the charged zirconium or titanium ion moves relatively to the centre position [18]**.**

2.5. Crystal Systems

Crystal systems are categorised into 32 point groups according to their symmetry [8][12]. As shown in Figure 6, these groups are divided in two classes, centro-symmetric (with a centre of symmetry) and non-centro-symmetric (without a centre of symmetry). The latter are sub-divided into 21 point groups of which 20 exhibit piezoelectricity. Within this 20 point groups, 10 of the crystal classes show spontaneous polarization (ferroelectricity).

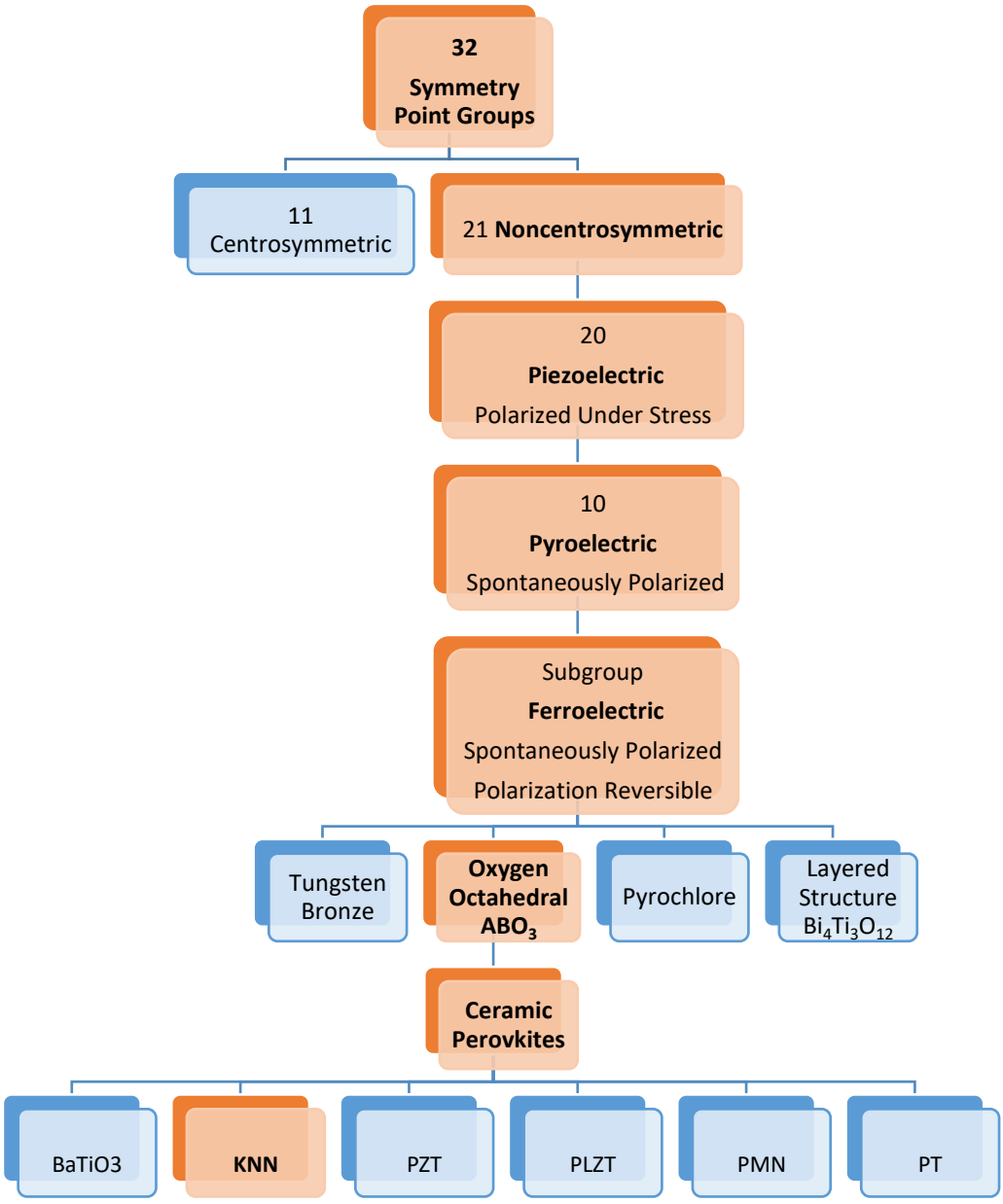

Figure 6- Hierarchisation of crystal classes based on the symmetry point group [8].

$K_{0.5}Na_{0.5}NbO_3$ is a ferroelectric with perovskite structure [8]. KNN is a solid solution between the ferroelectric (potassium niobate, $KNbO_3$ (KN)) and the antiferroelectric (sodium niobate, $NaNbO_3$ (NN)) materials. At room temperature (RT), NN is described as orthorhombic (space group *Pbcm* (No. 57)) and KN is described as tetragonal (*P4mm* (No. 99)) [11][21]. Thus, KNN has a slightly distorted perovskite structure, with symmetry described as orthorhombic, but can be also indexed as monoclinic with the β angle very near to 90° [21].

2.6. Potassium Sodium Niobate (KNN)

A major attempt to research lead free piezoelectrics has started since European Union restricted the use of lead. Despite the efforts made to find a feasible alternative to lead-based materials, there is still a verified deficit of fundamental studies on lead free materials [11].

Three important perovskite families based on $BaTiO_3$ (BT), $Na_{0.5}Bi_{0.5}TiO_3$ (NBT) and KNN, exist amongst lead free piezoelectric ceramics [7][22][23]. Within these families, KNN is considered the most promising due to its high Curie temperature (T_C up to 420°C), good piezoelectric properties (d_{33} = 80 pC/N), electromechanical coupling coefficient (k_p = 48%), and relative dielectric permittivity (ε_r = 230-475). Moreover, the piezoelectric coefficient can be increased by the composition and microstructure optimization (Figure 7) [24][25]. Despite these features, KNN still needs a significant improvement in order to become a suitable substituent for PZT.

The European Union established an exception on the use of lead based piezoelectric materials since they still present better properties compared to the sustainable lead free materials, although the lead based materials are limited for high temperatures applications by their Curie temperature. In Figure 7 it is shown that PZT materials have higher dielectric permittivity (Figure 7a)) and piezoelectric coefficient (Figure 7b)) compared to BT and NBT based materials. At the same time, KNN has some compositions with properties in the range of PZT based materials. Furthermore, KNN based materials present reasonable values of dielectric permittivity and

piezoelectric coefficient for Curie temperatures higher than the ones achieved by PZT. For this reason, KNN is the most appropriate material for high temperature applications [11][26].

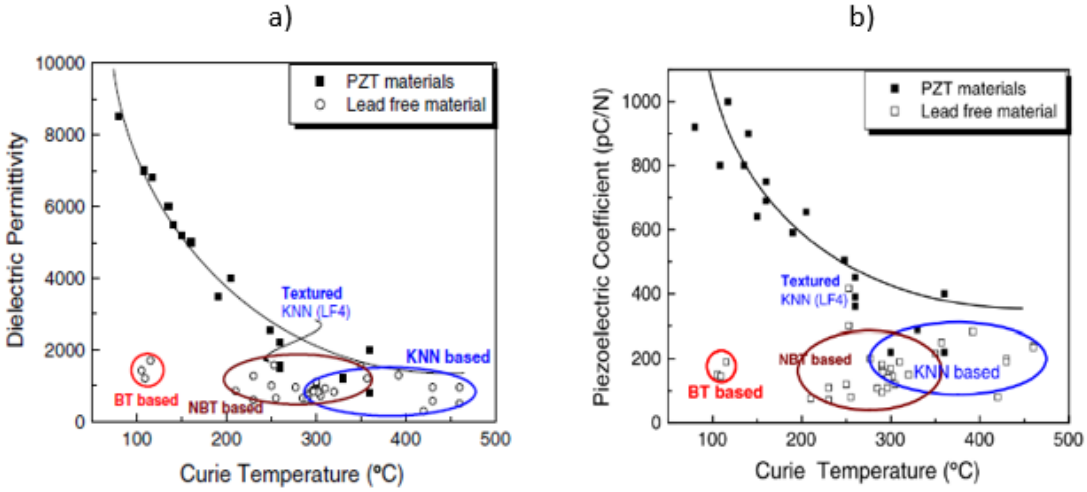

Figure 7- Room temperature values of a) dielectric permittivity and b) piezoelectric coefficient as a function of T_C for various piezoceramics [7]**.**

Similarly, to PZT, potassium sodium niobate (KNN) is a solid solution between the ferroelectric (potassium niobate, $KNbO_3$ (KN)) and the antiferroelectric (sodium niobate, $NaNbO_3$ (NN)) materials. At room temperature (RT), KN and NN are tetragonal and orthorhombic, respectively [11][21]. All the phases crystalize in the perovskite structure, but with different symmetries [22]. Binary phase diagram of the corresponding system $(1-x)(KNbO_3)-x(NaNbO_3)$ is shown in Figure 8. The "morphotropic phase boundary (MPB)" that separates two orthorhombic ferroelectric phases was identified at $x \approx 0.5$ [11][16]. In Figure 8, the first phase that appears during the cooling from the *liquidus* state following the green line for x = 0.5 is cubic and paraelectric one. The *solidus* and *liquidus* lines for this composition are at 1140°C and 1220°C, respectively [22]. A cubic to tetragonal phase transition occurs at 420°C, indicating this temperature as the Curie temperature of paraelectric to ferroelectric phase transition in KNN. The tetragonal to orthorhombic phase transition appears on further cooling around 200°C. Around -150°C the structure becomes rhombohedric. The maximum application temperature for piezoelectrics does not exceed ½ of their Curie temperature, thus it is important to keep a high Curie temperature [25]. In addition, it was reported in the literature, that virtually morphotropic transition,

associated with a broad peak in piezoelectric properties, occurs near 47.5% $KNbO_3$, which is the ideal value to achieve the best piezoelectric properties of KNN [11].

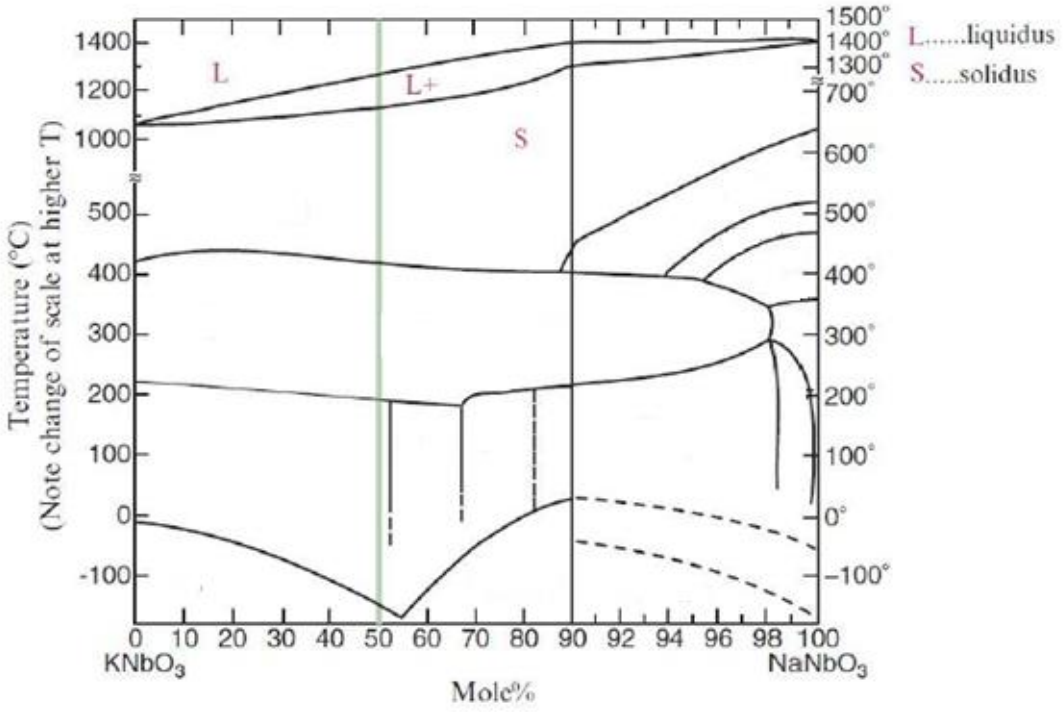

Figure 8- Phase diagram of $KNbO_3$-$NaNbO_3$ system [11]**.**

2.6.1. KNN Ceramics

The solid state method, using oxides and carbonates precursors like K_2CO_3, Na_2CO_3 and Nb_2O_5 and calcination temperatures between 850°C and 950°C, is the most used route for synthesis of KNN ceramics [27][28][29]. Then the global chemical reaction is as considered in Equation 8:

$$\frac{1}{4}Na_2CO_3 + \frac{1}{4}K_2CO_3 + \frac{1}{2}Nb_2O_5 \rightarrow (Na_{0.5}K_{0.5})NbO_3 + \frac{1}{2}CO_2 \qquad \text{Equation 8}$$

However, when pure KNN is sintered by the conventional mixed oxides processing it shows several limitations, which are not desirable for industrial applications. The hygroscopic and volatile nature of alkali elements, compositional inhomogeneity, phase stability at high temperatures (related to volatility of the alkali metal oxides, because above 1100°C, alkali-deficient secondary phases of tungsten

bronze structure can appear and are accompanied by abnormal grain growth) and poor densification are some of these limitations [23][30].

It was noticed that pure KNN densification can be improved by manipulation of heating rate, decreasing it to 2°C/min [23]. Dense ceramics can be produced by alternative processes such as hot pressing (HP) [16][27][28], hot isostatic pressing (HIP) [16][28] and spark plasma sintering [16][31] methods. The piezoelectric properties of HP and HIP processed KNN ceramics are enhanced and the coupling coefficient becomes higher than the value reported for conventional techniques, due to improved densification [28]. However, these two techniques are expensive and not attractive for industrial applications. In spark plasma sintered KNN, high density and d_{33} values up to 148 pC/N are achieved. However, it is necessary to perform a high temperature post-annealing of the sintered KNN ceramics to reduce their conductivity induced by the oxygen vacancies [5][32].

The main objective of doping is to improve the densification and the properties of the material for specific application. In the perovskite structure, such elements as Li, Mg, Ca, Sr, Ba, La, Eu [16][33] and W, Ce, Ti, Mn, Fe, Ta [16][34] can occupy A- and B-sites, respectively. The best properties reported until now at room temperature were obtained in KNN ceramics doped with Li, Ta and Sb [6]. The density and electromechanical properties of doped ceramics are improved, to a certain extent, when compared to undoped KNN, without decreasing Curie temperature. However, their properties did not reach the ones from PZT. Thus, it is not possible to replace it for the industrial applications.

2.6.2. KNN Single Crystals

Until now, few studies have been published on the growth and properties of KNN single crystals in comparison to polycrystalline KNN [35][36][37]. The electromechanical properties of lead based ferroelectric single crystals like $Pb(Zn_{1/3}Nb_{2/3})O_3$-$PbTiO_3$ and $Pb(Mg_{1/3}Nb_{2/3})O_3$-$PbTiO_3$ are five times higher than bulk PZT [38]. When compared to other ceramics, KNN single crystals have shown better electromechanical properties, which is the reason for the beginning of the

investigations on KNN single crystals [39][40]. Several methods can be used to produce this material. Kizaki *et al*. (2006) reported the use of a molten salt method to produce KNN single crystals. In this method the solvent is a molten salt or oxide and, in this case, NaF and KF were used as fluxes [41]. Another method to obtain KNN single crystals is solid state crystal growth, which basic principle is the abnormal grain growth. In this method, a single crystal is buried in a powder matrix during a long period at high temperatures. In the case of $(K_{0.5}Na_{0.5})NbO_3$, $KTaO_3$ is used as the seed crystal. One of the problems is the appearance of porosity, although HP can be used to reduce the porosity in the grown crystal [42]. The following Table 1 presents the main differences between the undoped KNN ceramics, doped KNN ceramics and KNN single crystals.

Table 1- Dielectric permittivity and piezoelectric coefficient (d_{33}) for undoped, doped and doped/textured KNN ceramics as well as KNN single crystals.

Composition	Dielectric permittivity (ε_r)	Piezoelectric coefficient (d_{33})	Ref.
KNN	290	80 pC/N	[7]
KNN LF4		300 pC/N	[6]
KNN LF47	1570	416 pC/N	[6]
KNN single crystals	240	160 pC/N	[40]

2.6.3. KNN Thin Films

The term “thin films” is usually employed to designate a set of materials processed into layers, with a total thickness that can reach the order of micrometres, deposited on a substrate. Their mechanical properties are generally obtained from the properties of a bulk material with the same chemical composition. In general, the films are formed as a sequence of superimposed materials. Each layer is either formed of a single phase or by more than one phase material.

Most literature is focused on KNN-based bulk materials. Recently, KNN based films have received more attention as one of the promising alternatives in various

applications, such as sensors, actuators, energy harvesting systems and microelectromechanical systems (MEMS). This attention is due to the high piezoelectric properties in their bulk counterparts. However, two main issues still inhibit the fabrication of high-quality KNN-based films: composition deviations from stoichiometry and the loss of alkali oxides during its preparation. For a pure KNN thin film, some factors strongly affect their ferroelectric and piezoelectric properties, such as the use of stabilizing agents, new preparation techniques, excess alkali metals, different substrates, processing conditions, buffer layers, dopants or ion substitutions, orientation, annealing atmosphere, etc. It is also important to focus on the construction of phase boundaries as well as on the relationships between strain and electrical properties if subsequent breakthroughs are desired.

Most KNN-based thin films with proper ferroelectric and piezoelectric characteristics are synthesized by RF-magnetron sputtering, pulsed laser deposition (PLD), metal–organic chemical vapour deposition (MOCVD) and sol–gel methods. However, the high volatility both of sodium and potassium complicates the fabrication of KNN thin films by physical vapour deposition processes. In this study the sol–gel method is used for deposition with advantages such, as low temperature fabrication, precise control of the chemical composition of the film, and reduced equipment cost, making it promising for producing homogeneous thin films.

The use of substrates also affects the ferroelectric properties of KNN thin films, due to the involvement of the orientation. Epitaxial thin films grown on single crystalline substrates are important to exhibit high performance.

Compared with bulk ceramics and polycrystalline thin films, where the presence of the grain boundary and random orientation of the grains complicates the study of the microscopic physical properties, the epitaxial thin films have a similar structure to the single crystals with a preferred orientation, which can be considered as ideal for studying the mechanism of piezoelectricity [4][43].

In the preparation of KNN-based thin films, the proportion among potassium (K), sodium (Na) and niobium (Nb) is likely to diverge from stoichiometry. This is due to the volatilization of K and Na during the calcination process at high temperatures. The vacancies left by the evaporation of K and Na ions result in poor ferroelectricity and

high leakage current on KNN films. A relatively high leakage current in the KNN thin films is induced by oxidation, leading to electron–hole ($h^{\bullet}$) (p-type) conduction. This is expressed as the defect reaction formula (($V_o^{\bullet\bullet} + 1/2O_2 \rightarrow O_o^x + 2h^{\bullet}$), where $V_o^{\bullet\bullet}$ indicates the vacancy at the oxide-ion site O_o^x and represents O^{2-} at the oxide-ion site.

One of the key issue in the KNN thin film fabrication is the heating rate in the heat-treated process. With a decrease in the heating rate, the total heating time increases. Hence, the K and Na ions become volatile, yielding A-site ion vacancies. The volatility of K and Na ions triggers the formation of oxygen vacancies which maintain the neutral charge in the perovskite KNN films. Therefore, cation and anion defects are generated in the KNN thin films during the crystallization heat treatment. As a result, reasonably saturated *P-E* hysteresis loops can be created. To compensate the volatilization loss of K and Na, two overdose methods were applied. The first, consists in the addition of both K and Na ions in equal amount, while in the second, only one of these ions is added in overdose [44][45][46].

In this study, both methods are used, since their volatilization tends to induce defects in the resulting films, which can significantly decrease both ferroelectric and piezoelectric performance [47]. First, a solution with 20% excess of K and 20% excess of Na was prepared, as an attempt to obtain electrical measurements similar to the ones reported by Ahn *et al*.[48]. In the previous study, it was prepared a thick film from acetate-alkoxide based solution with 250 nm by drying at 150^{o}C, two pyrolysis steps and final heating at 700^{o}C for 30 minutes. When the coating solution contained 20% alkali-excess, the preferentially (100) oriented films exhibited ferroelectric loops with a remnant polarization of 10 μC/cm^2 and coercive field of 35 kV/cm (Figure 9). Through the electron probe microanalysis of the films, prepared from solutions with different amounts of alkali excess, it was verified that the volatilization of Na was larger than that of K, which is in agreement with the results obtained by Wang *et al.* [49]. Based on work by A. Kupec *et al.*[50], a solution with only 5% excess of K was also prepared for this dissertation.

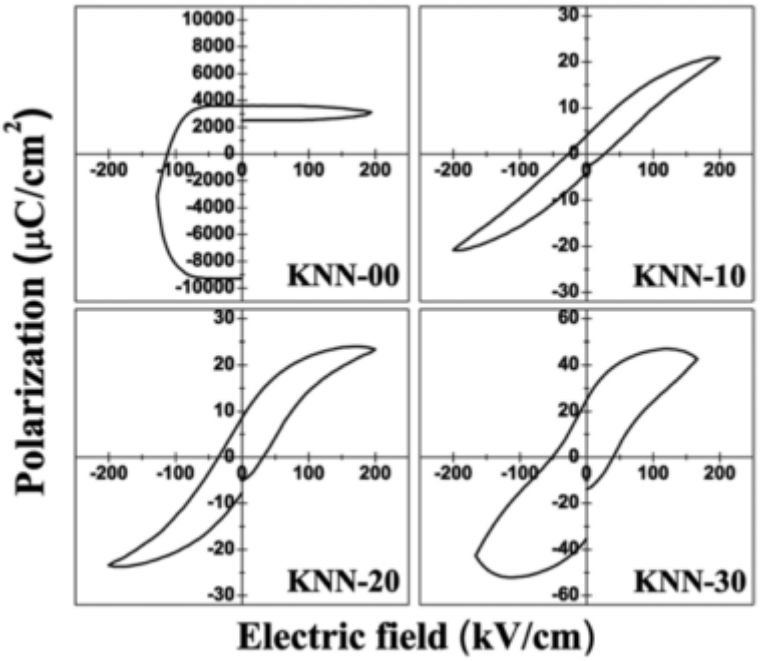

Figure 9- *P–E* hysteresis loops of KNN thin films grown using 0, 10, 20, 30% K and Na excess precursor solution at room temperature [48]**.**

Table 2 shows the electrical properties reported in the literature for the KNN thin films produced by different techniques.

Table 2- Electrical properties ok KNN thin film reported in the literature.

KNN	Deposition technique	Excess (%)	Molar concentration	Substrate	Thickness (nm)	ε_r at room temperature	tanδ	P_r ($\mu C/cm^2$)	Ec (kV/cm)	d_{33}	Ref.
$K_{0.48}Na_{0.52}NbO_3$	Sol-gel	6% K and 17% Na	0.3	$Si/SiO_2/TiO_2/Pt$	250	699 (10 kHz)	0.039	-	-	-	[44]
$K_{0.5}Na_{0.5}NbO_3$	Sol-gel	5% K	0.4	$Si/SiO_2/TiO_2/Pt$	250	614 (1 kHz)	0.015	8 (1 kHz)	80	-	[50]
$K_{0.5}Na_{0.5}NbO_3$	Sol-gel	2% K and 8% Na	0.35	$Si/SiO_2/TiO_2/Pt$	-	725 (1 kHz)	~0.09	9.1 (1 kHz)	80	-	[51]
$K_{0.5}Na_{0.5}NbO_3$	Sol-gel	20% K and 20% Na	0.1	$Si/SiO_2/TiO_2/Pt$	250	-	-	10 (1 kHz)	35	40 pm V^{-1}	[48]
$K_{0.5}Na_{0.5}NbO_3$	Sol-gel	40% K and 40% Na	0.3	$Si/SiO_2/TiO_2/Pt$	500	~525 (100 kHz)	~0.3	11.2 (1 kHz)	~20	40.23 pC/N	[47]
$K_{0.5}Na_{0.5}NbO_3$	Sol-gel	0	0.35	$Si/SiO_2/TiO_2/Pt$	-	~240 (1 kHz)	~0.16	2 (1 kHz)	80	-	[51]
$K_{0.5}Na_{0.5}NbO_3$	Sol-gel	0	0.3	$Si/SiO_2/TiO_2/Pt$	120	258 (1 kHz)	0.05	3.4 (1 kHz)	160		[52]
$K_{0.5}Na_{0.5}NbO_3$	RF-Sputtering	0	-	$LaAlO_3$	1.5 µm	470 (1 MHz)	0.01	11.5 (300 Hz)	95	15.1 pC/N	[53]
$K_{0.5}Na_{0.5}NbO_3$	RF-Sputtering	-	-	$Pt_{80}Ir_{20}$	1.5 µm	530 (100 kHz)	0.016	9.7 (300 kHz)	95	-	[54]
$K_{0.5}Na_{0.5}NbO_3$	aerosol-deposition	-	-	$Si/SiO_2/TiO_2/Pt$	7.1 µm	545 (1 kHz)	~0.03	8.1	100	-	[55]

2.7. Strain/Stress Influence

All dielectric materials are electrostrictive, but in ferroelectrics the quadratic coupling between polarization and strain can be especially strong. This strong polarization-strain coupling is responsible for the changes in the paraelectric-to-ferroelectric transition temperature (T_C, also called the Curie point), piezoelectric coefficients, and dielectric and electro-optic properties when the mechanical boundary conditions of a ferroelectric are altered [56].

The hydrostatic compression (three-dimensional compression) causes the decrease of the dielectric permittivity and the Curie temperature of ferroelectrics [57][58]. The increase in the dielectric permittivity and T_C is directly related to the application of two-dimensional compression normal to the electrodes of the parallel plate capacitor filled with a ferroelectric. The fact that ionic positions and vibrations in a ferroelectric are modified by the stress, and these changes are coupled to the polarization mechanism in the ferroelectric, causes the effect of the stress on the dielectric permittivity and the T_C [59].

Pb-based piezoelectric ceramics exhibit much higher electric field induced strain that their lead-free counterparts, therefore control the market of piezoelectric actuators [6][60]. The high strain, which can be obtained in PZT, is normally attributed to two factors. The first factor is due to the electronic structure of Pb^{2+} ion which makes it highly polarizable, resulting in a distortion of the crystal lattice. The second is related with the existence of a morphotropic phase boundary (MPB) between phases belonging to different domain orientation, also resulting in a higher piezoelectric effect. In Pb-based antiferroelectric ceramics such as (Pb, La)(Sn, Zr, Ti)O_3, high strain is obtainable as a result of a field induced transition from an antiferroelectric to a ferroelectric phase. In fact, the development of actuators based on ceramic materials, which sustain such phase transition under electric field, has been of great interest in the past decade [6][7][61]. However, this approach of inducing high strain has not yet been achieved for lead-free piezoelectrics.

The lead-free counterparts are characterized by accurate displacements against large forces in microseconds. However, they are hampered by their small achievable

strains, about 0.1%-0.2% and environmental issues call for the use of non-hazardous materials, e.g. lead-free ceramics with a competitive performance [62]. Different approaches, including special actuator designs and enhancement of the piezoelectric strain coefficient d_{33} by special material composition have been developed for achievement of large displacement actuators [60][63]. For single-crystal systems with compositions near the morphotropic phase boundary, large attainable strain (approximately 1%) have been reported, whereas their ceramic counterparts display a strain of only proximally 0.2% [62][64]. Recently, the achievement of a large recoverable strain in a piezoelectric ceramics has been demonstrated [65] and attributed to an unusual reversible switching of non-180^o domains when the applied electric field is removed [60].

Regarding the films, they are always under stress/strain due to the substrate and the heat treatments during their deposition. Strains can be imparted into thin films through differences in lattice parameters and thermal expansion behaviour between the film and the substrate, or they can arise from defects formed during film deposition [66][67]. Fully coherent, epitaxial films have the advantage that high densities of threading dislocations (e.g., the proximally 10^{11} cm^{-2} dislocations observed in partially relaxed ferroelectric films) are avoided [68][69]. The strain field around dislocations locally alters the properties of the film, making its ferroelectric properties inhomogeneous and often degraded [70][71].

The lattice mismatch is relevant for epitaxial films. Here, film growth takes the orientation of the single crystal or textured substrate. Thus, lattice mismatch is defined through Equation 9:

$$Lattice\ mismatch = \frac{a_{substrate} - a_{film}}{a_{substrate}} \qquad \text{Equation 9}$$

where $a_{substrate}$ is the substrate lattice parameter and a_{film} is the free-standing film lattice parameter. The compatibility of the substrate bottom with the film may result in strains in the latter, namely compressive ($a_{film} > a_{substrate}$) or tensile ($a_{film} < a_{substrate}$) [72].

Strain can be defined as the change of length, being its dimensionless value measured in films. The *stress* value, that is force per unit of area (measured in kN/m^2 or Pa), can be calculated from the *strain*:

$$Strain = E_Y \times Stress \qquad \text{Equation 10}$$

where E_Y is the elastic Young's modulus of the material. So *stress* can be calculated either in compressive or tensile state.

Stresses in polycrystalline films are more difficult to be predicted and calculated than the case of epitaxial films, because there is a presence of grain boundaries in the former. One cause of stresses in thin films is the lattice mismatch between the film and the substrate. It was observed that lattice mismatch plays a critical role in the dielectric response of ferroelectric thin films. It has been demonstrated that this condition might create interfacial defects, which induce strains in ferroelectric thin films. Thus, a combination of strain and interface effects are responsible for the differences in the dielectric properties of thin films and single crystals. Another cause of stress in thin films might be related to the annealing process after or during their deposition. Since high temperatures are usually necessary for the crystallization of the required film phase (perovskite phase), stress between the substrates and films develops upon cooling to room temperature, due to the difference in the thermal expansion coefficients (TEC, α) of the film (α_{film}) and substrate ($\alpha_{substrate}$). Then thermal stress (σ_{th}) can be represented as:

$$\sigma_{th} = \int_{RT}^{T_{ann}} \frac{E_f}{1-\gamma_f} \times \left(\alpha_{film}(T) - \alpha_{substrate}(T)\right) dT \qquad \text{Equation 11}$$

where E_f is the Young's modulus of the film and γ_f is the Poisson ratio of the film. Thermal stress can induce structural changes and stress driven preferred orientation of the film, resulting in the change of their dielectric response and cracking of the films. This leads to a short circuiting between their top and bottom electrodes [72].

To understand the effect of the stress on the dielectric properties, Landau-Ginzburg-Devonshire formalism provides a framework. In this framework, it was predicted that for strained $BaTiO_3$ and $PbTiO_3$ thin films the temperature of the phase transition should be higher than in corresponding bulk material. This phase transition would be changed from a first order transition as in bulk materials to a second order one in films [73]. This theoretical prediction was later corroborated experimentally on epitaxial (001) oriented $BaTiO_3$ and $PbTiO_3$ film on cubic substrates, by Pertsev *et al.* [74]. The obtained results can be explained as influence of the compressive stress and tensile stress. The compressive stress results in an "out-of-plane" oriented polarization, while a tensile stress creates an oriented "in-plane" polarization [72][74].

The influence of the stresses induced in the KNN thin films on the film properties, has not been yet reported in the literature. The purpose of this study is to prepare KNN thin films using the sol-gel technique on different substrates, evaluate the induced stresses and their influence on the microstructure, dielectric properties and ferroelectric properties of the KNN thin films.

3. Experimental Procedure: Preparation and Characterization of Thin Films

3.1. Sol-Gel Fabrication of Thin Films

Sol-gel provides an alternative methodology for conventional powder preparation. Moreover, this technique has been used in the preparation of thin films, due to its easiness of using and control of the material composition. Film fabrication normally involves the deposition of the precursor solutions onto a clean substrate. The resulting as-deposited film is generally amorphous. The most common method for the transformation of the amorphous films into crystalline ones begins with a pyrolysis step of the as-deposited film, for short periods of time, to promote the removal of the organic species. The transformation from the amorphous pyrolyzed film to the crystalline one occurs by the increase of temperature during film annealing. These transformations occur due nucleation and growth processes, in which the increasing temperature during film annealing provides the energy to overcome the barrier heights of homogeneous and heterogeneous nucleation.

To fulfil the objectives proposed in this dissertation, this chapter is dedicated to the description of the strategy used to approach the stated problem. Thus, the following section describes the experimental procedure conducted to fabricate KNN thin films on Si/SiO_2, polycrystalline Al_2O_3, $Si/SiO_2/TiO_2/Pt$, Al_2O_3/Pt and $SrTiO_3/Pt$ substrates, through the precursor sol-gel method and to characterize the obtained films. Figure 10 shows the flowchart of the steps since the reagents, the time of distillation, the atmosphere used, the molar concentration of the KNN solution, the pyrolyzed step, the conditions used to deposit the KNN solution in the substrates and the annealing conditions.

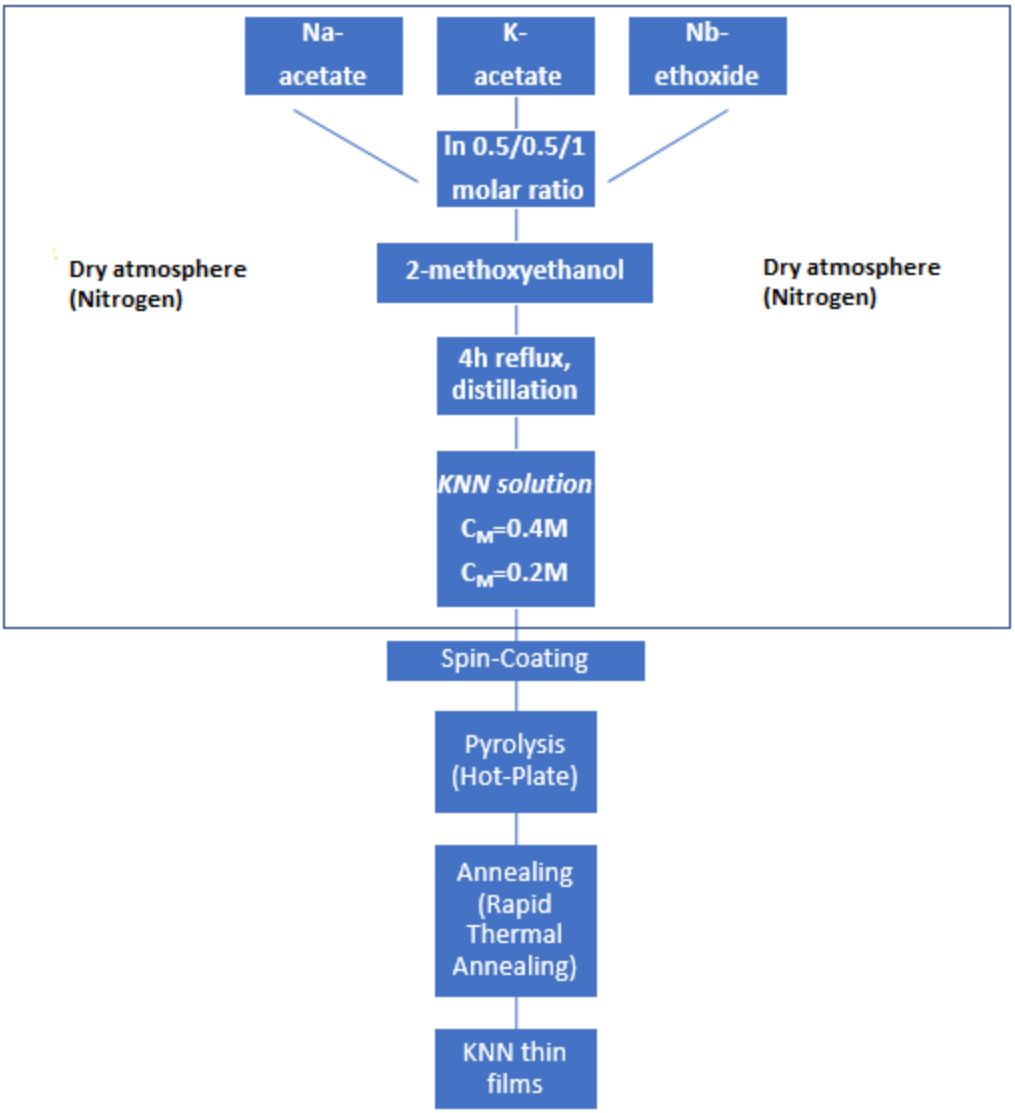

Figure 10- Scheme of preparation of the KNN solution.

3.1.1. Preparation of the Solution

For the preparation of the sols with a concentration of about 0.4 M and 0.2 M the following reagents were used: potassium acetate $KO_2C_2H_3$ (≥99%, ChemPur, GmbH), sodium acetate $NaO_2C_2H_3$ (99%, Alfa Aeasar) niobium pentaethoxide $Nb(OCH_2CH_3)_5$ (99%, Stark, Munich, Germany) and 2-methoxyethanol (99%, Sigma Aldrich, Steinheim, Germany) (Table 3). $Si/SiO_2/TiO_2/Pt$ substrates were bought from Inostek INC, Korea. Al_2O_3 and $SrTiO_3$ substrates were bought from Crystal GmbH, Germany with following platinization in Inostek INC, Korea.

Table 3- List of the precursors used for the film preparation.

Chemical name	Chemical formula	Purity	Source
Potassium acetate	$KO_2C_2H_3$	≥99%	ChemPur, GmbH
Sodium acetate	$NaO_2C_2H_3$	99%	Alfa Aeasar
Niobium pentaethoxide	$Nb(OCH_2CH_3)_5$	99.9%	ABCR, Germany
2-methoxyethanol	2-methoxyethanol	≥99.99%	Sigma Aldrich, Steinheim, Germany

Initially, approximately 12 g of 2-methoxyethanol were placed in a closed flask and left for 30 minutes in argon (Ar) under constant stirring. Using a glove box with an atmosphere of nitrogen (N_2), the potassium acetate ($KO_2C_2H_3$), sodium acetate ($NaO_2C_2H_3$) and niobium pentaethoxide ($Nb(OCH_2CH_3)_5$) were weighted in a requested ratio and dissolved in the 2-methoxyethanol. 20% excess of potassium (K) and sodium (Na) as well as 5% excess of potassium (K) were used in this study. After the mixing, the solution remained during approximately 30 minutes in nitrogen and was stirred at the same time. The solution was stirred at a reflux temperature of about 106^{o}C for 4 hours and distilled at 124^{o}C. After cooling, the KNN solution was transferred to the 25 ml flask with further addition of the 2-methoxyethanol to keep the concentration at 0.4 M or 0.2 M. Thus, four stable solutions with 5% of K and 20% excess of K and Na as well as 0.4 M or 0.2 M concentrations were prepared in this study. Table 4 resumes the four solutions, the excess precursor used and its percentage, the amounts of all the precursors and the molar concentration of the final solution.

Table 4- Compositions of the four KNN solutions prepared in this work.

Solution	Alkali Excess	Excess percentage	KNN precursors			2-methoxyethanol (g)	Molar concentration
			K- acetate (g)	Na-acetate (g)	Nb-ethoxide (ml)		
1	Potassium and sodium acetate ($KO_2C_2H_3$ + $NaO_2C_2H_3$)	20% + 20%	0.5948	0.4972	2.51	21.0233	0.4 M
2		20% + 20%	0.5948	0.4972	2.51	42.0466	0.2 M
3	Potassium acetate ($KO_2C_2H_3$)	5%	0.5205	0.4143	2.51	22.6813	0.4 M
4		5%	0.5205	0.4143	2.51	45.3626	0.2 M

3.1.2. KNN Thin Films Deposition

Using the previously prepared precursor solutions, layers were deposited on such substrates as Si/SiO_2, polycrystalline Al_2O_3, $Si/SiO_2/TiO_2/Pt$, Al_2O_3/Pt and $SrTiO_3/Pt$ by spin-coating (Chemat Technology spin-coater KW-4A). Before being used, the substrates were cleaned in boiling ethanol and dried on the hot-plate.

The four KNN solutions passed through a 0.2 µm filter in a syringe and were spin-coated for 30 s at 3000 rounds per minute on the substrates. The as-deposited layers were pyrolyzed at 350ºC for 2 min on a hot-plate in air. This step was repeated after each spinning to ensure complete removal of volatile species between each layer. After the deposition of the required number of layers, films were annealed in air at defined temperatures for 5 min at 750ºC. (Figure 11). In this study, to anneal the films was used a thermal rapid annealing equipment (Jipelec, Jetfirst).

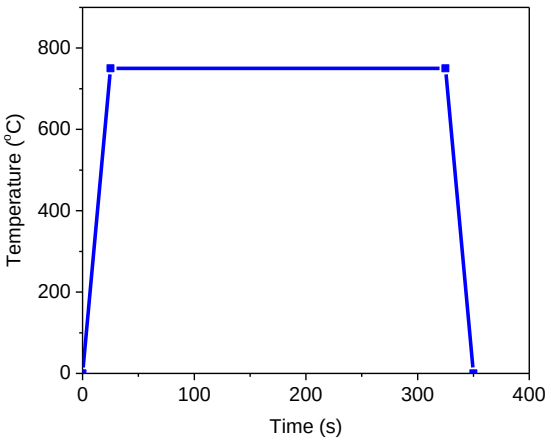

Figure 11- Conditions of the thermal cycle to which the films were subjected.

The solution with 0.4 molar concentration was deposited in 5 layers and the solution with 0.2 molar concentration was deposited in 10 layers at each substrate previously chosen.

The Si/SiO_2 and polycrystalline Al_2O_3 substrates were used only for KNN solution with 20% excess of potassium and sodium and 0.4 molar concentration in order to evaluate the induced strain, structure and microstructure of the films in comparison to the platinized substrates.

Table 5 presents the 12 films, being a combination between the 5 substrates and the 4 KNN solutions as well as their deposition conditions, namely the duration and temperature used for spin-coating, pyrolysis and crystallization.

Table 5- List of KNN films indicating the used solutions, substrates and the deposition conditions.

Excess percentage	Molar concentration	Substrate	Number of layers	Pyrolysis		Spin-coating		Crystallization (RTA-air)		
				Time (s)	Temp.(°C)	Time (s)	Rotation (rpm)	Time (s)	Temp.(°C)	Heating/Cooling rate (°C/s)
20%+20%	0.4	Si/SiO_2	5	120	350	30	3000	300	750	30
20%+20%	0.4	polycrystalline Al_2O_3	5							
20%+20%	0.4	$SrTiO_3/Pt$	5							
20%+20%	0.4	Al_2O_3/Pt	5							
20%+20%	0.4	$Si/SiO_2/TiO_2/Pt$	5							
20%+20%	0.2	$SrTiO_3/Pt$	10							
20%+20%	0.2	Al_2O_3/Pt	10							
20%+20%	0.2	$Si/SiO_2/TiO_2/Pt$	10							
5%	0.2	$SrTiO_3/Pt$	10							
5%	0.2	Al_2O_3/Pt	10							
5%	0.2	$Si/SiO_2/TiO_2/Pt$	10							
5%	0.4	$Si/SiO_2/TiO_2/Pt$	5							

3.2. Crystallographic and Microstructure Characterization

3.2.1. X-Ray Diffraction Analysis

The structural characterization of the material generally starts with the X-ray diffraction (XRD) analysis. This is a versatile and non-destructive technique, which is able to reveal detailed information about the crystallographic structure of the materials. Nowadays, X-ray diffraction enables a variety of techniques that allow the characterization of different material classes [75].

3.2.1.1. Standard X-Ray Diffraction Measurements

In 1913, Henry and Lawrence Bragg developed a simple way to understand the diffraction phenomena from a crystal [75]. They state that a crystal lattice is a regular three dimensional distribution of atoms arranged in parallel planes separated from each other by a certain distance (*d*). This distance varies according to the nature of the material. When a monochromatic X-ray beam with a certain *theta* angle (θ) and wavelength (*λ*) is projected onto a crystalline material, diffraction develop if the distance travelled by the rays reflected from successive planes differs by a complete number (*n*) of wavelengths. This process is described by Bragg's law (Equation 12)[76]:

$$\kappa\,\lambda = 2d_{hkl}\sin\Theta \qquad \text{Equation 12}$$

where *d* corresponds to the space between the planes and *(hkl)* the Miller indices. To satisfy the Bragg's law it is necessary to vary the *theta* angle (θ) in order to get conditions by different *d*-spacing in polycrystalline materials. The Bragg's law conditions are satisfied by different *d*-spacings in polycrystalline materials when theta angle is varied and *κ* becomes the complete number of wavelengths.

I this work, the phase evolution analysis of KNN thin films was performed by X-ray diffraction with a Rigaku (D/Max-C series) X-ray diffractometer, using Cu-Kα radiation (λ=0.15064 nm), equipped with MDI data scan 3.2 controller software. The

XRD was typically operated at 40 kV and 30 mA and θ-2θ scan technique was adopted to collect the diffraction intensity data with Cu-Kα radiation at rate 1°/min, with step 0.02 between 10-70°.

3.2.1.2. Grazing Incidence Measurements

When the X-rays intercept the film, they penetrate to a certain depth, where they are diffracted. When the film layer is too thin, the X-rays can be transmitted by the sample or part of them can be diffracted by the substrate. This provokes no diffracting signal or an overlap between the substrate and the sample diffraction peaks. In these specific cases the in-plane diffraction is used. In this diffraction technique both the incident and diffracted beams are practically parallel to the film surface (Figure 12) [77].

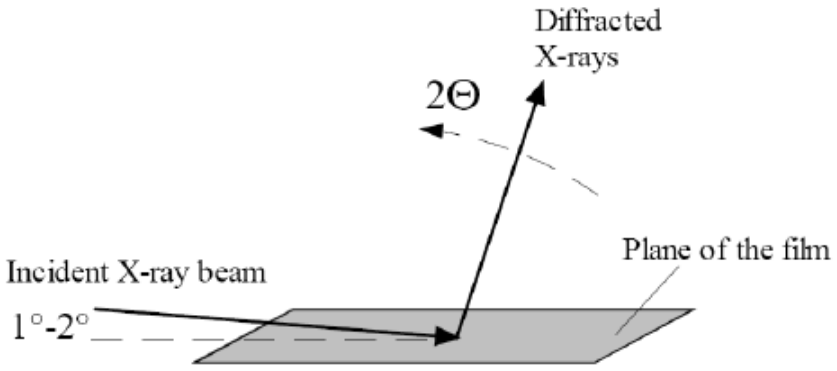

Figure 12- Scheme of grazing incidence XRD experiment [72]**.**

With standard diffraction geometries, lattice planes that are parallel to the sample surface are then measured. In-plane diffraction has two important characteristics. The first feature is, since the beam is incident at the grazing angle, small angle, the penetration depth of the beam is limited to within 100 nm of the surface. The second characteristic is that the in-plane diffraction technique can measure diffracted beams, which are dispersed nearly parallel to the sample surface. So, it is possible to measured lattice planes that are perpendicular to the sample surface, being these planes inaccessible by other techniques.

In this work, the in-plane incidence measurements of the different thin films were performed using a Philips X'Pert MPD X-Ray diffractometer, equipped with a mobile arm and X'Pert Data Collector controller software, with *CuKα* radiation, to determine in-plane lattice parameters. The X-Ray diffraction patterns were obtained between 10º and 60º in θ-2θ with a step mode of 0.01º/10s and using a grazing incidence angle of 2º.

3.2.1.3. Texture Films (Pole Figures)

The texture of the film can be evaluated by pole figure measurement. This procedure allows measuring the intensity of a XRD peak as the sample rotates about two orthogonal axes. Therefore, it is possible to collect the total of the lattice plane reflection signals from a large number of crystallites in a polycrystalline material. To determine the orientation of a given lattice plane (*hkl*), the detector is first set to a proper Bragg angle (*2*θ) of the diffraction peak of interest. After, the sample is rotated in a goniometer until the lattice plane (*hkl*) is in a reflection condition, meaning that the normal to the lattice plane is the bisectrix between incident and diffracted beam [78]. This measurement was performed in a Philips X'Pert MRD equipment.

The texture fraction along (100) planes was calculated from the XRD patterns using the Lotgering approach. The Lotgering factor (*f*) is the fraction of the area textured with the crystallographic plane of interest using:

$$f = \frac{P_{(100)} - P_0}{1 - P_0} \qquad \text{Equation 13}$$

where, $P_{100} = \sum I_{100} / \sum I_{hkl}$ and $P_0 = \sum I^0_{100} / \sum I^0_{hkl}$ with I_{hkl} and I^0_{hkl} being the intensities of *(hkl*) peaks for the textured and randomly oriented KNN thin films, respectively.

3.2.1.4. Residual Strain Measurements

The stress remaining in a material in absence of any external forces is called residual stress. Hole drilling, curvature method, neutron diffraction, electron diffraction, compliance methods, magnetic and electrical techniques, ultrasonic methods, piezospectroscopic techniques, thermoplastic methods, photoelastic methods and X-ray diffraction are some of the methods that determine the stress [79].

Some of those methods are destructive, some are not. X-ray residual stress measurement is a technique considered as non-destructive and together with other diffraction techniques for residual stress measurement uses the distance between crystallographic planes as a strain gage. That is, X-ray diffraction is used as a method for measuring elastic strain in polycrystalline materials [80]. To obtain diffraction from differently oriented sets of planes, needed to determine the different components of the strain, the sample under analyses needs to be rotated with respect to the incident X-ray beam [72].

There is a clear relationship in the distance between atomic planes (the inter-planar spacing) within the material and the diffraction patterns that are observed when X-rays are diffracted through crystal lattices. It is possible to obtain different diffraction patterns by changing the inter-planar spacing or the wavelength of the X-ray beam. A characteristic diffraction pattern for that material will be produced from the inter-planar spacing of a material that is free from strain. When a material is under strain, elongations and contractions are generated inside the crystal lattice, which cause the inter-planar spacing of the (*hkl*) lattice plane. Then, the induced change in space between the planes (*d*) will cause a shift in the diffraction pattern. Due to the shift in the diffraction pattern, the change in the inter-planar spacing can be evaluated and, consequently, the strain inside the material can be deducted. Thus, it is necessary to establish mathematical relationships between the inter-planar spacing and the strain. The orthogonal coordinate systems used in the following explanation are defined in Figure 13 [76].

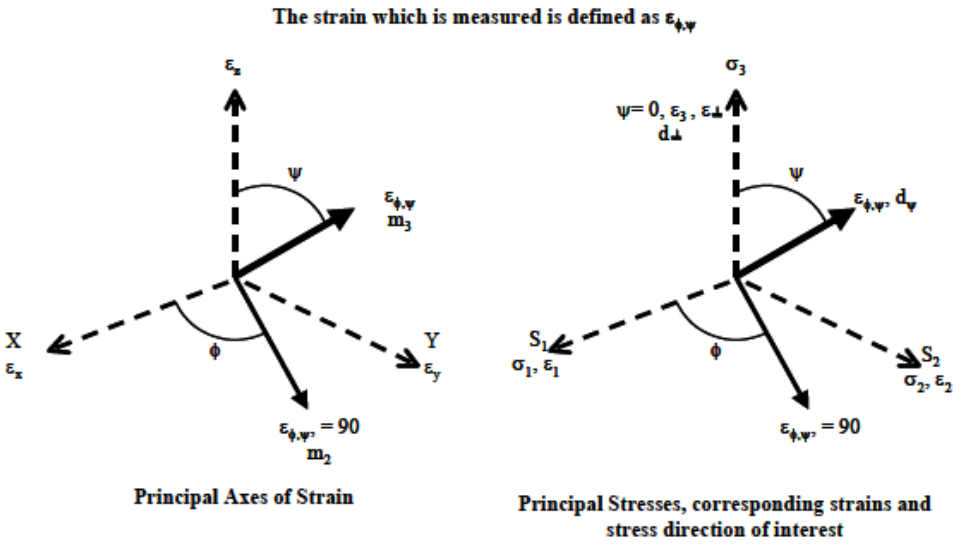

Figure 13- Coordinate system used for calculating surface strain and stresses. Note that ε_z and σ_3 are normal to the specimen surface. σ_1, σ_2 and σ_3 are principal stresses acting in the principal directions [76]**.**

Assuming that the measurement is made near the surface, then the principal stresses acting in the principal directions will be equal to zero (σ_3 = 0 MPa). On the other hand, strain (ε_z) will not be equal to zero and can be experimentally measured by determining the peak position (2θ) and solving Equation 12 for a value of d_n. If the unstrained inter-planar spacing (d_0) is known, then:

$$\varepsilon = \frac{d_n - d_0}{d_0} \qquad \text{Equation 14}$$

Thus, comparing the unstressed lattice inter-planar spacing with the strained inter-planar spacing it is possible to measure the strain near the surface of the material. However, this requires the precise measurement of an unstrained sample of the material. The formula for measurements taken normal to the surface is presented in the Equation 14. Measurements of planes at an angle (ψ) can be made altering the tilt of the specimen inside the diffractometer (Equation 14). Using Equation 15, it is possible to calculate the tensions along this tilt direction.

$$\varepsilon = \frac{d_{\phi\psi} - d_0}{d_0} \qquad \text{Equation 15}$$

Figure 14 shows an angle $\phi\psi$ to the surface and planes parallel to the surface of the material. This demonstrates how to measure planes at a certain angle to the surface by tilting the specimen. Thus, the planes are brought into a position where they satisfy Bragg's Law [76].

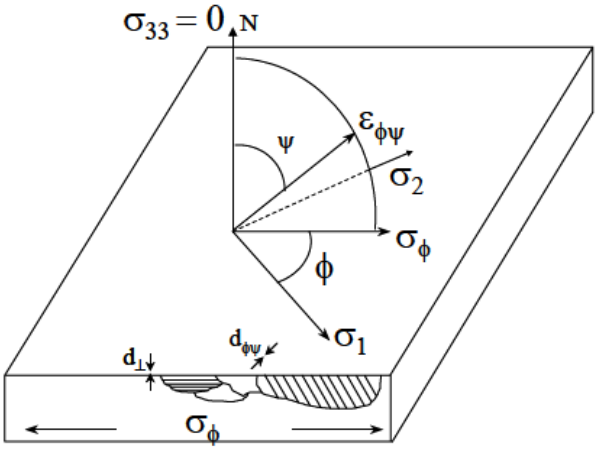

Figure 14- Scheme showing diffraction planes parallel to the surface and at an angle $\varphi\psi$. Note σ_1 and σ_2 both lie in the plane of the specimen surface [76]**.**

3.2.1.5. Stress Determination

Although it is useful to know the strains within the material, it is important to identify the stresses that are linked to these strains. From Hooke's law, that the stress is equal to the product of strain and Young's modulus E_Y [76]:

$$\sigma_y = E_Y \varepsilon_y \qquad \text{Equation 16}$$

A tensile force producing a strain in the X-direction can generate a strain in the transverse directions and not only a linear strain in that direction. Assuming a state of plane stress exists, i.e. σ_z = 0 and that stresses are biaxial, the ratio of the transverse to longitudinal strain is Poisson's ratio (v) [76]:

$$\varepsilon_x = \varepsilon_y = -\nu\varepsilon_z = \frac{-\nu\sigma_y}{E_Y} \quad \text{Equation 17}$$

If at the surface of the material, where the X-ray measurement is considered to be made, $\sigma_z = 0$, then [76]:

$$\varepsilon_z = -\nu\left(\varepsilon_x + \varepsilon_y\right) = \frac{-\nu}{E_Y}(\sigma_x + \sigma_y) \quad \text{Equation 18}$$

Thus, combining Equation 14 and Equation 18 [76],

$$\frac{d_n - d_0}{d_0} = \frac{-\nu}{E_Y}(\sigma_x + \sigma_y) \quad \text{Equation 19}$$

In Equation 19 only the sum of the principal stresses can be obtained. Thus, the precise value of d_0 is still required.

To measure a single stress acting in some direction of the surface $\sigma\varphi$, it is necessary to consider the elasticity theory for an isotropic solid, which shows that the strain along an inclined line (m_3 in Figure 13) is [76]:

$$\varepsilon_{\phi\psi} = \frac{1+\nu}{E_Y}(\sigma_1 cos^2\phi + \sigma_2 sin^2\phi)sin^2\psi - \frac{\nu}{E}(\sigma_1 + \sigma_2) \quad \text{Equation 20}$$

Considering the strains in terms of inter-planar spacing, and the use of the strains to evaluate the stresses, it is possible to demonstrate that [76]:

$$\sigma_\psi = \frac{E_Y}{(1+\nu)sin^2\psi}\left(\frac{d_\psi - d_n}{d_n}\right) \quad \text{Equation 21}$$

Equation 21 allows the calculation of the stress in any chosen direction from the inter-planar spacing determined from two measurements, made in a normal plane to the surface and containing the direction of the stress to be measured.

The method for stress determination most commonly used is the $sin^2\psi$ method. It consists of several XRD measurements that are performed at different psi tilts (Figure

14). The inter-planar spacing (or *2*θ peak position), is measured and plotted as a curve like the one shown in Figure 15 [76].

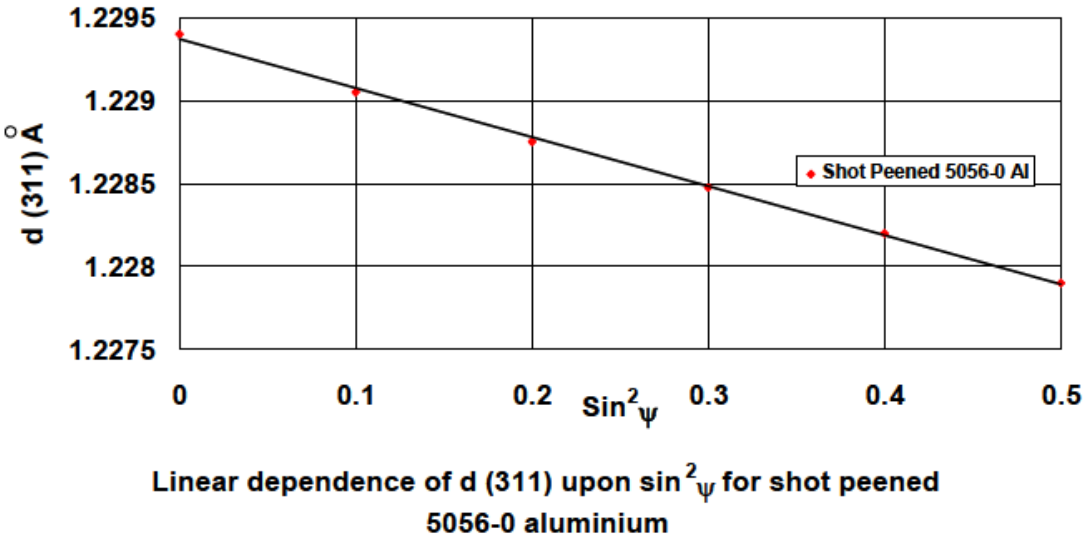

Figure 15- Example of a *d* vs *sin²ψ* plot [76]**.**

From the plotted graph (Figure 15) it is possible to obtain the stress, calculating the gradient of the line and with basic knowledge of the elastic properties of the material. This assumes a zero stress at $d = d_n$, where *d* is the interception on the y-axis when $sin^2\psi = 0$.

Thereby the stress is given by [76]:

$$\sigma_\phi = \left(\frac{E_Y}{1+\nu}\right) m \qquad \text{Equation 22}$$

where *m* is the gradient of *d versus* $sin^2\psi$ curve (Figure 15) [76].

In this study, the value of KNN Young's modulus of 104 GPa and the KNN Poisson's ratio of 0.27 was used [26][29]. The tests consisted of sequentially θ/2θ measurements with a 0.02° step width and 5 seconds of counting time per step in 29.5°-33°, for ψ values ranging from -70° to 70°, in a Philips X'Pert MRD equipment.

3.2.2. Microstructure Analysis

3.2.2.1. Scanning Electron Microscope (SEM)

SEM is used to generate high-resolution images of shapes of objects and to show spatial variations in chemical compositions. This equipment is also used to identify phases based on qualitative chemical analysis and/or crystalline structure. SEM is a type of electron microscope that images the sample surface by scanning it with a high-energy beam of electrons in a raster scan pattern (Figure 16). The electrons interacting with the atoms that constitute the sample, end up producing signals that contain data about the composition, sample's surface topography and other properties. Electron microscope consist of an electron source, an accelerating high voltage structure, electromagnetic lenses, a specimen and detectors enclosed in a column that is evacuated in order to stop the electrons being scattered by gas molecules [72].

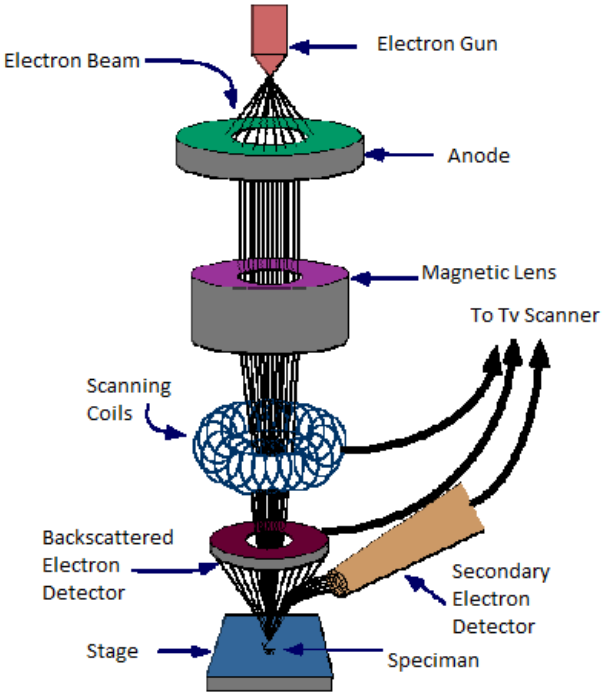

Figure 16- Schematic drawing of SEM [72].

In this dissertation, SEM was used to determine the thickness of the films and characterize the surface and interface between the substrates and the films (density,

defects, *etc*.). Regarding the interface study, cross-sections of the films were prepared. Thus, film samples were cut and pasted in a sample holder using a conductive carbon paste for SEM analysis. The samples were oriented facing up and sideways in order to analyse the surface (top view) and the interface (cross section) of the films, respectively.

SEM experiments were performed using a field emission scanning electron microscope (Hitachi, S-4100), working under the electron acceleration field of 25 kV.

3.2.2.2. Atomic Force Microscopy (AFM)

Surface morphology of KNN thin films was also studied by Atomic Force Microscopy (AFM) using a commercial AFM equipment (Multimode Nanoscope IIIA, Digital Instruments) in taping mode, equipped with a hard silicon conducting tip was used to examine the surface structure of the studied films. The topography images were processed using WSxMbeta6_0 software.

The atomic force microscope is a high-resolution type of scanning probe microscope. This type of microscope has the ability to demonstrate resolutions of fractions of a nanometre (Figure 17).

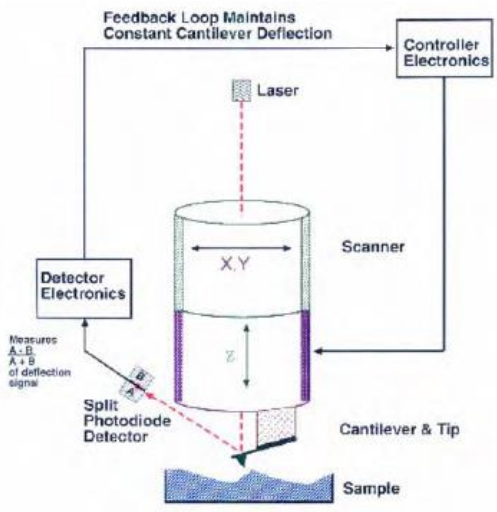

Figure 17- Schematic diagram showing the operating principles of the atomic force microscope in the contact mode [72]**.**

The AFM uses a microscale cantilever (typically silicon or silicon nitride) with a sharp tip (probe) at its end, which is used to scan the specimen surface. According to

Hook's law, when the tip is close to the sample surface, the forces between the tip and the sample lead to a deflection of the cantilever. Some forces can be measured in AFM including mechanical contact force, Van der Waals forces, chemical bonding, *etc*. It is also possible to use specialised types of probe to measure, simultaneously, additional quantities as well forces. Typically, the deflection is measured using a laser spot reflected from the top surface of the cantilever into an array of photodiodes.

For fragile samples, AFM can perform non-contact scans using a tip attached to the end of an oscillating cantilever across the sample surface. In this type of performance, the tip oscillates above the absorbed fluid layer on the surface during scanning, without touching the surface area [72][81].

In this study, the surface microstructure of KNN films was analysed by atomic force microscope (AFM) in contact mode. In this mode, AFM works by bringing a cantilever tip in contact with the surface to be imaged. An ionic repulsive force from the surface applied to the tip bends the cantilever upwards. To calculate the force, it is considered the amount of bending, measured by a laser spot reflected onto a split photo detector. Maintaining the force constant while scanning the tip across the surface, allows the vertical movement of the tip to follow the surface profile, which is recorded as the surface topography by the AFM.

Using the obtained SEM and AFM topography images the average grain size was calculated by the linear technique with the Equation 23:

$$\bar{G} = 1.5\frac{\sum L}{N} \qquad \text{Equation 23}$$

where $\bar{G}$ stands for average grain size, *L* stands for linear grain intercept distance and *N* stands for the number of grains intercepted per unit test length.

3.3. Electrical Measurements

Dielectric properties were determined on metal/film/metal capacitors. Platinum (Pt) was used as the bottom electrode and gold (Au) was used as the top electrode material. The Au electrodes were deposited at the top with a diameter of 600 µm, using

a SEM coating unit (E5000, Polaron Equipment Limit) with an argon partial pressure of 2 mtorr, an acceleration voltage of 12 kV and an emission current of 12 mA.

3.3.1. Dielectric Measurements

Relative permittivity (ε_r) indicates the ability of a material to store energy and is composed of a real and an imaginary part. The former represents how much energy from an external applied field is stored in a material. The later, characterizes the dissipation of energy in the material. Piezoelectric material can be modelled as a resistor with the electrical resistance *R* and conductance G = 1/R and capacitor (C_p) in parallel (Figure 18).

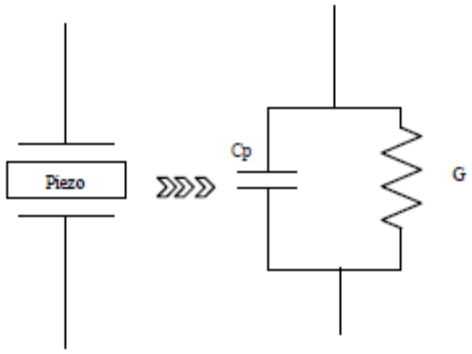

Figure 18- Electrical circuit model of a piezoelectric sample [82]**.**

Then the current passing through the piezoelectric sample (*I*) is defined as:

$$I = I_C + I_R = \left(j\omega C_p + G\right)V = j\omega C_0 \left[\frac{C_p}{C_0} - j\frac{G}{\omega C_0}\right]V = j\omega C_0 \varepsilon_r V$$

Equation 24

where I_C represents the current passing through the capacitor and I_R the current passing over the resistor, *j* stands for the imaginary operator, $\omega = 2\pi f$ stands for the angular frequency and C_0 stands for the free space capacitance:

$$C_0 = \frac{\varepsilon_0 A}{t} = C/\varepsilon_r \qquad \text{Equation 25}$$

where ε_0 is the permittivity of free space (8.85×10^{-12} F/m), A is the electrode area, and t is the sample thickness.

Then, the complex relative permittivity is defined as:

$$\varepsilon_r = \varepsilon_r' - j\varepsilon_r'' = \frac{C_p}{C_0} - j\frac{G}{\omega C_0} \qquad \text{Equation 26}$$

The real part of the permittivity is given by:

$$\varepsilon_r' = \frac{C_p}{C_0} = \frac{tC_P}{\varepsilon_0 A} \qquad \text{Equation 27}$$

The imaginary part is:

$$\varepsilon_r'' = \frac{G}{\omega C_0} = \frac{1}{\omega \mathrm{R} C_0} = \frac{t}{\omega \mathrm{R} \varepsilon_0 A} \qquad \text{Equation 28}$$

The loss tangent (*tanδ*) is the tangent of the phase angle between the real and the imaginary parts of the permittivity [83]:

$$tan\delta = \frac{\varepsilon_r''}{\varepsilon_r'} \qquad \text{Equation 29}$$

The dielectric permittivity and loss tangent measurements were carried out on the Agilent (E4980A) at 21 frequencies in the frequency range of 100 Hz to 1 MHz at room temperature. Dual impedance parameters *Z-ψ* were measured under an oscillation level of the applied voltage of 50 mV with further recalculation to:

$$\varepsilon_r' = \frac{tsin(\psi)}{\omega Z \varepsilon_0 A} \qquad \text{Equation 30}$$

and

$$tan\delta = tan(90° - \psi) \qquad \text{Equation 31}$$

3.3.2. Ferroelectric Measurements

3.3.2.1. Polarization Hysteresis Loop

The polarization versus applied electric field hysteresis (*P-E*) loop can be used to investigate the ferroelectric behaviour of the fabricated KNN thin film. The ferroelectric materials belong to a class of piezoelectrics, in which KNN is included. The dielectric polarization describes the behaviour of a material under an applied electric field and can be determined as the dipole moment per unit volume. A typical *P*(*E)* hysteresis loop of ferroelectrics is shown in Figure 19.

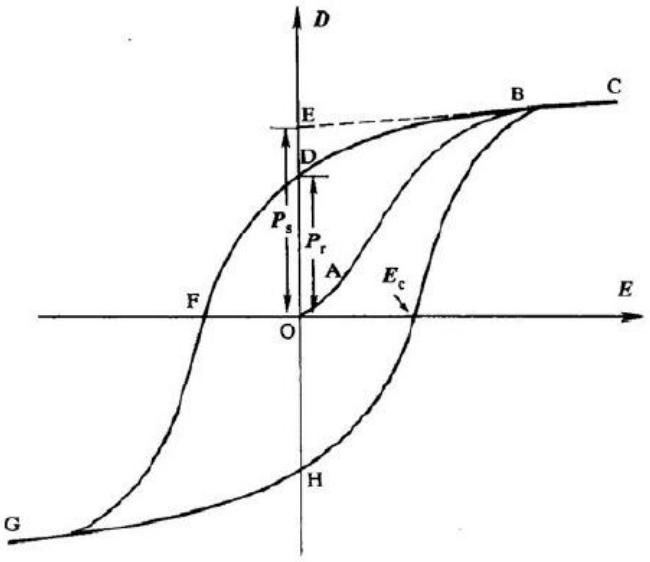

Figure 19- Typical *P*(*E)* hysteresis loop of ferroelectric materials [72]**.**

Figure 19 shows that initially the unpoled ferroelectric materials have zero polarization (point *O*). The spontaneous polarization directions of domains will be forced towards the field direction, when the electrical field increases, which eventually results in a rapid increase in polarization (segment *OAB*).

When all the domains are aligned as close as possible to the field direction it is reached a saturation state (*BC*). A linear dielectric and piezoelectric response is represented by the linear extrapolation of the segment *BC* back to the polarization axis

(*CBE*). Appropriately oriented single crystals may provide such a stable polarization state.

The saturated polarization (P_s) corresponds to the polarization value at point *E*, which is the volume averaging of the spontaneous polarization of all domains. The remnant polarization (P_r) is the moment when the field strength decreases and the polarization decreases to point *D* (*BD*). This value is smaller than P_s but different from zero, since for piezoceramics some of the domains will be reoriented due to grain and domain interaction and some will remain aligned.

Until the applied field in the opposite direction reaches a certain value (point *F*), the remnant polarization holds (poling state). The coercive field (E_c) is the strength of the field required to reduce the polarization back to zero. Further increase of the field will induce an alignment of the dipoles in this direction. Reversing the field direction once again leads to a close cycle and the relation of *P* and *E* is represented by hysteresis loop (Figure 19) [72].

The hysteresis loop measurement was performed using the ferroelectric analyser *TF Analyzer* 2000 aixACCT. *P(E)* hysteresis loop normally runs at low frequencies. The input parameters selected to control the hysteresis measurement include a frequency, a variable amplitude of the driving voltage, a signal waveform and a number of point recorded to plot the loop. The current applied to the films was controlled by the acquisition software.

3.3.2.2. Local Analysis of Ferroelectric Domains

Via the so-called piezoelectric force microscopy (PFM) it is possible to analyse the local ferroelectric domains of KNN thin films. The operation of PFM is based on the detection of local piezoelectric deformation of a ferroelectric sample induced by an external electric field. In piezoelectric samples this field causes thickness changes and vibrations of the surface, which lead to oscillations of the cantilever that can be read out with a lock-in amplifier (Figure 20). The different orientations of the polar axis of adjacent domain lead to a contrast in PFM measurements, which mean the domains are displayed as bright and dark areas in PFM images [84].

In this study, a modified commercial atomic force microscope (Multimode, Nanoscope IIIA, Digital Instruments) was employed. A conductive *Pt* coated *Si* tip-cantilever system was used for the application of external voltages and for vibration detection. Applying an external *AC* voltage between the PFM tip and KNN thin films, these were excited at the bottom electrode. Thus, the deflection signal from the cantilever was detected by a lock-in amplifier. A topographic image of the film surface was taken simultaneously with the domain image. In the piezoelectric image, domains with opposite polarities exhibit different contrast.

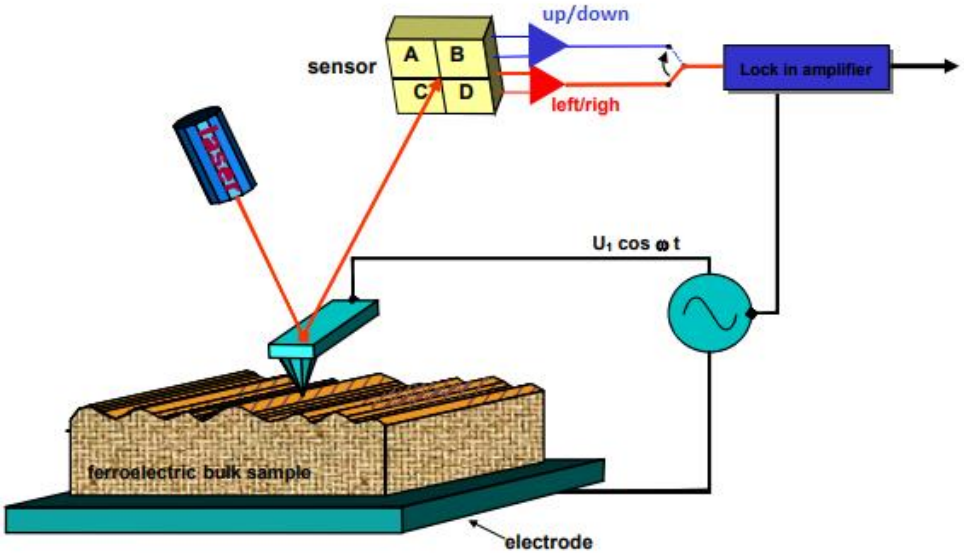

Figure 20- Typical PFM setup [84]**.**

4. Results and Discussion

In this chapter, structure and microstructure of thin KNN films deposited by the sol-gel method on several substrates, such as Si/SiO_2, polycrystalline Al_2O_3, $Si/SiO_2/TiO_2/Pt$, Al_2O_3/Pt and $SrTiO_3/Pt$ are presented. Some characteristics of the substrates are shown in Table 6. The room temperature dielectric response as a function of the frequency (*f*), hysteresis *P(E)* loops and local piezoresponse are also presented for the films deposited on platinised substrates.

Table 6- Lattice parameters and Thermal Expansion Coefficients (TEC's) of the substrates used in the current work (data from the supplier company), Pt [72] **used as electrode and bulk KNN** [46][85]**.**

	Al_2O_3	**Si**	**$SrTiO_3$**	**Pt**	**KNN**
Lattice parameter (Å)	3.730	3.841	3.903	3.912	a= 3.994 b= 4.016 c= 3.935
TECx10^{-6}/°C	7.7	2.3	9	9	4.72

4.1. Preparation and Characterization

Using four different solutions of KNN, layers of sol-gel were deposited on Si/SiO_2, polycrystalline Al_2O_3, $Si/SiO_2/TiO_2/Pt$, Al_2O_3/Pt and $SrTiO_3/Pt$ substrates by spin-coating and, after drying, all the obtained films were annealed at 750°C for 5 minutes in air.

Different tools were used for the characterization of KNN films. The structure, phase content and microstructure of the films were analysed by X-ray Diffraction (XRD), Atomic Force Microscopy (AFM) and Scanning Electron Microscopy (SEM). Impedance Analysers were used to measure room temperature dielectric permittivity and dielectric losses of KNN films on platinized substrates as a function of frequency. The *P-E* loops of these films were traced by a ferroelectric tester. Piezoelectric force microscopy (PFM) was used for the imaging of local ferroelectric domain structure.

4.2. Structural Characterization

4.2.1. Crystal Structure

The XRD patterns were obtained from low incident beam angle experiments with the purpose to omit the substrate response from the spectra of the studied films. XRD patterns in Figure 21-23 illustrate the phase formation and assemblage for KNN films derived from two solutions with 5% excess of potassium and 20% excess of potassium and sodium.

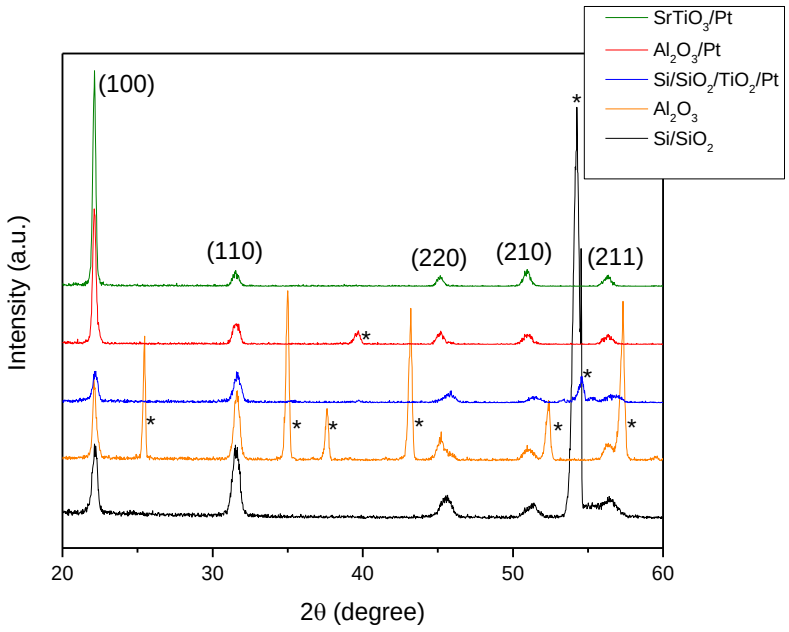

Figure 21- XRD patterns of KNN films prepared from solutions with 20% excess of potassium and sodium and 0.4 M concentration, deposited on different substrates. Substrate peaks are marked by *.

XRD patters of KNN films with 20% excess and 0.4 molar concentration are shown in Figure 21. According to the diffraction peaks of the standard powder samples of $KNbO_3$ (JCPDS #04-14-0625) and $NaNbO_3$ (JCPDS #04-005-7334), it was noticed that all the films have well crystallized perovskite phase and no other phases were detected. Analysing the XDR patterns of the films deposited on the substrates of Si/SiO_2, polycrystalline Al_2O_3 and $Si/SiO_2/TiO_2/Pt$ the perovskite structure, which is defined as pseudo-cubic structure (*Pm-3m* space group), was identified and no preferential

orientation or textured structure was detected. However, in the case of the Al_2O_3/Pt and $SrTiO_3$/Pt substrates, intense (100) peaks were observed, implying that these films have preferential crystallographic orientation. The (100) preferential orientation can be attributed to the lowest surface energy of (100) faces in a perovskite cell [50].

Figure 22 shows the XRD patterns of the films prepared from the solution with 20% excess of potassium and sodium but with 0.2 molar concentration. Although the solution was diluted, the films show no significant changes in the XRD pattern, continuing to present a pure perovskite structure and no secondary phases. Analysing the XRD patterns, the KNN films deposited on $SrTiO_3$/Pt and Al_2O_3/Pt substrates continue to present a more intense (100) peak in their patterns.

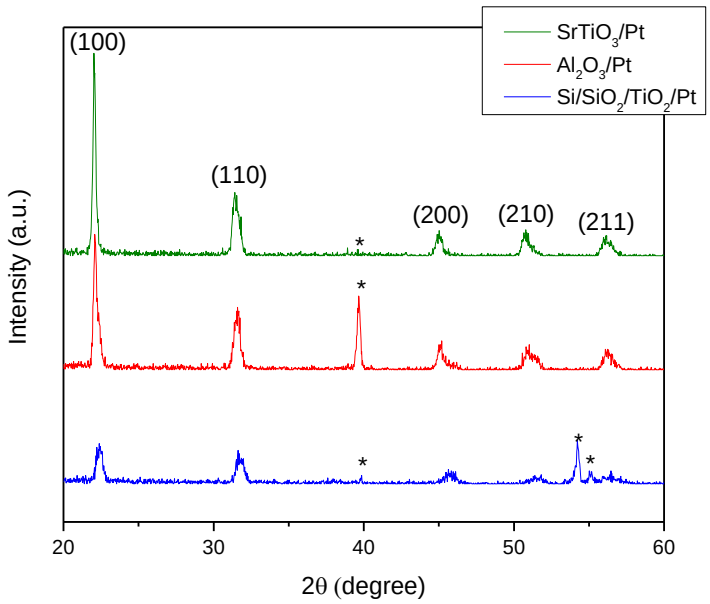

Figure 22- XRD patterns of KNN films prepared from solutions with 20% excess of potassium and sodium and 0.2 M concentration, deposited on different substrates. Substrate peaks are marked by *.

Figure 23 presents the XRD patterns of the films prepared from solution with 5% excess of potassium and 0.2 molar concentration, which were deposited on $Si/SiO_2/TiO_2/Pt$, Al_2O_3/Pt and $SrTiO_3$/Pt substrates. The XRD patterns also show pure perovskite peaks with pseudo-cubic structure, without secondary phases. However, in contrast to the solution with higher alkali ions excess, no clear crystallographic orientation was detected.

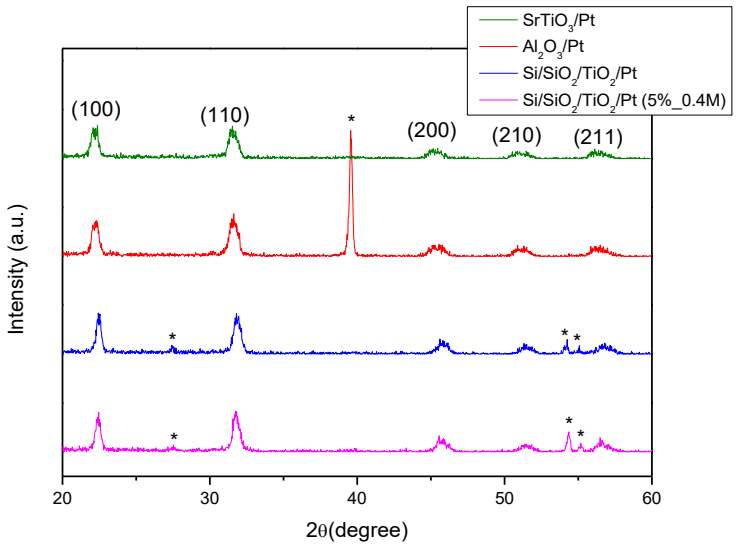

Figure 23- XRD patterns of KNN films prepared from solutions with 5% excess of potassium as well as 0.4 M and 0.2 M concentrations, deposited on different substrates. Substrate peaks are marked by *.

XRD pattern of the film prepared from KNN solution with 5% excess of potassium and 0.4 molar concentration, which was only deposited on $Si/SiO_2/TiO_2/Pt$ substrate, is shown in Figure 23 as well. In this XRD pattern, the presence of pure perovskite peaks, without preferential orientation is also observed.

Thus, all XRD patterns demonstrate peaks corresponding to perovskite structure (Figure 21-23). No significant differences were detected, comparing the XRD patterns of the solutions with the same alkali excess but different molar concentration. Analysing the differences between the films with different alkali excesses, the XRD patterns of the films with 20% excess have preferential (100) crystallographic orientation, whereas the films with 5% excess are rather randomly orientated. At the same time, KNN films with 20% excess of potassium and sodium present XRD patterns with more intense peaks, which is associated to a greater crystallization of these films. The absence of secondary phases for both solutions with different alkali ion excess can be explained by the insensitivity of XRD to the phases formed by the excess. XRD can only detect the alkali poor phase, formed due to the high volatility of K and Na ions during the heat treatment [48]. Tanaka *et al.* [51] reported that sodium-poor secondary phases can be formed most easily due to the volatilization rate of Na_2O being higher than that of K_2O [48].

Assuming that all the films have perovskite pseudo-cubic structure (a=b=c), the out-of-plane lattice parameter was calculated based on the peaks that appeared at about 22.1º, 31.5º, 45.2º, 50.8º and 56.1º. Table 7 shows the lattice parameters of the KNN films deposited on Si/SiO_2, polycrystalline Al_2O_3, $Si/SiO_2/TiO_2/Pt$, Al_2O_3/Pt and $SrTiO_3/Pt$ substrates.

Table 7- Out-of-plane lattice parameters of different KNN films deposited on Si/SiO_2, polycrystalline Al_2O_3, $Si/SiO_2/TiO_2/Pt$, Al_2O_3/Pt and $SrTiO_3/Pt$ substrates.

KNN films		Substrate	Lattice parameter (Å)
% Excess	Molar concentration		
20+20	0.4	Si/SiO_2	~3.986 ± 0.003
20+20	0.4	polycrystalline Al_2O_3	~4.017 ± 0.011
20+20	0.4	$SrTiO_3/Pt$	~4.013 ± 0.002
20+20	0.4	Al_2O_3/Pt	~4.012 ± 0.004
20+20	0.4	$Si/SiO_2/TiO_2/Pt$	~3.941 ± 0.015
20+20	0.2	$SrTiO_3/Pt$	~4.028 ± 0.007
20+20	0.2	Al_2O_3/Pt	~4.017 ± 0.004
20+20	0.2	$Si/SiO_2/TiO_2/Pt$	~3.949 ± 0.017
5	0.2	$SrTiO_3/Pt$	~4.006 ± 0.006
5	0.2	Al_2O_3/Pt	~4.000 ± 0.009
5	0.2	$Si/SiO_2/TiO_2/Pt$	~3.957±0.001
5	0.4	$Si/SiO_2/TiO_2/Pt$	~3.970±0.007

XRD patterns can be used to quantify the crystallographic texture of the film, calculating the Lotgering factor (*f*) as described in Chapter 2. Table 8 shows the texture degree (Lotgering factor, *f*) present in the KNN thin films, which showed a higher intensity in the peak (100) at the XRD patterns. The table shows that the $f_{(100)}$ in the KNN thin films with 5% excess deposited on Al_2O_3/Pt is 12.77% and it increases to 71.90% with the increasing amount of potassium and sodium excess in the solution. The $f_{(100)}$ increases from 15.03% to 75.09% with the increasing amount of potassium and sodium excess in the film, in the case of KNN thin films deposited on $SrTiO_3/Pt$. Such high values as 71.90% and 75.09% indicate significant texturing of the films along (100)

crystallographic direction, whereas moderate values, such as 1.74-17.40% obtained for films deposited on $Si/SiO_2/TiO_2/Pt$ imply rather random orientation.

Table 8- Texture degree (Lotgering factor, *f*) of different KNN thin films deposited on: $Si/SiO_2/TiO_2/Pt$, Al_2O_3/Pt and $SrTiO_3/Pt$ substrates.

KNN films		Substrate	Lotgering Factor ($f_{(100)}$(%))
% Excess	Molar concentration		
20+20	0.4	$SrTiO_3/Pt$	75.09
20+20	0.4	Al_2O_3/Pt	71.90
20+20	0.4	$Si/SiO_2/TiO_2/Pt$	15.59
20+20	0.2	$SrTiO_3/Pt$	54.93
20+20	0.2	Al_2O_3/Pt	38.64
20+20	0.2	$Si/SiO_2/TiO_2/Pt$	17.40
5	0.2	$SrTiO_3/Pt$	15.03
5	0.2	Al_2O_3/Pt	12.77
5	0.2	$Si/SiO_2/TiO_2/Pt$	15.85
5	0.4	$Si/SiO_2/TiO_2/Pt$	1.74

In order to completely characterize the texture quality, pole figure measurements, which reflect the preferred orientation of the crystal lattice in the material, were performed. The (100) X-ray pole figures of KNN thin films with 20% excess and 0.4 M concentration, 20% excess and 0.2 M concentration and 5% excess and 0.2 M concentration are shown in Figure 24, Figure 25 and Figure 26, respectively. For the KNN thin film with 20% excess and 0.4 M concentration and particularly with 20% excess and 0.2 M concentration, the projected intensities are all grouped in a central circle near a tilt angle of 0°. It is an indication that these films are oriented along (100), as XRD patterns suggested. In contrast, for KNN thin films with 5% excess and 0.2 M concentration, pole figures show the most diffuse distribution of the lines indicating absence of the preferred crystallographic orientation along (100).

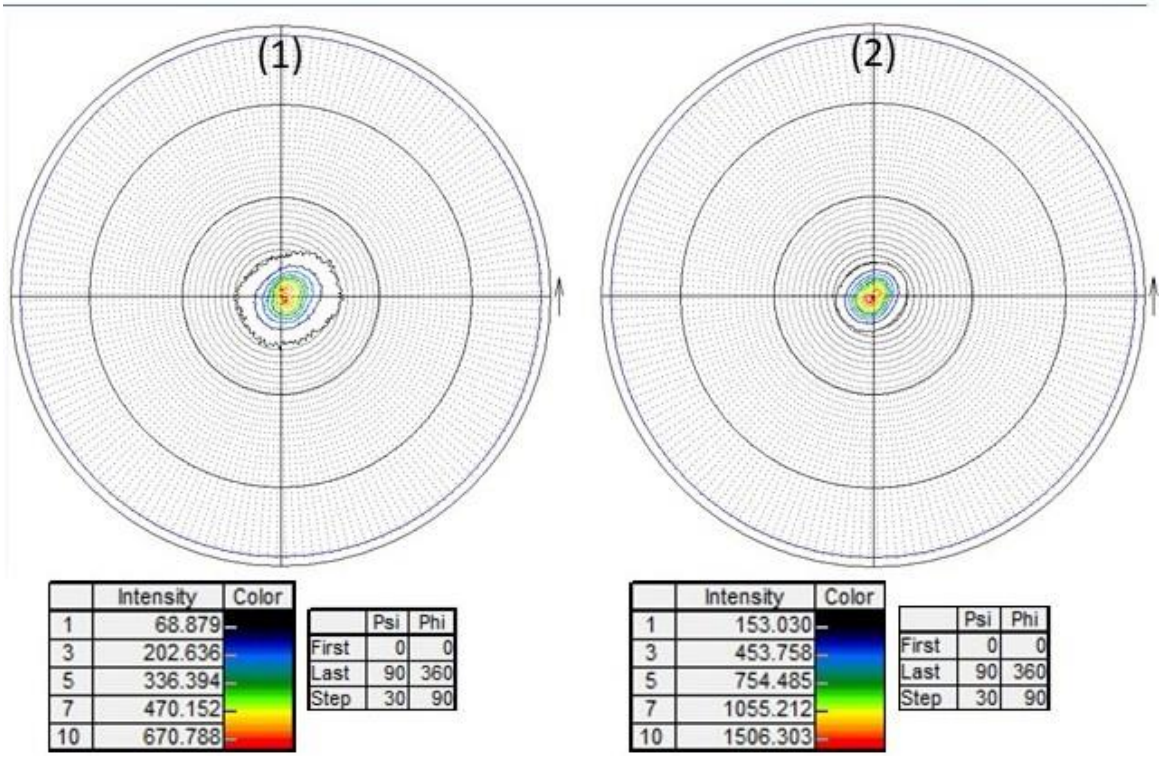

Figure 24- Pole figures of KNN thin films with 20% excess and 0.4 M concentration deposited on (1) Al_2O_3/Pt and (2) $SrTiO_3$/Pt measured for (100) plane.

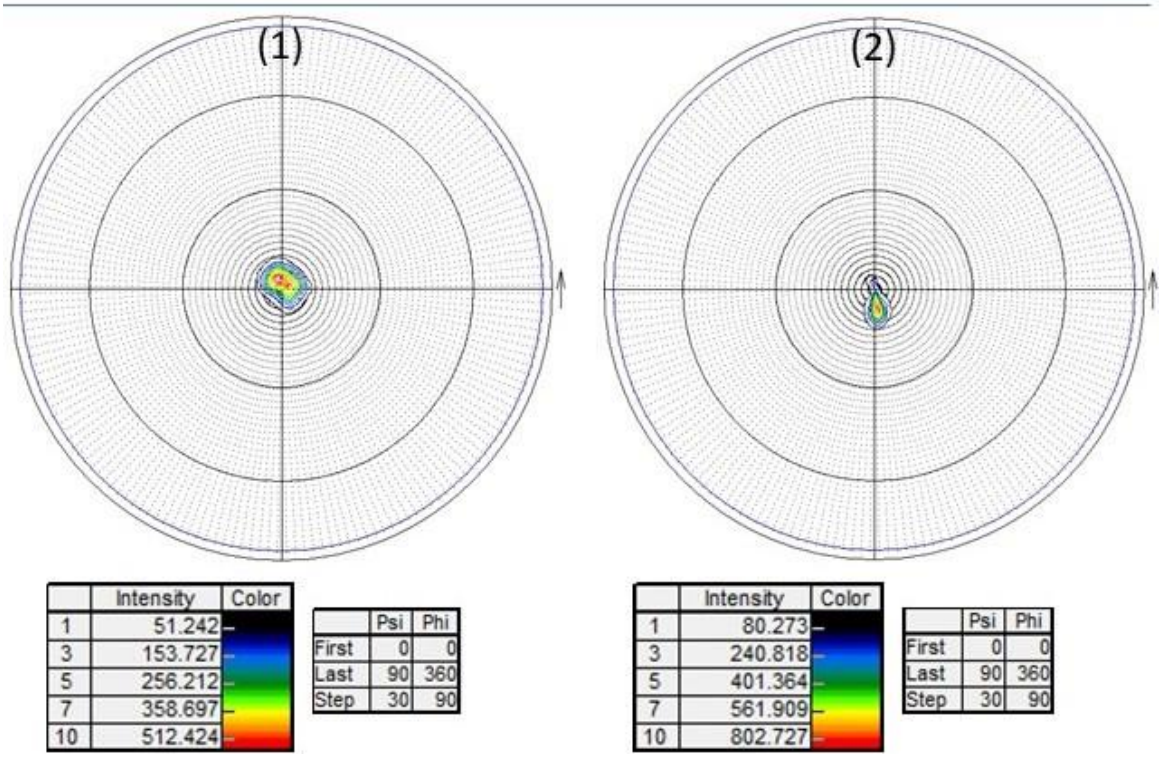

Figure 25- Pole figures of KNN thin films with 20% excess and 0.2 M concentration deposited on (1) Al_2O_3/Pt and (2) $SrTiO_3$/Pt measured for (100) plane.

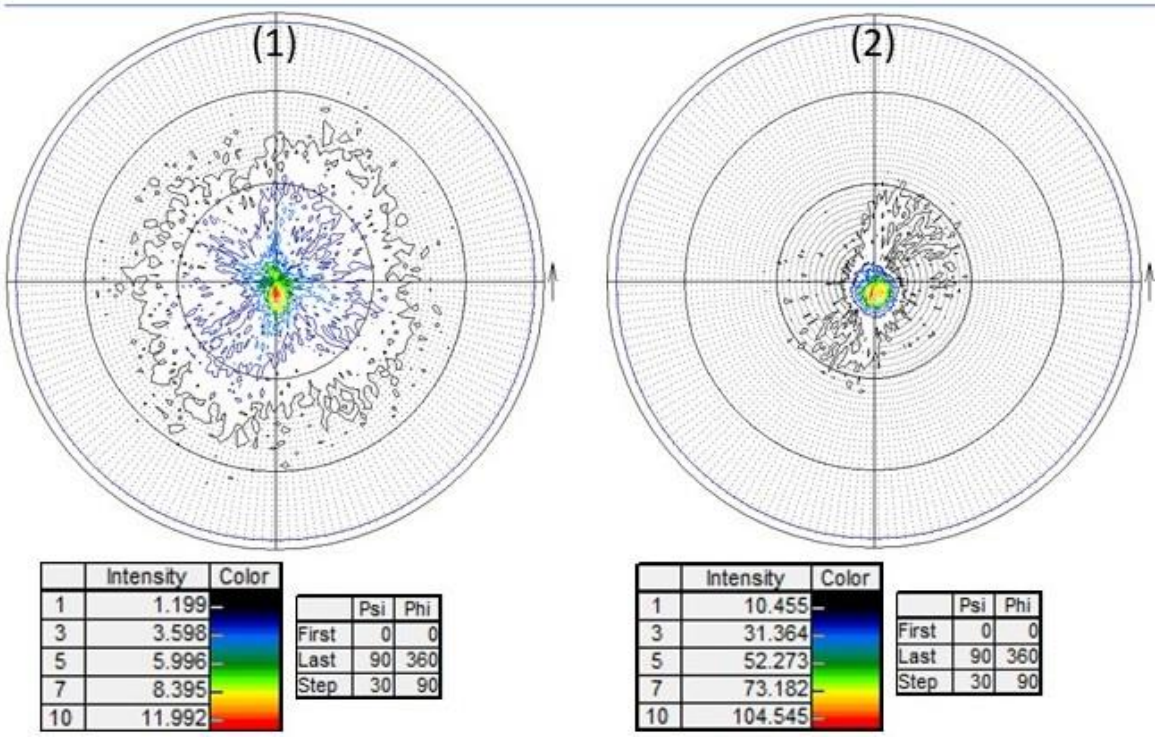

Figure 26- Pole figures of KNN thin films with 5% excess and 0.2 M concentration deposited on (1) Al_2O_3/Pt and (2) $SrTiO_3$/Pt measured for (100) plane.

4.2.2. Strain Measurements and Stress Calculations

Strain measurements were conducted by the XRD $sin^2\psi$ method, as previously described in Chapter 2. Thus, the lattice spacings *d* of a specific *(hkl)* plane were measured at different tilt angles ψ (inclined exposure). The linear variations of the corresponding strains induced in the KNN films by different substrates are presented in Figure 27.

The strains for the KNN films from solution with 20% excess of potassium and sodium and 0.4 molar concentration are presented in Figure 27 (a). The films deposited on polycrystalline Al_2O_3, Al_2O_3/Pt and $SrTiO_3$/Pt substrates present a compressive strain, which is associated to the negative linear dependence. In contrast, the positive slope verified in the KNN films prepared on Si/SiO_2 and $Si/SiO_2/TiO_2$/Pt substrates indicates a tensile strain level.

Moreover, in Figure 27 (b) the negative slope indicates that the KNN films with 20% excess of potassium and sodium and 0.2 M concentration on Al_2O_3/Pt and $SrTiO_3$/Pt

substrates have a compressive strain while the KNN films on $Si/SiO_2/TiO_2/Pt$ substrate have a tensile strain.

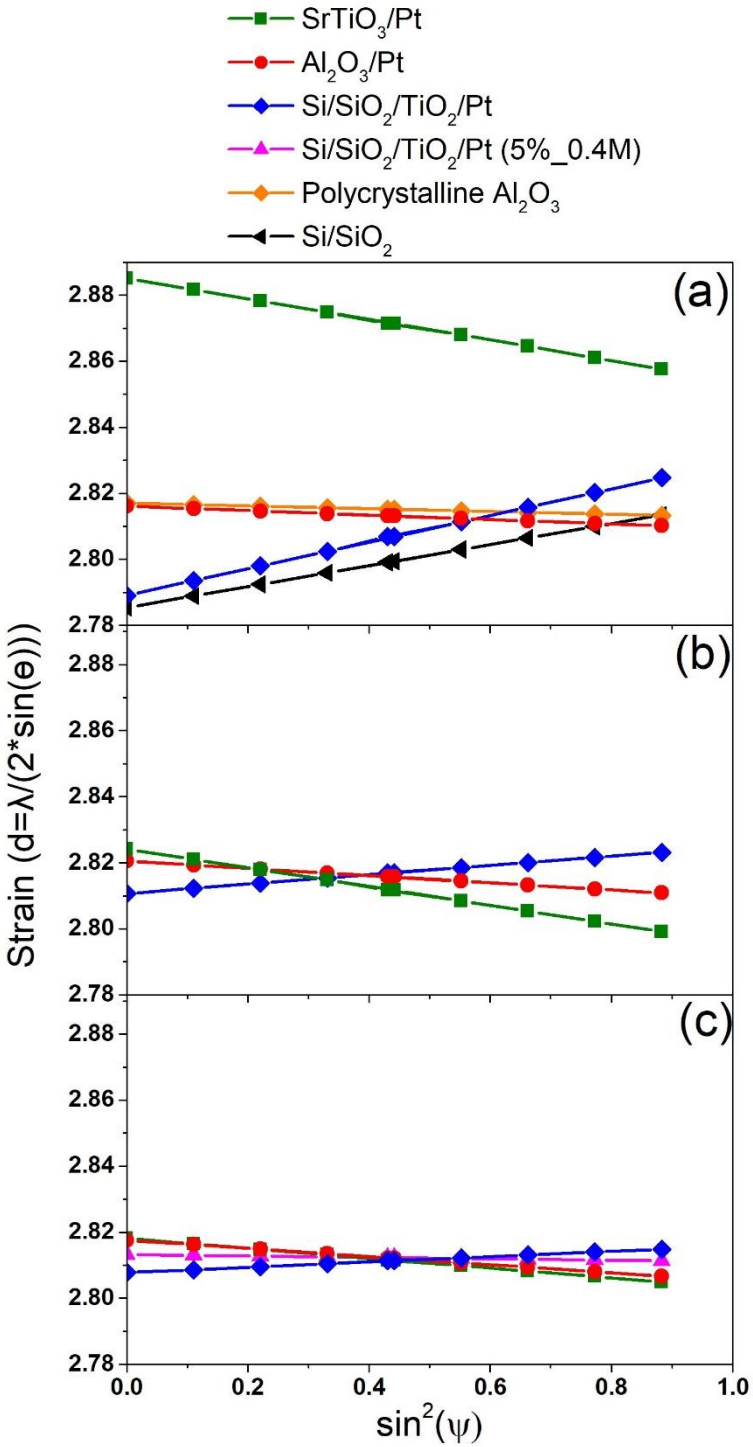

Figure 27- Strain (d=λ/(2*sin(ɵ))) of KNN films prepared from: (a) 20% excess of potassium and sodium and 0.4 M concentration, (b) 20% excess of potassium and sodium and 0.2 M concentration, (c) 5% excess of potassium and 0.2 M as well as 0.4 M concentration solutions, deposited on Si/SiO_2, polycrystalline Al_2O_3, $Si/SiO_2/TiO_2/Pt$, Al_2O_3/Pt and $SrTiO_3/Pt$ substrates.

KNN films with 5% excess of potassium and 0.2 molar concentration (Figure 27 (c)) deposited on Al_2O_3/Pt and $SrTiO_3$/Pt substrates have a compressive strain, while the strain of the KNN film deposited on Si/SiO_2/TiO_2/Pt substrate is tensile. In Figure 27 (c) the KNN film with 5% excess of potassium and 0.4 M concentration on Si/SiO_2/TiO_2/Pt substrate presents a positive slope, which is associated to a tensile strain as well.

Using the average values of the obtained strain, the stress values can be calculated through the following formula:

$$\sigma = \left(\frac{E_Y}{1+v}\right) * m \qquad \text{Equation 32}$$

where E_Y and v correspond to the Young's modulus and Poisson's ratio of the film, respectively, and m is the gradient of the d vs $sin^2\psi$ curve.

The resulting values of the average total stress for the KNN films deposited on different substrates are shown in Table 9. Comparing the different KNN films on the same substrate it is verified that the Si/SiO_2/TiO_2/Pt substrate is always characterized by a tensile stress. Furthermore, the highest tensile stress is obtained in the KNN film with 20% excess and 0.4 M concentration (~3.300 GPa).

Despite the different values of excess and molar concentration of the KNN films, Al_2O_3/Pt substrates always present moderate compressive stress values. The highest compressive stress (~-1.015 GPa) was verified in the KNN film with 5% excess and 0.2 molar concentration. Amongst the KNN films deposited on $SrTiO_3$/Pt a significant compressive stress is observed. The highest compressive stress (~-2.546 GPa) was obtained in the KNN film with 20% excess and 0.4 M concentration.

Comparing the lattice parameter values of the KNN thin films with the average total stress values, it is possible to observe that the films under in-plane compressive stress have higher out-of-plane lattice parameters and the KNN thin films with a tensile stress have lower lattice parameters (Table 7). There is also an agreement between the TEC values of the substrates used in this study and the average total stress values (Table 6). Si substrates with TEC about twice lower than that of KNN, naturally induce a tensile stress at cooling from the annealing to room temperature. On the other hand, films that have a compressive stress are deposited on the substrates with TEC values higher than

that of KNN. In the case of $SrTiO_3$, TEC is almost double of that for KNN, thus inducing a stress comparable with that from Si substrate but with different sign.

Table 9- Values of the average total stress of different KNN films deposited on Si/SiO_2, polycrystalline Al_2O_3, $Si/SiO_2/TiO_2/Pt$, Al_2O_3/Pt and $SrTiO_3/Pt$ substrates.

KNN films		Substrate	Average total stress (GPa)
% Excess	Molar concentration		
20+20	0.4	Si/SiO_2	2.604
20+20	0.4	polycrystalline Al_2O_3	-0.343
20+20	0.4	$SrTiO_3/Pt$	-2.546
20+20	0.4	Al_2O_3/Pt	-0.548
20+20	0.4	$Si/SiO_2/TiO_2/Pt$	3.300
20+20	0.2	$SrTiO_3/Pt$	-2.325
20+20	0.2	Al_2O_3/Pt	-0.892
20+20	0.2	$Si/SiO_2/TiO_2/Pt$	1.154
5	0.2	$SrTiO_3/Pt$	-1.220
5	0.2	Al_2O_3/Pt	-1.015
5	0.2	$Si/SiO_2/TiO_2/Pt$	0.655
5	0.4	$Si/SiO_2/TiO_2/Pt$	0.171

4.3. Microstructure Analysis

4.3.1. SEM Analysis

The microstructure of the KNN films deposited on Si/SiO_2, polycrystalline Al_2O_3, $Si/SiO_2/TiO_2/Pt$, Al_2O_3/Pt and $SrTiO_3/Pt$ substrates was analysed by SEM. Figure 28 presents the images related to the KNN films from the solution with 20% excess of potassium and sodium and 0.4 M concentration deposited on different substrates. The measured films thickness is about ~380 nm (Table 10). All the films used reveal a granular and irregular microstructure. However, the film deposited on the $Si/SiO_2/TiO_2/Pt$ substrate presents cracks. These might be explained by the significant difference between the coefficient of thermal expansion coefficients (TEC's) of the KNN film and the $Si/SiO_2/TiO_2/Pt$ substrate.

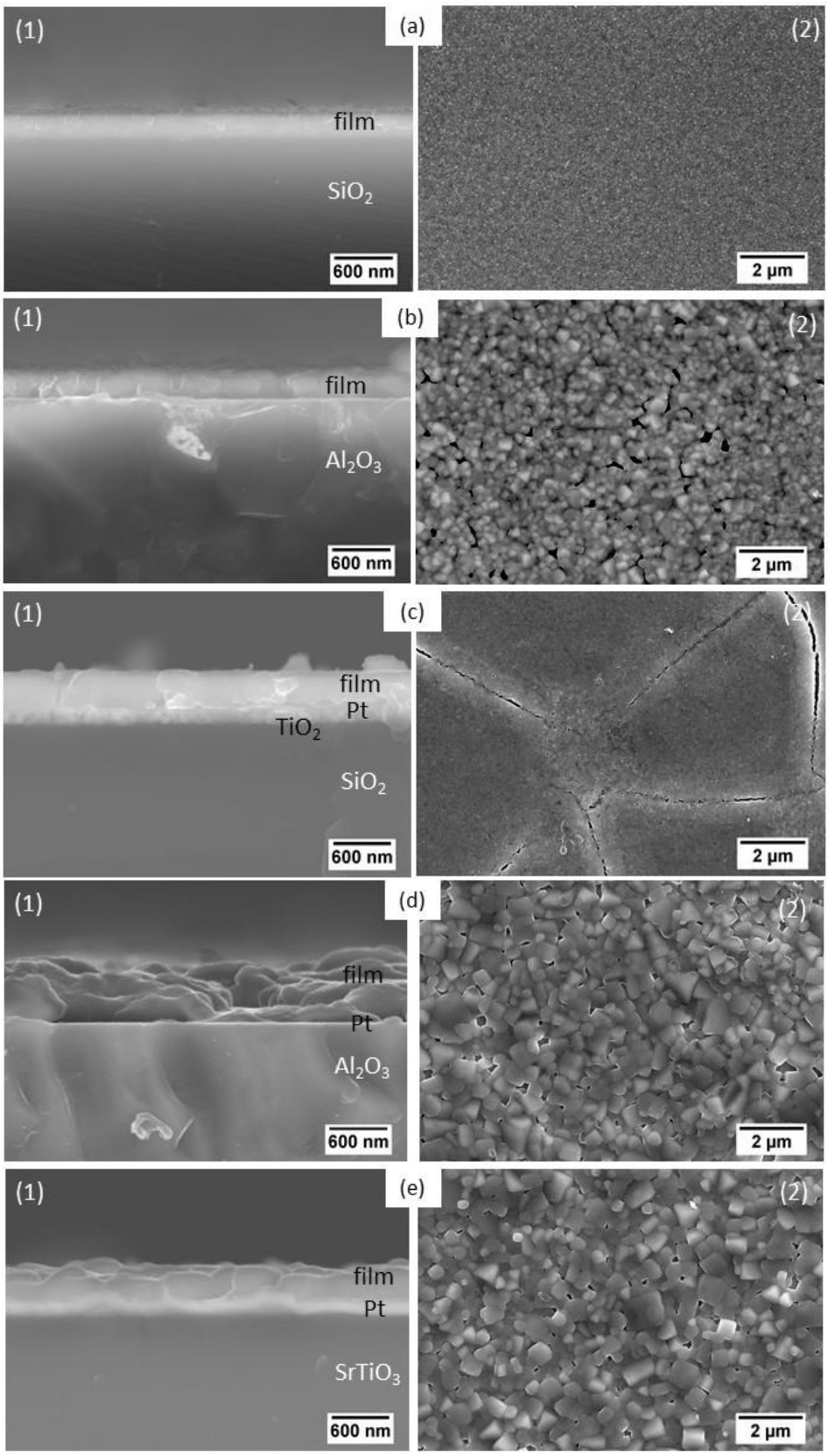

Figure 28- SEM cross-section (1) and top-view (2) micrographs of KNN thin films (20% excess of potassium and sodium and 0.4 M concentration) deposited on: (a) Si/SiO_2, (b) polycrystalline Al_2O_3, (c) $Si/SiO_2/TiO_2/Pt$, (d) Al_2O_3/Pt and (e) $SrTiO_3/Pt$ substrates.

To avoid cracks in the films, the 20% excess KNN solution was diluted from 0.4 M to 0.2 M. The KNN films from solution with 20% excess and 0.2 M concentration deposited on $Si/SiO_2/TiO_2/Pt$, Al_2O_3/Pt and $SrTiO_3/Pt$ substrates have no cracks (Figure 29). The average thickness of these films, calculated using the cross sections images, is approximately 284 nm (Table 10).

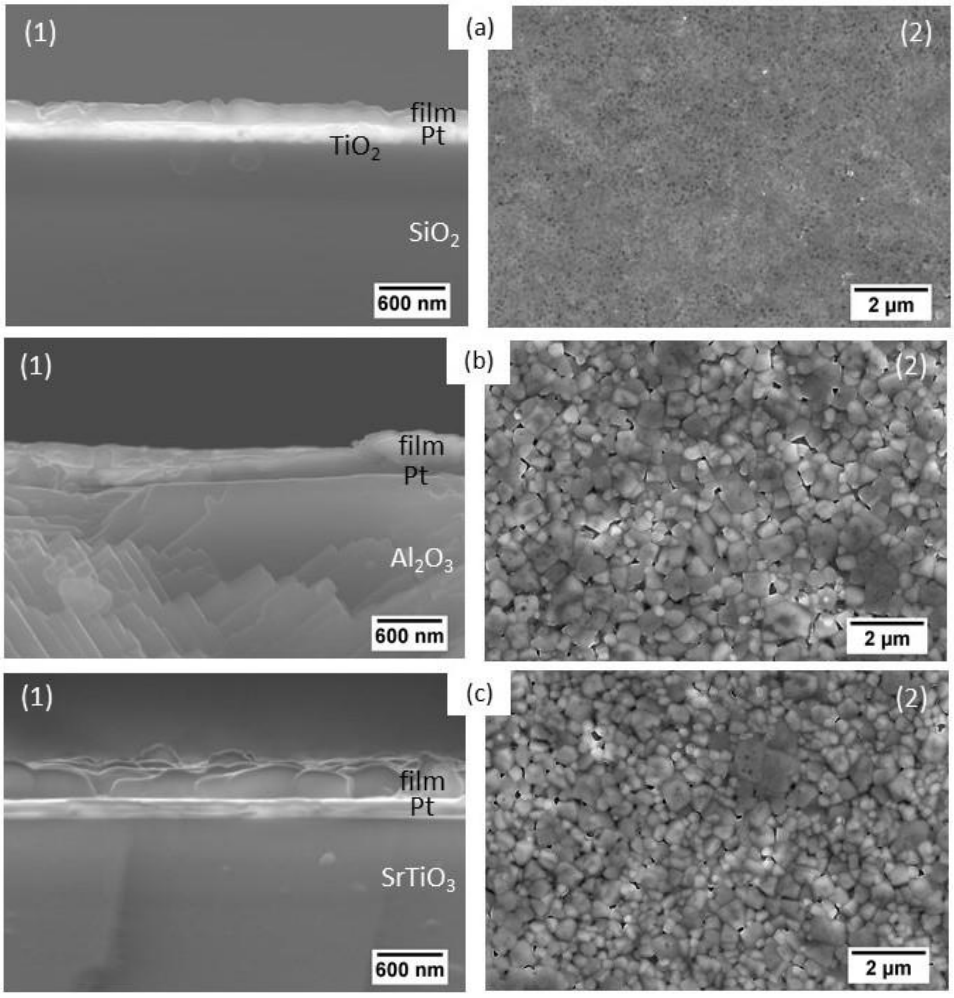

Figure 29- SEM cross-section (1) and top-view (2) micrographs of KNN thin films (20% excess of potassium and sodium and 0.2 M concentration) deposited on: (a) $Si/SiO_2/TiO_2/Pt$, (b) Al_2O_3/Pt and (c) $SrTiO_3/Pt$ substrates.

SEM cross-section and top-view micrographs of the KNN films with 5% excess and 0.2 M concentration are shown in Figure 30. All the films reveal a dense and crack free microstructure with a smooth surface. The average thickness of the film is approximately 379 nm (Table 10).

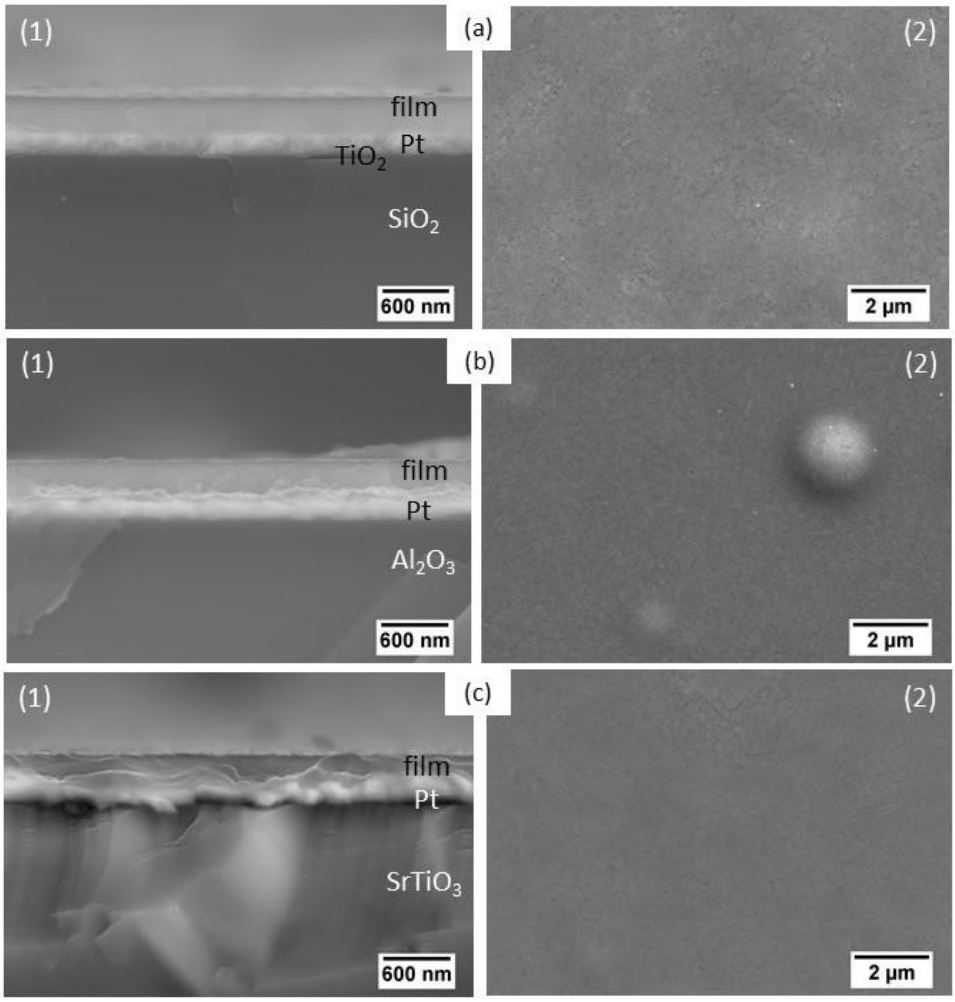

Figure 30- SEM cross-section (1) and top-view (2) micrographs of KNN thin films (5% excess of potassium and 0.2 M concentration) deposited on: (a) $Si/SiO_2/TiO_2/Pt$, (b) Al_2O_3/Pt and (c) $SrTiO_3/Pt$ substrates.

Figure 31 shows the SEM cross-sections and top-view micrographs of KNN thin films with 5% excess of potassium and 0.4 molar concentration deposited on $Si/SiO_2/TiO_2/Pt$ substrate. Due to the different thermal expansion coefficients between the KNN film and the substrate, the film presents cracks. The average thickness of the film is approximately 379 nm (Table 10).

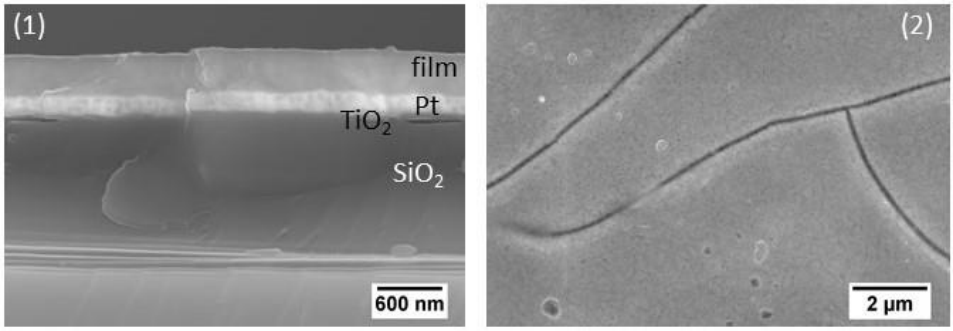

Figure 31- SEM cross-section (1) and top-view (2) micrographs of KNN thin films (5% excess of potassium with 0.4 M) deposited on Si/SiO_2/TiO_2/Pt substrate.

The average thickness of the KNN films deposited on Si/SiO_2, polycrystalline Al_2O_3, Si/SiO_2/TiO_2/Pt, Al_2O_3/Pt and $SrTiO_3$/Pt substrates is summarized in Table 10. These values were calculated from the cross-section images obtained by SEM, using the *ImageJ* program.

Table 10- Average film thickness of the different films deposited on Si/SiO_2, polycrystalline Al_2O_3, Si/SiO_2/TiO_2/Pt, Al_2O_3/Pt and $SrTiO_3$/Pt substrates.

KNN films		Substrate	Average film thickness (nm)
% Excess	Molar concentration		
20+20	0.4	Si/SiO_2	341
20+20	0.4	polycrystalline Al_2O_3	361
20+20	0.4	$SrTiO_3$/Pt	399
20+20	0.4	Al_2O_3/Pt	381
20+20	0.4	Si/SiO_2/TiO_2/Pt	420
20+20	0.2	$SrTiO_3$/Pt	329
20+20	0.2	Al_2O_3/Pt	312
20+20	0.2	Si/SiO_2/TiO_2/Pt	214
5	0.2	$SrTiO_3$/Pt	382
5	0.2	Al_2O_3/Pt	424
5	0.2	Si/SiO_2/TiO_2/Pt	333
5	0.4	Si/SiO_2/TiO_2/Pt	379

4.3.2. AFM Analysis

The in-plane surface morphology (Figure 32 *left pictures*) and corresponding 3D views (Figure 32 *right pictures*) of KNN films with 20% excess of potassium and sodium and 0.4 molar concentration deposited on $Si/SiO_2/TiO_2/Pt$, Al_2O_3/Pt and $SrTiO_3/Pt$ substrates were analysed by AFM.

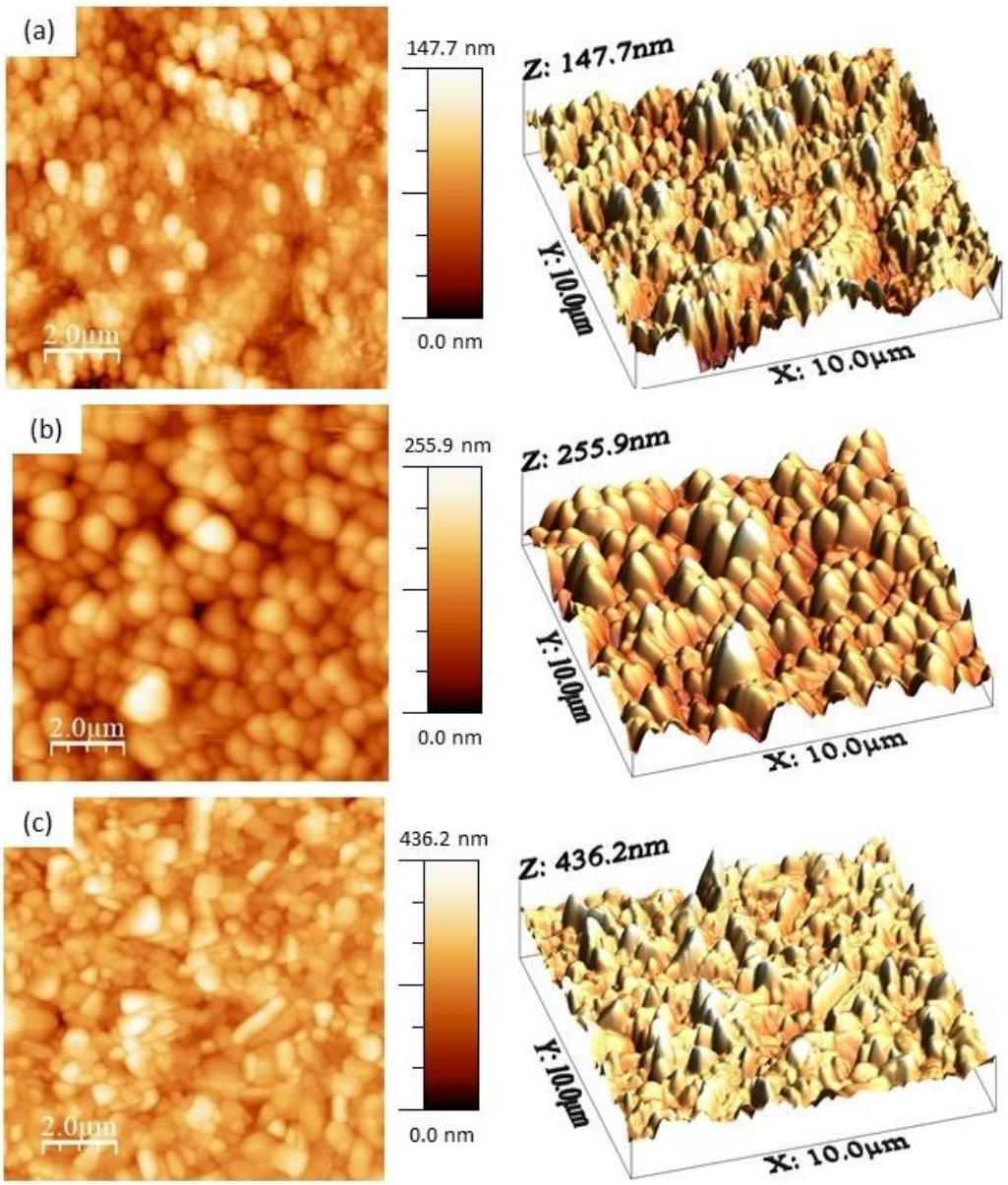

Figure 32- Atomic force micrographs of KNN thin films (20% excess with 0.4 M concentration) deposited on: (a) $Si/SiO_2/TiO_2/Pt$, (b) Al_2O_3/Pt and (c) $SrTiO_3/Pt$ substrates. Scan areas are 10x10 µm.

The analysed KNN films (20% excess with 0.4 M) deposited on different substrates exhibit grains in *x,y,z*-directions (Figure 32 *left pictures*). The in-plane grain size of the films was calculated from these AFM micrographs and is presented in Table 11.

The smallest in-plane average grain size (*G*) is ~211 nm and was found in KNN films deposited on $Si/SiO_2/TiO_2/Pt$ substrate. For $SrTiO_3/Pt$ substrate it is ~493 nm. The KNN film on Al_2O_3/Pt substrate has the highest average grain size (~603 nm).

The roughness of the films is also presented in Table 11. All the films have high root mean square (RMS) roughness. The smallest RMS roughness (~19.46 nm) was calculated from the KNN on $Si/SiO_2/TiO_2/Pt$ substrate, corresponding to the smallest average grain size.

The in-plane surface morphology (Figure 33 *left pictures*) and corresponding 3D views (Figure 33 *right pictures*) of KNN films with 20% excess of potassium and sodium and 0.2 molar concentration deposited on $Si/SiO_2/TiO_2/Pt$, Al_2O_3/Pt and $SrTiO_3/Pt$ substrates were also analysed by AFM. The smallest average grain size (~334 nm) was also found in KNN films deposited on $Si/SiO_2/TiO_2/Pt$ substrate. For $SrTiO_3/Pt$ substrate it reaches ~469 nm and the highest average grain size (~483 nm) is obtained in the KNN film on Al_2O_3/Pt substrate. The smallest RMS roughness (~16.61 nm) was again calculated for the KNN film on $Si/SiO_2/TiO_2/Pt$ substrate, which is in agreement with the smallest average grain size (Table 11).

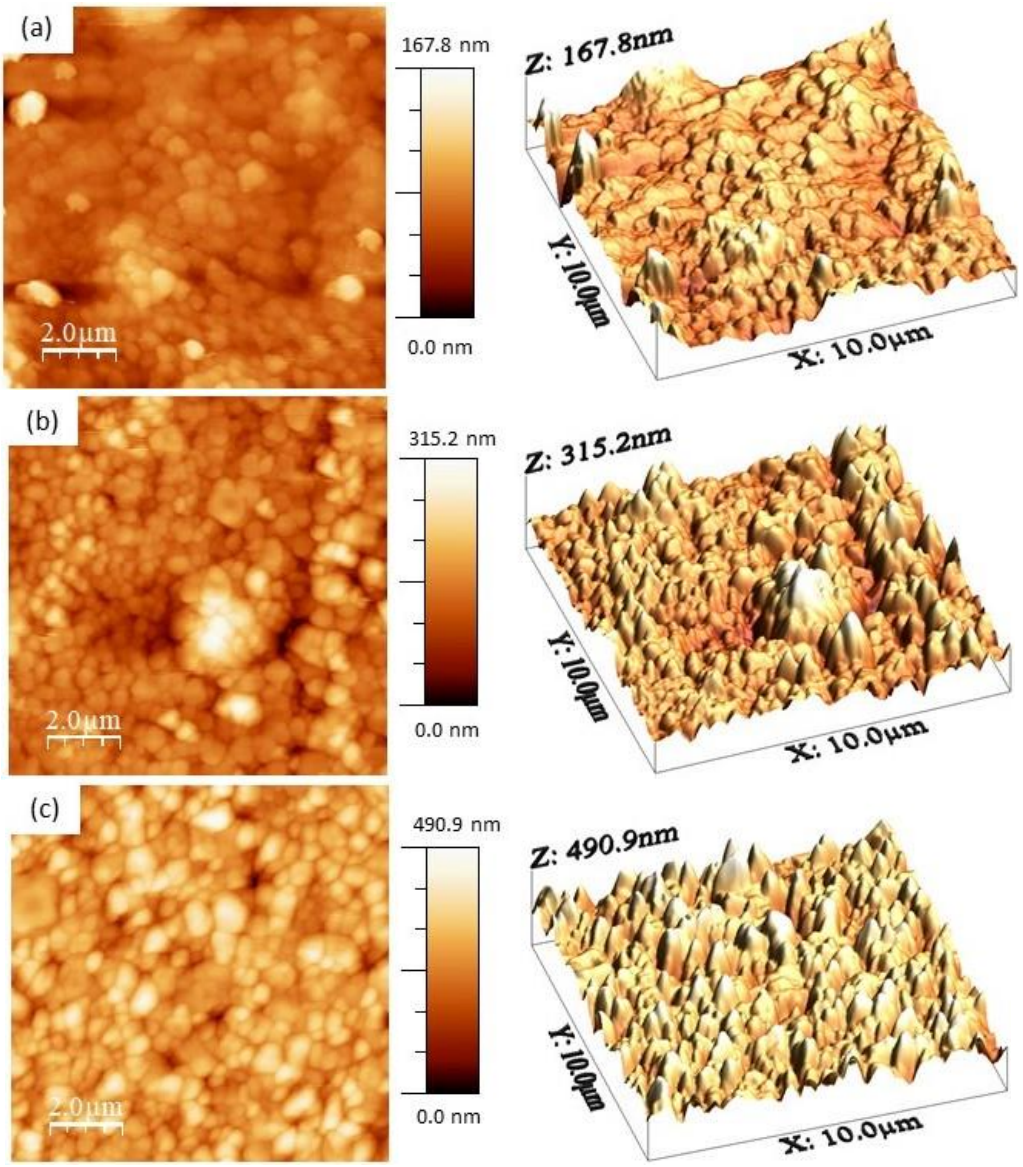

Figure 33- AFM of KNN thin films (20% excess with 0.2 M concentration) deposited on: (a) $Si/SiO_2/TiO_2/Pt$, (b) Al_2O_3/Pt and (c) $SrTiO_3/Pt$ substrates. Scan areas are 10x10 µm.

Figure 34 shows the morphology (*left pictures*) and corresponding 3D views (*right pictures*) of KNN films with 5% excess of potassium and 0.2 molar concentration deposited on $Si/SiO_2/TiO_2/Pt$, Al_2O_3/Pt and $SrTiO_3/Pt$ substrates analysed by AFM. In this case, the smallest average grain size was found in KNN films deposited on Al_2O_3/Pt (~112 nm) and $SrTiO_3/Pt$ (~105 nm) substrates, while the highest average grain size was verified on the KNN film deposited on $Si/SiO_2/TiO_2/Pt$ substrate (~133 nm). The smallest RMS roughness was calculated from the KNN on $Si/SiO_2/TiO_2/Pt$ substrate (~ 8.91 nm) (Table 11).

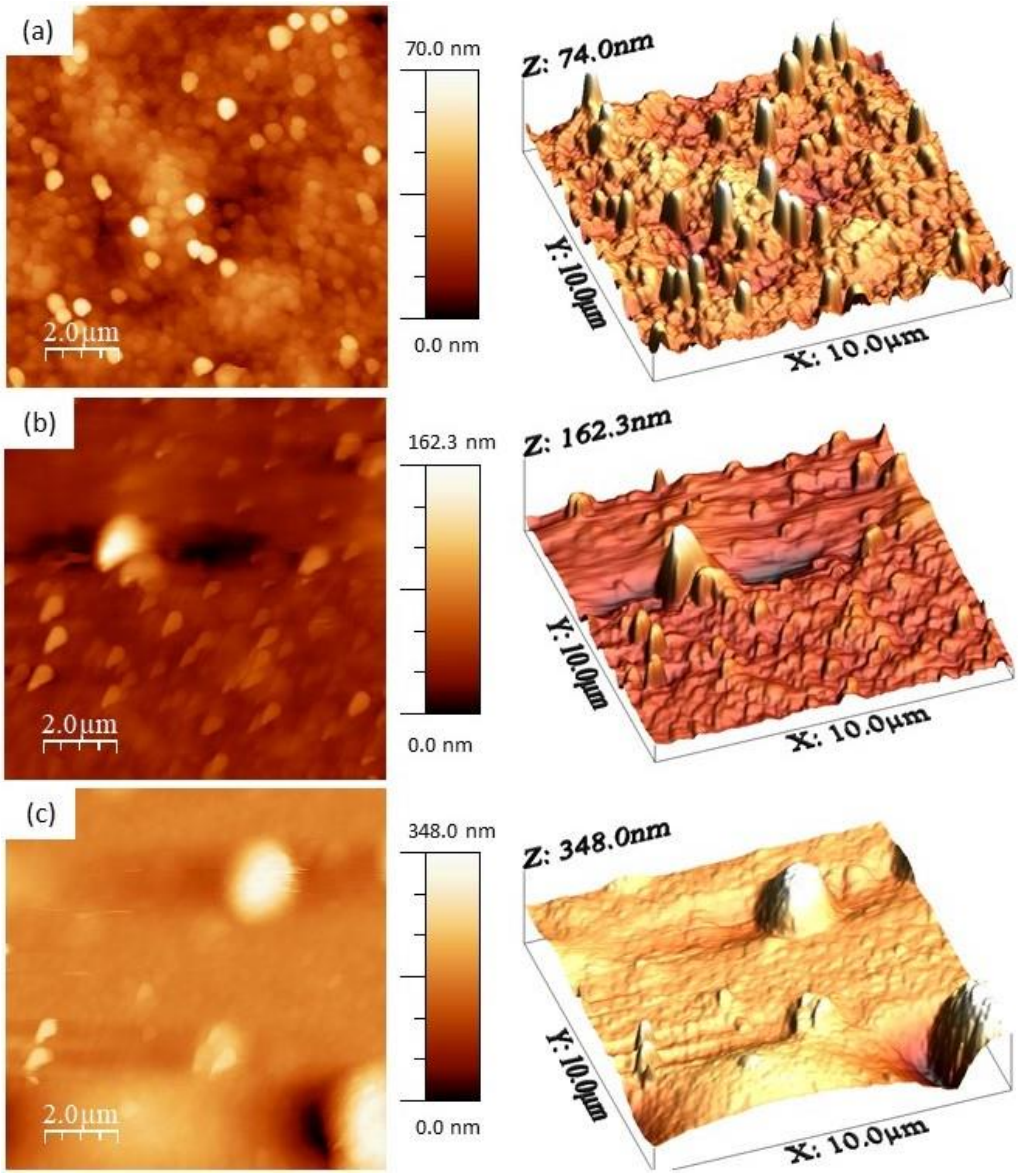

Figure 34- AFM of KNN thin films (5% excess with 0.2 M concentration) deposited on: (a) $Si/SiO_2/TiO_2/Pt$, (b) Al_2O_3/Pt and (c) $SrTiO_3/Pt$ substrates. Scan areas are 10x10 µm.

The analysed KNN films (5% excess of potassium with 0.4 M concentration) deposited on $Si/SiO_2/TiO_2/Pt$ substrates exhibit grains in *x,y,z*-directions (Figure 35 *left pictures*). The RMS roughness of the films was calculated from these AFM micrographs, having ~17.91 nm and is presented in Table 11. The average grain size of the KNN thin film is proximally 247 nm.

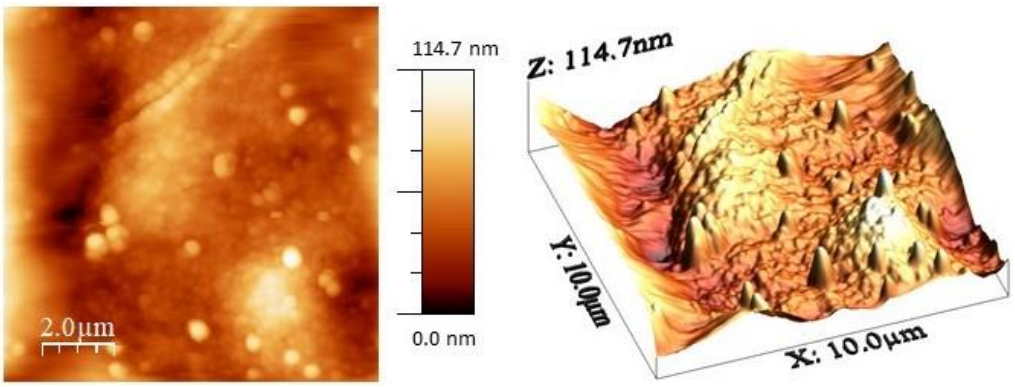

Figure 35- AFM of KNN thin films (5% excess with 0.4 M concentration) deposited on $Si/SiO_2/TiO_2/Pt$ substrate. Scan areas are 10x10 µm.

Table 11 summarizes the average grain size and RMS roughness of KNN thin films deposited on $Si/SiO_2/TiO_2/Pt$, Al_2O_3/Pt and $SrTiO_3/Pt$ substrates. The table shows that the KNN thin films with 20% of excess of potassium and sodium deposited on the $SrTiO_3/Pt$ substrates are those that present higher RMS roughness. With the decreasing of alkali excess, the RMS roughness decreases in the films deposited on $SrTiO_3/Pt$ substrates, becoming higher in the KNN thin films deposited on Al_2O_3/Pt substrate.

Table 11- In-plane average grain size and roughness of KNN films deposited on: $Si/SiO_2/TiO_2/Pt$, Al_2O_3/Pt and $SrTiO_3/Pt$ substrates.

KNN films		Substrate	Average grain size (G) (nm)	RMS roughness (nm)
% Excess	Molar concentration			
20+20	0.4	$SrTiO_3/Pt$	493	44.25
20+20	0.4	Al_2O_3/Pt	603	34.82
20+20	0.4	$Si/SiO_2/TiO_2/Pt$	211	19.46
20+20	0.2	$SrTiO_3/Pt$	469	55.08
20+20	0.2	Al_2O_3/Pt	483	38.20
20+20	0.2	$Si/SiO_2/TiO_2/Pt$	334	16.61
5	0.2	$SrTiO_3/Pt$	105	13.66
5	0.2	Al_2O_3/Pt	112	38.98
5	0.2	$Si/SiO_2/TiO_2/Pt$	133	8.97
5	0.4	$Si/SiO_2/TiO_2/Pt$	247	17.91

4.4. Electrical Properties of KNN Thin Films

4.4.1. Dielectric Properties

Figure 36 shows the frequency dependence of the room-temperature relative permittivity (ε_r) and loss tangent ($tan\delta$) of KNN films with 20% excess of potassium and sodium and 0.4 molar concentration deposited on $Si/SiO_2/TiO_2/Pt$, Al_2O_3/Pt and $SrTiO_3/Pt$ substrates.

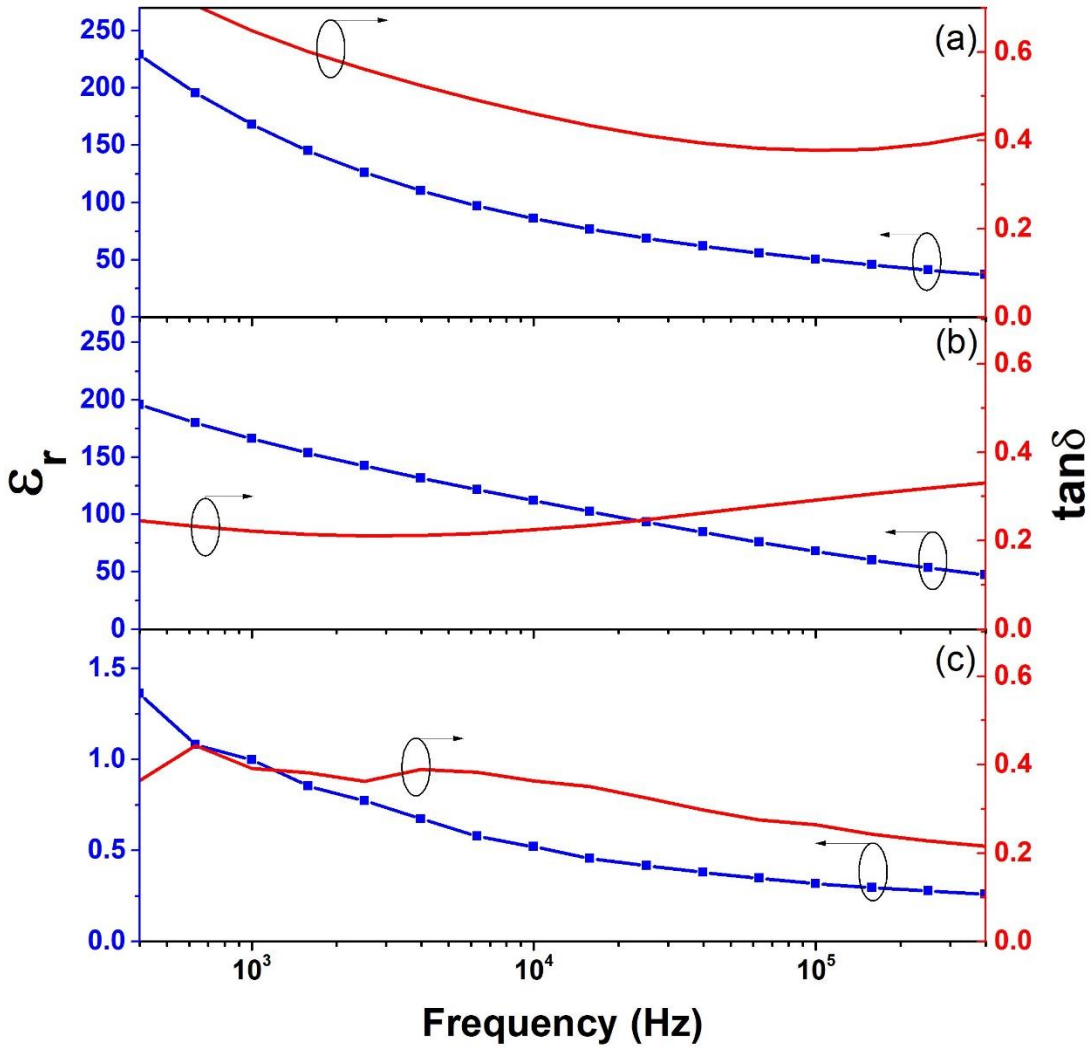

Figure 36- Room-temperature relative permittivity (ε_r) and loss tangent ($tan\delta$) as a function of frequency for KNN thin films with 20% excess and 0.4 molar concentration deposited on: (a) $Si/SiO_2/TiO_2/Pt$, (b) Al_2O_3/Pt and (c) $SrTiO_3/Pt$ substrates.

For KNN films deposited on $Si/SiO_2/TiO_2/Pt$ (Figure 36 (a)) ε_r at 10 kHz is 110 and *tanδ* is 0.46. Elevated loss tangent values were expected in this film, due to the presence of cracks in its microstructure, as it was verified on the top views of the SEM images (Figure 28 (c)).

The KNN film deposited on the Al_2O_3/Pt substrate has relative permittivity ε_r = 111 at 10 kHz and loss tangent *tanδ* = 0.22 at 10 kHz (Figure 36 (b)). These permittivity values are the highest compared with those for the other two films of the same solution and can be explained by the high average grain size of these films, as seen in Table 11.

Regarding the KNN films deposited on $SrTiO_3/Pt$ substrate, it was not possible to measure ε_r values higher than 0.69 at 10 kHz (Figure 36 (c)). These films have high loss tangent (*tanδ* = 0.38 at 10 kHz) when compared to the other films. A possible reason for such poor dielectric response might be in the film microstructure, which consists on columnar grains with grain boundaries extending across the whole film thickness, that could provide conduction pathways [50].

Figure 37 shows the relative permittivity and loss tangent as a function of frequency for KNN films with 20% excess of potassium and sodium and 0.2 molar concentration deposited on $Si/SiO_2/TiO_2/Pt$, Al_2O_3/Pt and $SrTiO_3/Pt$ substrates.

The decrease of the molar concentration from 0.4 to 0.2 in the solution with 20% excess, enhances the relative permittivity and supresses the loss tangent. Thus, the KNN film deposited on $Si/SiO_2/TiO_2/Pt$ has ε_r = 389 and *tanδ* = 0.09 at 10 kHz (Figure 37 (a)). The film on Al_2O_3/Pt has ε_r = 167 and *tanδ* = 0.09 at 10 kHz (Figure 37 (b)). Finally, the film on $SrTiO_3/Pt$ has ε_r = 585 and *tanδ* = 0.18 at 10 kHz (Figure 37 (c)). This might be explained by the fact that the films deposited on $Si/SiO_2/TiO_2/Pt$ substrate do not have cracks and the porosity is smaller in the films deposited on Al_2O_3/Pt and $SrTiO_3/Pt$ substrates (Figure 29). Comparing the dielectric values with the total stress it is verified that the KNN thin film with the lowest loss tangent (KNN thin film deposited on $Si/SiO_2/TiO_2/Pt$ substrate) has a tensile strain (Table 9). The KNN thin films with highest loss tangent (KNN thin film deposited on Al_2O_3/Pt and $SrTiO_3/Pt$ substrates) have a compressive strain (Table 9).

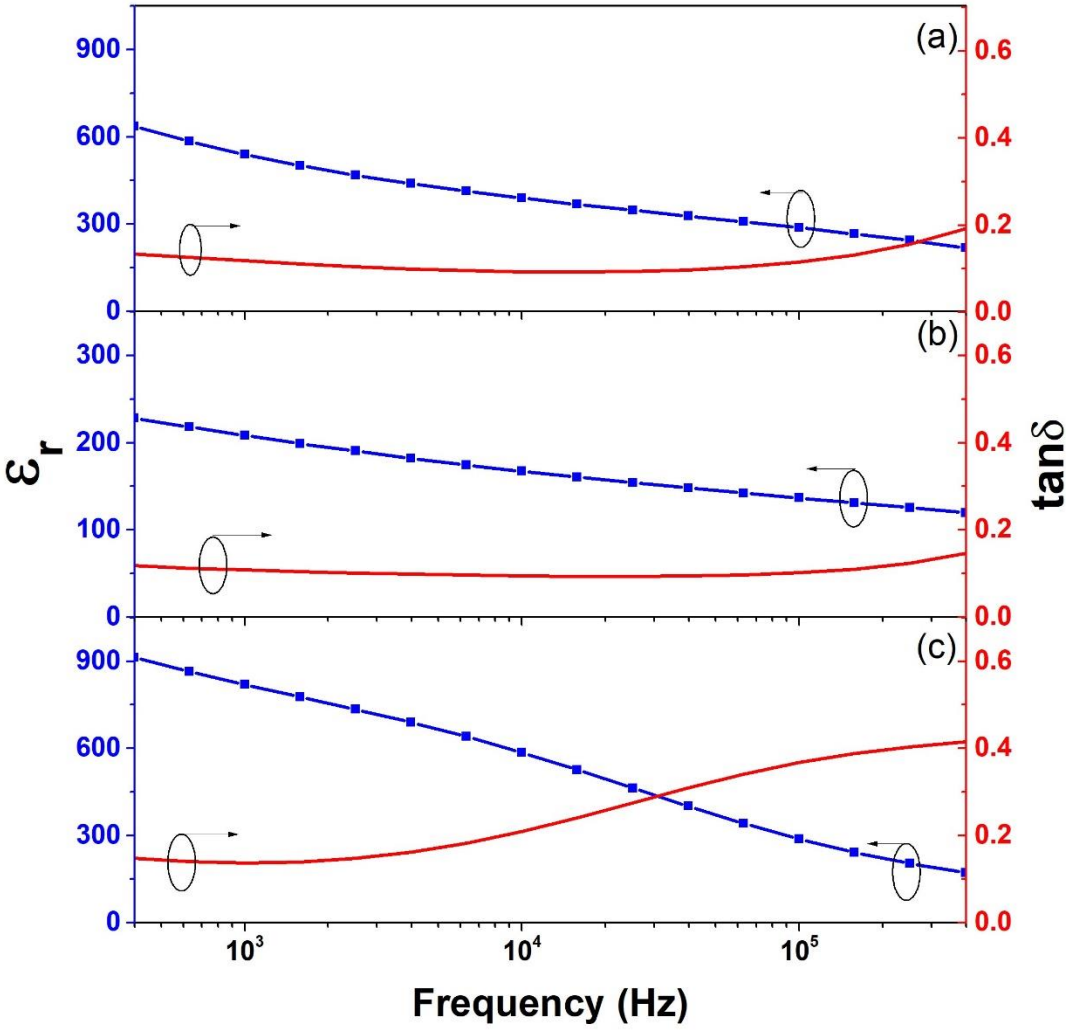

Figure 37- Room temperature relative permittivity (ε_r) and loss tangent ($tan\delta$) as a function of frequency for KNN thin films with 20% excess and 0.2 molar concentration deposited on: (a) $Si/SiO_2/TiO_2/Pt$, (b) Al_2O_3/Pt and (c) $SrTiO_3/Pt$ substrates.

Relative permittivity and loss tangent as a function of frequency is illustrated on Figure 38 for the KNN thin films with 5% excess and 0.2 molar concentration deposited on $Si/SiO_2/TiO_2/Pt$, Al_2O_3/Pt and $SrTiO_3/Pt$ substrates. The film deposited on $Si/SiO_2/TiO_2/Pt$ substrate (Figure 38 (a)) has ε_r = 161 and $tan\delta$ = 0.1 at 10 kHz. KNN films deposited on Al_2O_3/Pt and $SrTiO_3/Pt$ substrates (Figure 38 (b) and (c)) present relative permittivity values of ε_r = 110 and ε_r = 210 at 10 kHz, respectively. Simultaneously, the loss tangent values are $tan\delta$ = 0.36 and $tan\delta$ = 0.16 at 10 kHz, respectively. As in Figure 37, the KNN film with the lower losses (KNN thin film deposited on $Si/SiO_2/TiO_2/Pt$ substrate) presents a tensile strain and the KNN thin films with the highest losses (KNN

thin film deposited on Al_2O_3/Pt and $SrTiO_3$/Pt substrates) have a compressive strain (Table 9).

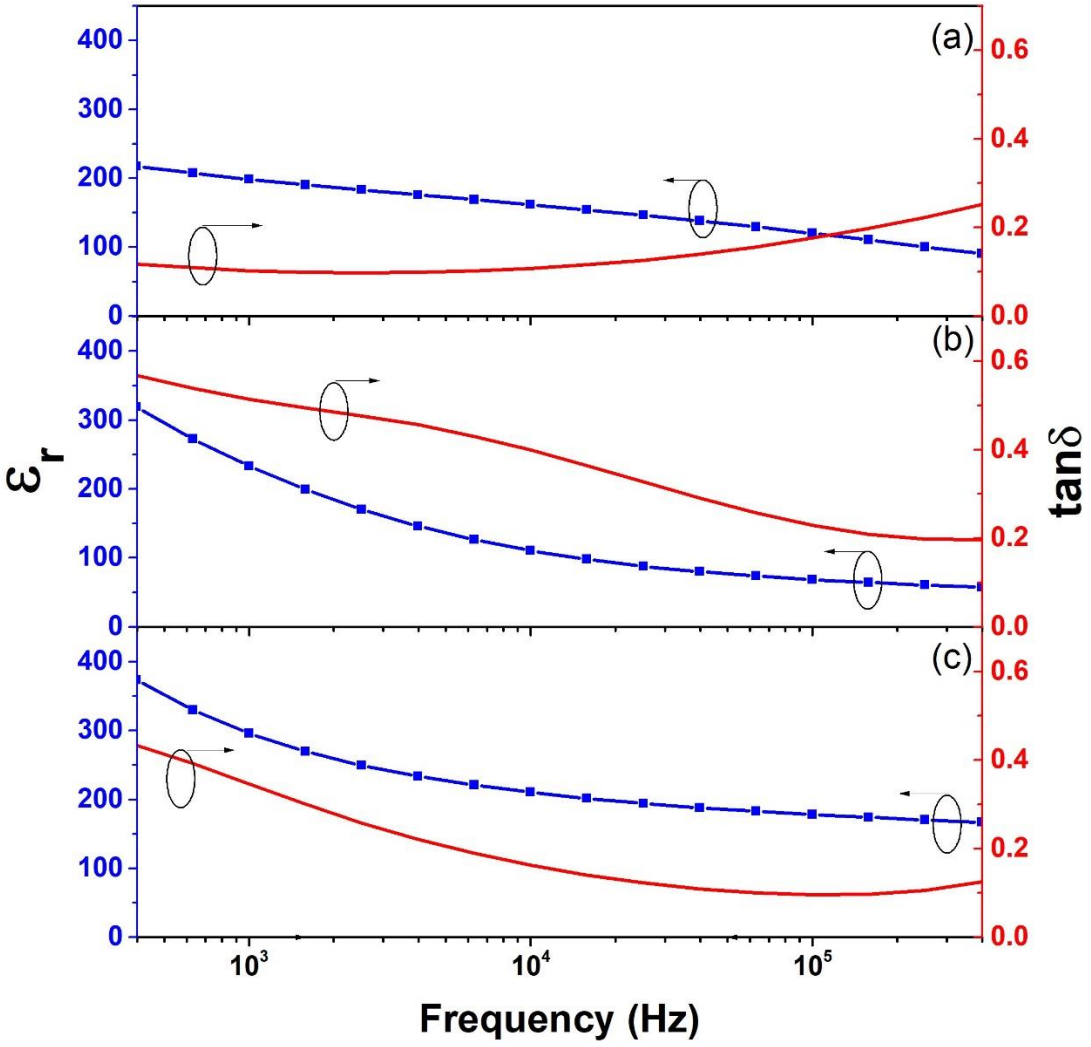

Figure 38- Room temperature relative permittivity (ε_r) and loss tangent ($tan\delta$) as a function of frequency for KNN thin films with 5% excess and 0.2 molar concentration deposited on: (a) Si/SiO_2/TiO_2/Pt, (b) Al_2O_3/Pt and (c) $SrTiO_3$/Pt substrates.

Figure 39 demonstrates the frequency dependence relative permittivity and loss tangent as a function of KNN films with 5% excess of potassium with 0.4 molar concentration deposited on Si/SiO_2/TiO_2/Pt substrates. These KNN films have rather high values of the relative permittivity (ε_r = 183 at 10 kHz) and loss tangent ($tan\delta$ = 0.21 at 10 kHz). These loss tangent values are higher than those for the identical film from the 0.2 M concentration solution, since it was possible to observe the cracks in the films microstructure on the SEM top-view image (Figure 31).

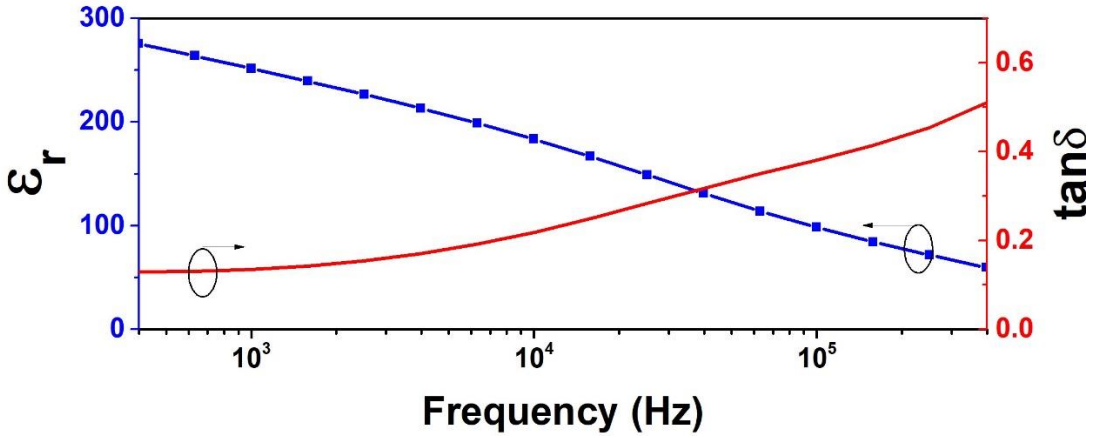

Figure 39- Room-temperature relative permittivity (ε_r) and loss tangent (*tanδ*) as a function of frequency for KNN thin films with 5% excess and 0.4 molar concentration deposited on Si/SiO_2/TiO_2/Pt substrate.

Table 12 summarizes the obtained dielectric properties of KNN thin films with 5% excess of potassium and 20% excess of potassium and sodium with 0.4 and 0.2 molar concentrations.

Table 12- Summary of the room temperature dielectric properties of KNN thin films at 10 kHz.

KNN films		Substrate	ε_r	tanδ
% Excess	Molar concentration			
20+20	0.4	$SrTiO_3$/Pt	-	-
20+20	0.4	Al_2O_3/Pt	111.96	0.224
20+20	0.4	Si/SiO_2/TiO_2/Pt	110.27	0.460
20+20	0.2	$SrTiO_3$/Pt	585.42	0.182
20+20	0.2	Al_2O_3/Pt	167.29	0.094
20+20	0.2	Si/SiO_2/TiO_2/Pt	389.33	0.093
5	0.2	$SrTiO_3$/Pt	210.52	0.163
5	0.2	Al_2O_3/Pt	110.48	0.364
5	0.2	Si/SiO_2/TiO_2/Pt	161.63	0.107
5	0.4	Si/SiO_2/TiO_2/Pt	183.41	0.218

4.4.2. Ferroelectric Characteristics of Films (Hysteresis)

Figure 40 shows the polarization-electric field (*P-E*) dependences measured at 50 Hz and various maximum electric fields on KNN thin films with 20% excess and 0.4 M concentration, 20% excess and 0.2 M concentration, 5% excess and 0.2 M concentration as well as 5% excess and 0.4 M concentration deposited on $Si/SiO_2/TiO_2/Pt$, Al_2O_3/Pt and $SrTiO_3/Pt$ substrates. Since loops are different for different maximum electric fields, the electric field of about 60 kV/cm was chosen as the field at which the loops can be compared, as shown in Figure 41.

The ferroelectric hysteresis loops in the KNN thin films with 20% excess and 0.4 M concentration deposited on $Si/SiO_2/TiO_2/Pt$ and Al_2O_3/Pt substrate are presented in Figure 41 (a). The KNN thin film deposited on $Si/SiO_2/TiO_2/Pt$ substrate has a remnant polarization (P_r) of 5.24 μC/cm^2 with a coercive field (E_c) of 29.32 kV/cm and the KNN thin films deposited on Al_2O_3/Pt substrate present an P_r = 1.26 μC/cm^2 with a E_c = 51.56 kV/cm. No reliable data was obtained for the KNN thin film with 20% excess and 0.4 M concentration deposited on $SrTiO_3/Pt$ substrate. A possible reason for such poor ferroelectric response might be in the film microstructure, which consists on columnar grains with grain boundaries extending across the whole film thickness, that could provide conduction pathways [50].

The *P-E* hysteresis loops of the KNN thin films with 20% excess and 0.2 M concentration deposited on $Si/SiO_2/TiO_2/Pt$, Al_2O_3/Pt and $SrTiO_3/Pt$ substrates exhibit rather irregular ferroelectric hysteresis loops (Figure 41 (b)). The remnant polarization (P_r) of the KNN thin film on $Si/SiO_2/TiO_2/Pt$ substrate is 9.57 μC/cm^2, while the coercive field (E_c) is 36.28 kV/cm, that is considerably high comparing with that of the KNN thin films on Al_2O_3/Pt (P_r = 3.19 μC/cm^2, E_c = 29.23 kV/cm) and $SrTiO_3/Pt$ substrate (P_r = 3.58 μC/cm^2, E_c = 42.68 kV/cm).

The ferroelectric hysteresis loops of the KNN thin films with 5% excess and 0.2 M concentration deposited on $Si/SiO_2/TiO_2/Pt$, Al_2O_3/Pt and $SrTiO_3/Pt$ substrates exhibit very well defined ferroelectric hysteresis loops (Figure 41 (c)), although with some leakage contribution. The KNN thin films on $Si/SiO_2/TiO_2/Pt$ as well as those on Al_2O_3/Pt substrate show values of remnant polarization and coercive field of 1.68 μC/cm^2 and

35.01 kV/cm as well as 2.66 μC/cm^2 and 36.84 kV/cm, respectively. The ferroelectric properties are slightly improved in the KNN thin film with 5% excess and 0.2 M concentration deposited on $SrTiO_3$/Pt substrate, when compared to the values obtained in the film with 20% excess and 0.2 M concentration on the same substrate, reaching P_r = 4.55 μC/cm^2 and E_c = 33.97 kV/cm. Thus, the KNN film with 5% excess and 0.2 M concentration has the lowest remnant polarization (KNN thin film deposited on $Si/SiO_2/TiO_2$/Pt substrate), when it is under tensile in-plane stress, and the KNN thin films with the highest remnant polarization (KNN thin film deposited on Al_2O_3/Pt and $SrTiO_3$/Pt substrates) are under compressive stress (Table 9). Moreover, as higher is the compressive in-plane stress, as higher is the polarisation. That is reasonable, taking into account that for KNN films on $SrTiO_3$/Pt, the lattice of the film is compressed on cooling from growth temperature by the thermal expansion mismatch ($\alpha_{SrTiO3} > \alpha_{KNN}$). Therefore, a tetragonal distortion is induced allowing the niobium (Nb) ionic motions is out-of-plane direction. As result, the dielectric properties of these films are enhanced in the parallel plate capacitor geometry, yielding the maximum polarization.

Figure 41 (d) depicts the polarization (*P*) versus electric field (*E*) dependence measured at 50 Hz and room temperature of KNN thin film with 5% excess and 0.4 molar concentration deposited on $Si/SiO_2/TiO_2$/Pt substrate. The remnant polarization of the KNN thin film is 1.19 μC/cm^2 with a coercive field of 47.09 kV/cm.

The remnant polarization P_r and coercive field E_c of the KNN thin films mentioned above are listed in Table 13.

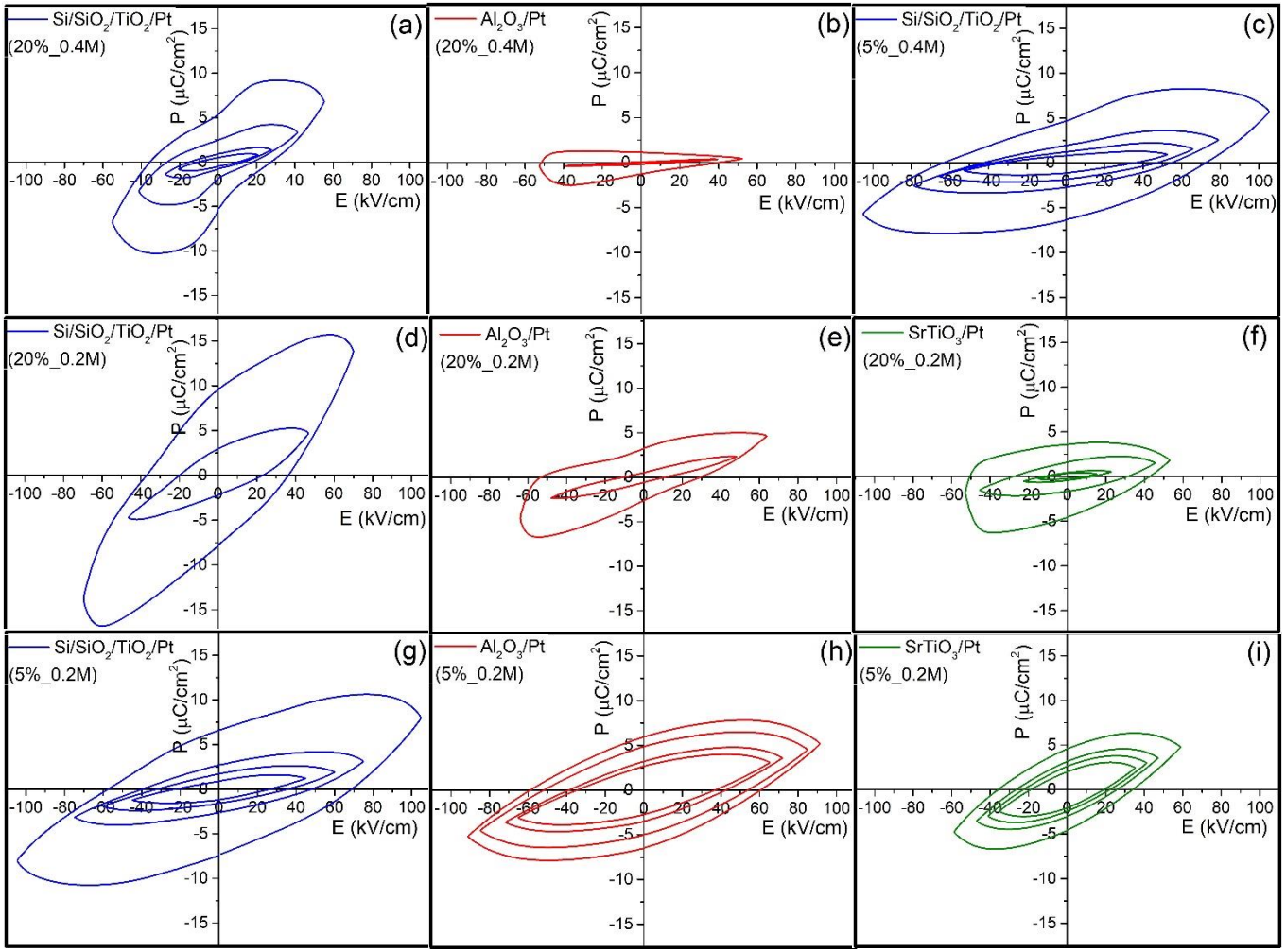

Figure 40- Polarization-electric field (*P-E*) dependence of KNN thin films with (a,b) 20% excess and 0.4 M concentration, (c) 5% excess and 0.4 M concentration, (d-f) 20% excess and 0.2 M concentration, and (g-i) 5% excess with 0.2 M concentration deposited on: (a,c,d,g) $Si/SiO_2/TiO_2/Pt$, (b,e,h) Al_2O_3/Pt and (f,i) $SrTiO_3/Pt$ substrates, measured at 50 Hz and various electric fields.

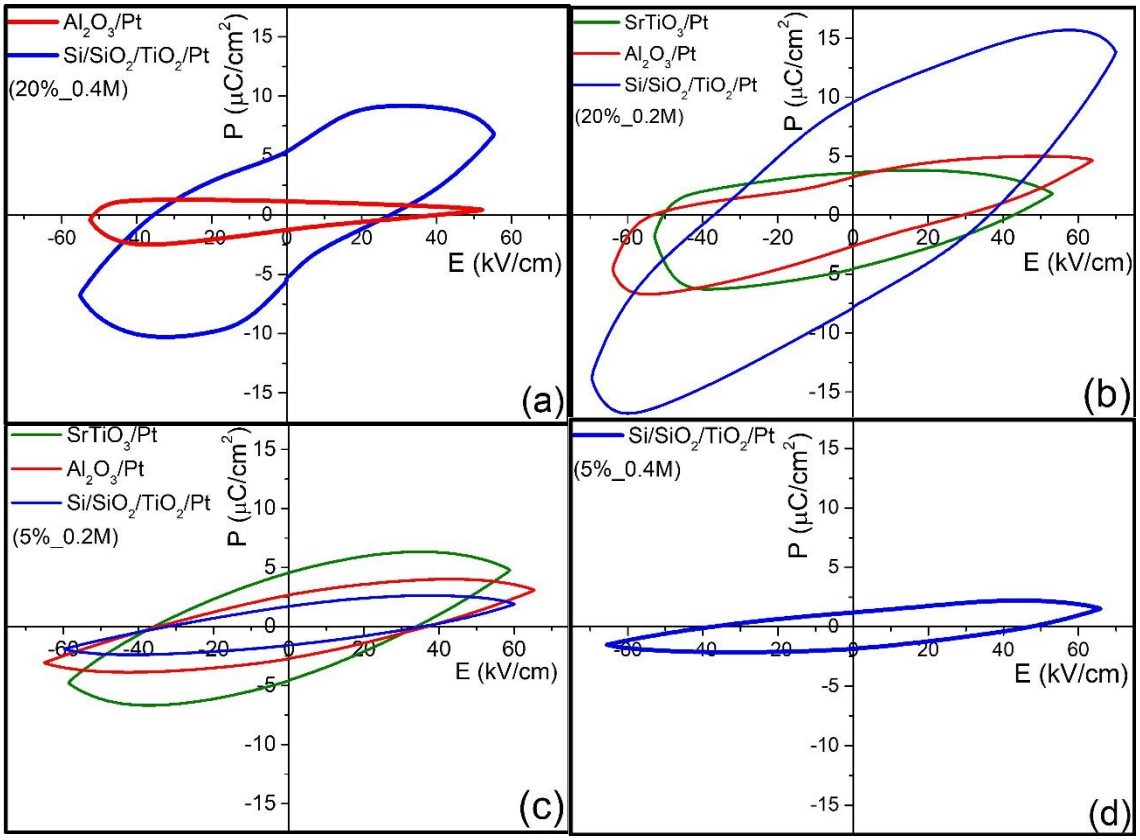

Figure 41- Polarization-electric field (*P-E*) dependence of KNN thin films with (a) 20% excess and 0.4 M concentration, (b) 20% excess and 0.2 M concentration and (c) 5% excess and 0.2 M concentration deposited on $Si/SiO_2/TiO_2/Pt$, Al_2O_3/Pt and $SrTiO_3/Pt$ substrates as well as (d) 5% excess and 0.4 M concentration deposited on $Si/SiO_2/TiO_2/Pt$ substrate, measured at 50 Hz.

Table 13- Remnant polarization (P_r) and coercive field (E_c) of the KNN thin films prepared in this work measured at room temperature, maximum electric field of ~60 kV/cm and frequency of 50 Hz.

KNN films		Substrate	P_r (μC/cm²)	E_c (kV/cm)
% Excess	Molar concentration			
20+20	0.4	$SrTiO_3/Pt$	-	-
20+20	0.4	Al_2O_3/Pt	1.26	51.56
20+20	0.4	$Si/SiO_2/TiO_2/Pt$	5.24	29.32
20+20	0.2	$SrTiO_3/Pt$	3.58	42.68
20+20	0.2	Al_2O_3/Pt	3.19	29.23
20+20	0.2	$Si/SiO_2/TiO_2/Pt$	9.57	36.28
5	0.2	$SrTiO_3/Pt$	4.55	33.97
5	0.2	Al_2O_3/Pt	2.66	36.84
5	0.2	$Si/SiO_2/TiO_2/Pt$	1.68	35.01
5	0.4	$Si/SiO_2/TiO_2/Pt$	1.19	47.09

Figure 42 shows the polarization-electric field (*P-E*) dependence of KNN thin films with 20% excess and 0.4 M concentration on Al_2O_3/Pt, 20% excess with 0.2 M concentration on Al_2O_3/Pt and 5% excess with 0.4 M concentration deposited on Si/SiO_2/TiO_2/Pt substrate, which could sustain applied electric field above 200 kV/cm. These films are the KNN films with the lowest absolute values of induced stress (Table 9). Moreover, the films on Al_2O_3/Pt reveal square-like loops, typical for ferroelectrics, but rarely reported for KNN films. And once again, with application of the higher field, the KNN thin films show increased remnant polarization and coercive field, reaching 9.46 μC/cm^2 and 398.59 kV/cm, respectively, for the KNN film with 20% excess and 0.2 M concentration deposited on Al_2O_3/Pt substrate (Table 14).

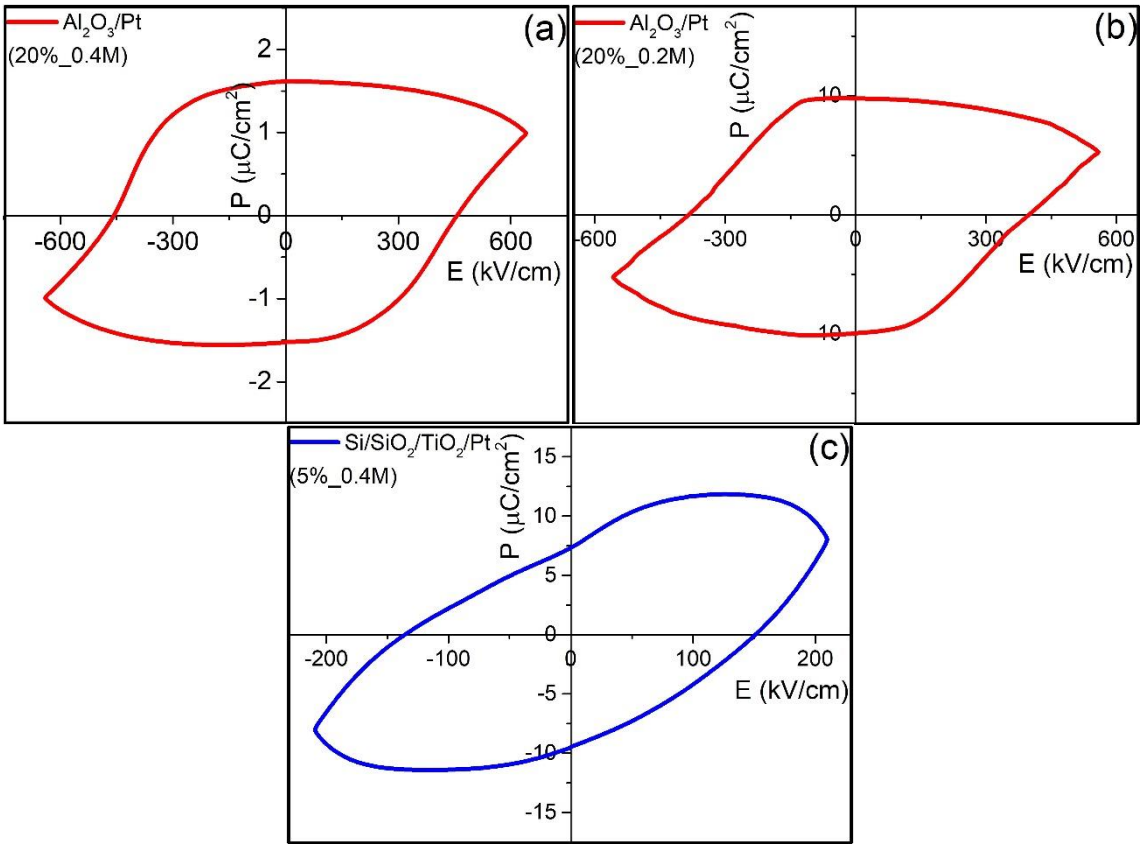

Figure 42- Polarization-electric field (*P-E*) dependence of KNN thin films with: (a) 20% excess and 0.4 M concentration deposited on Al_2O_3/Pt, (b) 20% excess and 0.2 M concentration deposited on Al_2O_3/Pt and (c) 5% excess and 0.4 M concentration deposited on Si/SiO_2/TiO_2/Pt substrate measured at 50 Hz.

Table 14- Maximum remnant polarization (P_r) and coercive field (E_c) of the KNN thin films prepared in this work measured at room temperature and 50 Hz.

KNN films		Substrate	E_{max} (kV/cm)	P_r (μC/cm^2)	E_c (kV/cm)
% Excess	Molar concentration				
20+20	0.4	$SrTiO_3$/Pt	-	-	-
20+20	0.4	Al_2O_3/Pt	669	1.61	456.45
20+20	0.4	Si/SiO_2/TiO_2/Pt	60.06	5.24	29.32
20+20	0.2	$SrTiO_3$/Pt	45.59	1.60	31.14
20+20	0.2	Al_2O_3/Pt	560	9.46	398.59
20+20	0.2	Si/SiO_2/TiO_2/Pt	70.09	9.57	36.28
5	0.2	$SrTiO_3$/Pt	58.96	4.55	33.97
5	0.2	Al_2O_3/Pt	91.62	5.94	60.44
5	0.2	Si/SiO_2/TiO_2/Pt	105.10	6.51	67.85
5	0.4	Si/SiO_2/TiO_2/Pt	200	7.32	150.22

4.4.3. Piezoelectric Force Microscopy Analysis

It is known that the ferroelectric and electromechanical response of a material is directly related to its polar domain structure. In ferroelectric KNN thin films energy minimization results in multiple domains, separated by domains walls. These domain walls have well-defined orientations that minimize energy by maintaining compatibility of strain and polarization across the wall. Thus, particular patterns, also known as domain structures, dictate the effective properties of the crystals.

Piezo-response microscopy (PFM) is a helpful tool to image ferroelectric domains at the nanoscale and to study their switching behaviour. The ferroelectric domains could adopt 60^o, 90^o, 120^o and 180^o domain walls, as in the case of $KNbO_3$ [3][25].

Figure 43 shows the topography images, the piezo-response images and simultaneous cross-sections of topography and PFM taken on KNN thin films with 20% excess of potassium and sodium and 0.4 molar concentration deposited on $SrTiO_3$/Pt substrate. These films exhibit a high percentage of well-defined nanodomains. The bright and dark contrast in PFM images represent the direction of orientation of the polarization vectors in their respective lattices.

The domains are exactly separated by 180^{o} domain walls relating to their polarization vector. This domain wall kind is dominant in most of the lattice grains in the film. The 180^{o} domains have exactly parallel lattices but oppositely oriented polar (fourfold rotation) *c*-axes [86]. The domain length in the PFM image ranges between 0.4 and 1 μm and the average size domain width is about 75 nm. So, these domains can be considered as nanodomains. It was observed from the illustrated images that the PFM contrast is independent of topography effects, indicating that the captured PFM signal has not been influenced by the cross talk with topography signal [25].

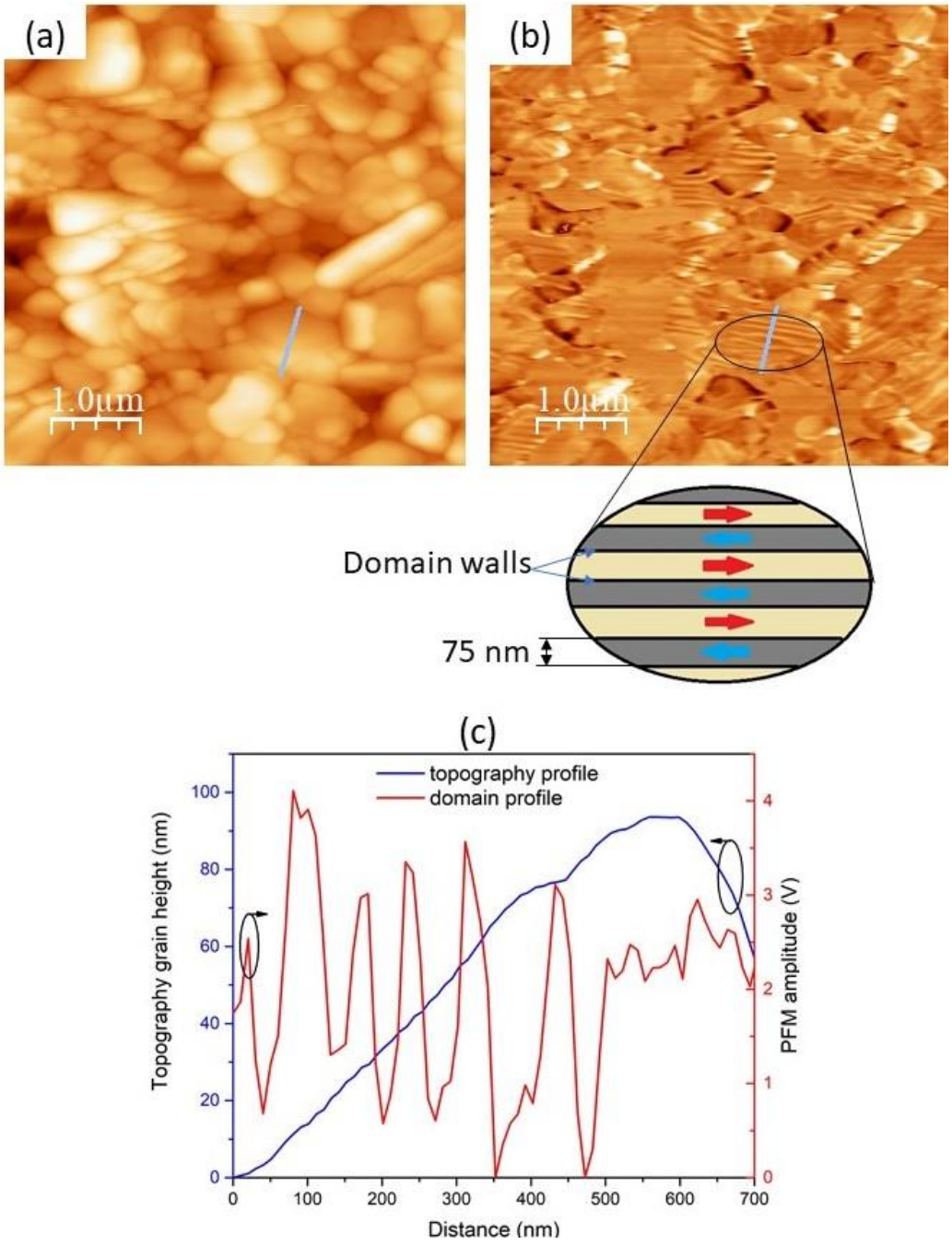

Figure 43- (a) Topography, (b) piezo-force response image and (c) cross-section of topography and PFM (c) taken on KNN thin films with 20% of potassium and sodium excess and 0.4 molar concentration deposited on $SrTiO_3$/Pt substrate.

Figure 44 shows the topography images, the piezo-response images and simultaneous cross-sections of topography and PFM taken on KNN thin films with 20% excess of potassium and sodium and 0.4 molar concentration deposited on Al_2O_3/Pt substrate. These films exhibit a low percentage of well-defined domains. As in Figure 43 it also presents nanodomains. These nanodomains are circled in the figure, the rest are

artefacts of the PFM. The domains are exactly separated by a 180° domain walls, with a wavy shape, characteristic to this type of domain walls [3]. The domain length in the PFM image ranges between 0.5 and 0.75 µm and the average size domain width is about 100 nm.

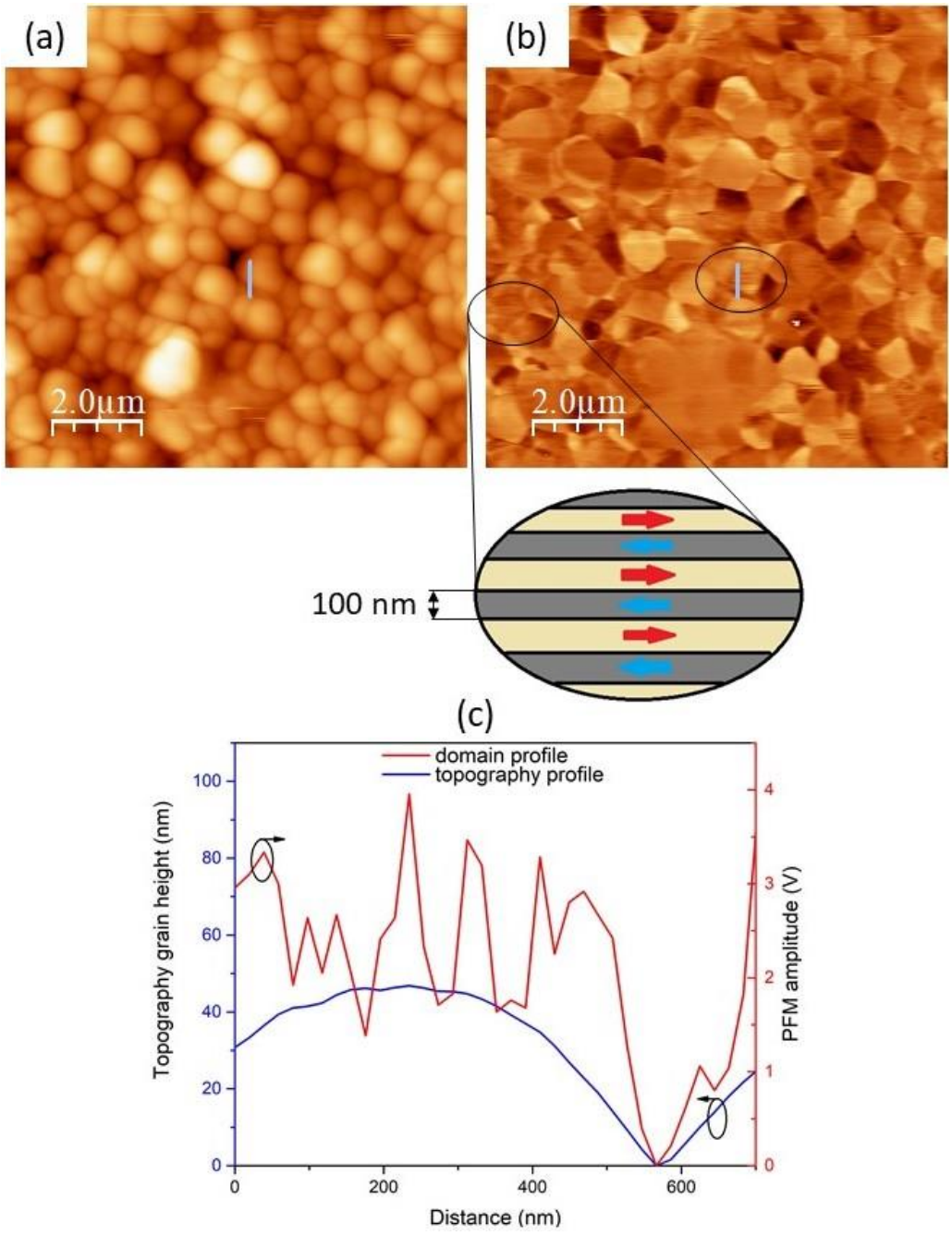

Figure 44- (a) Topography, (b) piezo-force response image and (c) cross-section of topography and PFM, taken on KNN thin films with 20% of potassium and sodium excess and 0.4 molar concentration deposited on Al_2O_3/Pt substrate.

Figure 45 and Figure 46 show topography, out of plane PFM signal and simultaneous cross-sections of topography and PFM taken on KNN thin film with 20% excess of potassium and sodium and 0.2 M concentration deposited on Al_2O_3/Pt and $SrTiO_3$/Pt substrates, respectively. Domain contrasts (deep bright and dark areas) might be found in PFM images (Figure 45 (b) and Figure 46 (b)), which is a sign of significant out-of-plane component of polarization (signed by black solid line). The bright and the dark contrasts in the PFM images represent the direction of orientation of the polarization. In the piezo-response images, dark regions (hereafter referred to as negative domains) correspond to domains with polarization oriented towards substrate, and bright regions (positive domains) to domains with polarization oriented to the film surface. Grains with non-ferroelectric nature or in-plane polarization will exhibit an intermediate grey contrast [84].

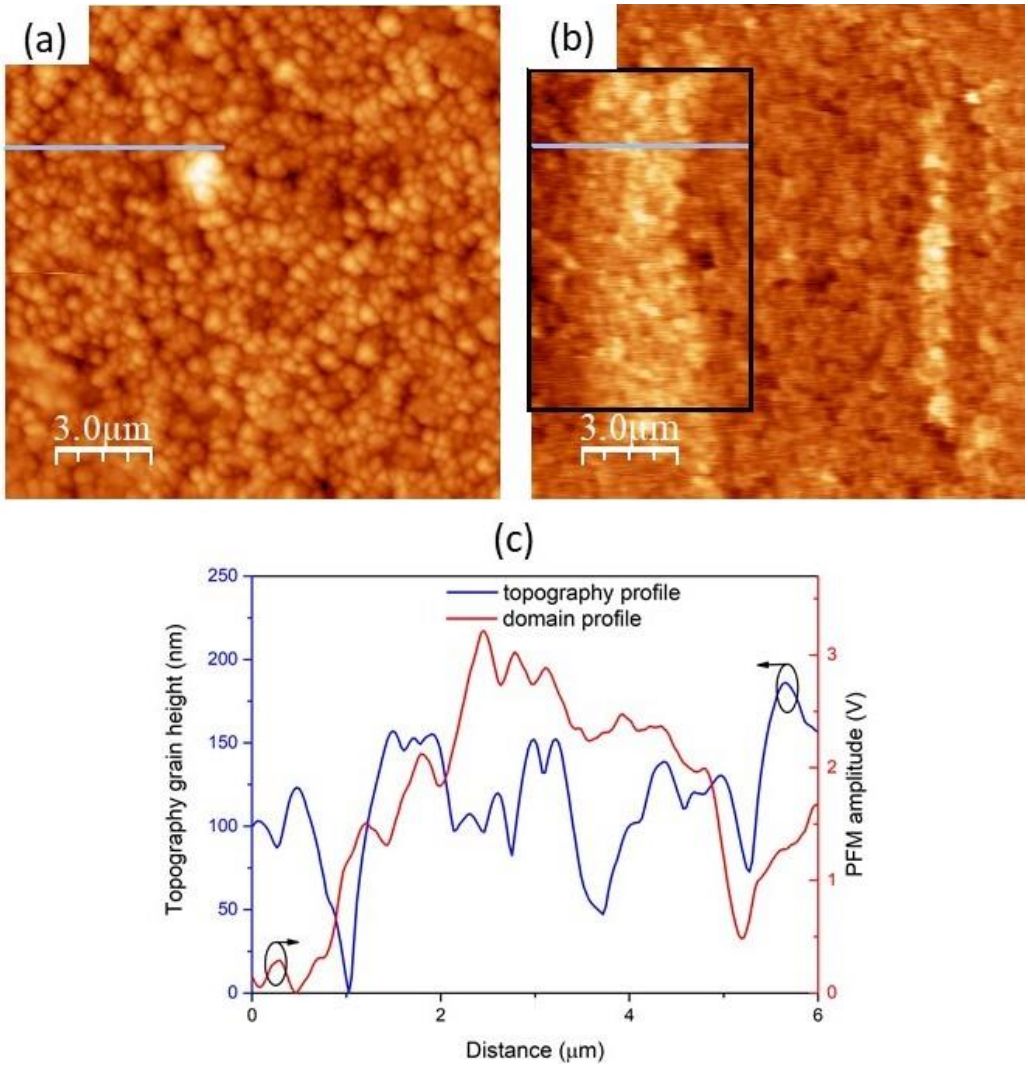

Figure 45- (a) Topography, (b) out of plane PFM signal and simultaneous (c) cross-section of topography and PFM, taken on KNN thin film with 20% excess of potassium and sodium and 0.2 M concentration deposited on Al_2O_3/Pt substrate.

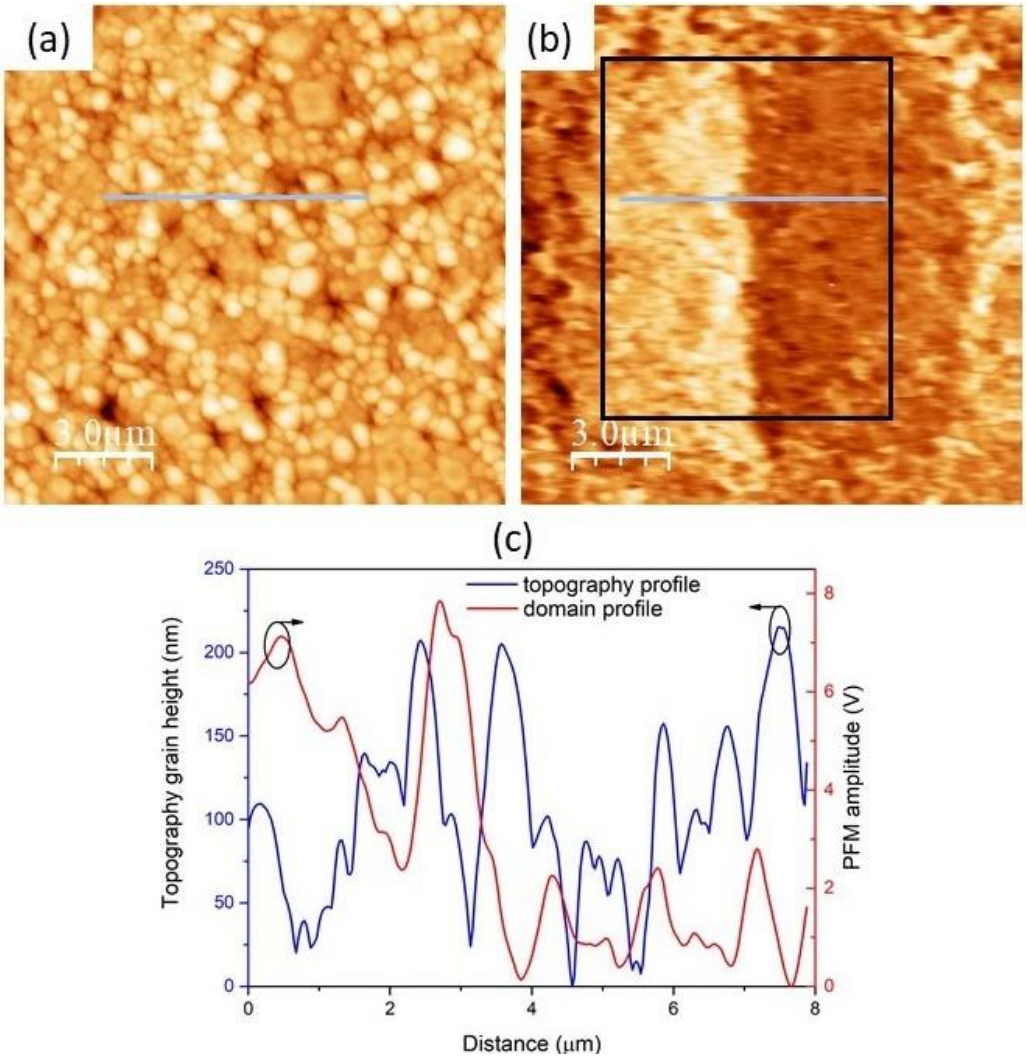

Figure 46- (a) Topography, (b) out of plane PFM signal and simultaneous (c) cross-section of topography and PFM, taken on KNN thin film with 20% excess of potassium and sodium and 0.2 M concentration deposited on $SrTiO_3$/Pt substrate.

Figure 47 and Figure 48 show topography, out-of-plane PFM signal and simultaneous cross-sections of topography and PFM taken on KNN thin film with 5% excess of potassium with 0.2 M concentration deposited on Al_2O_3/Pt and $SrTiO_3$/Pt substrates, respectively.

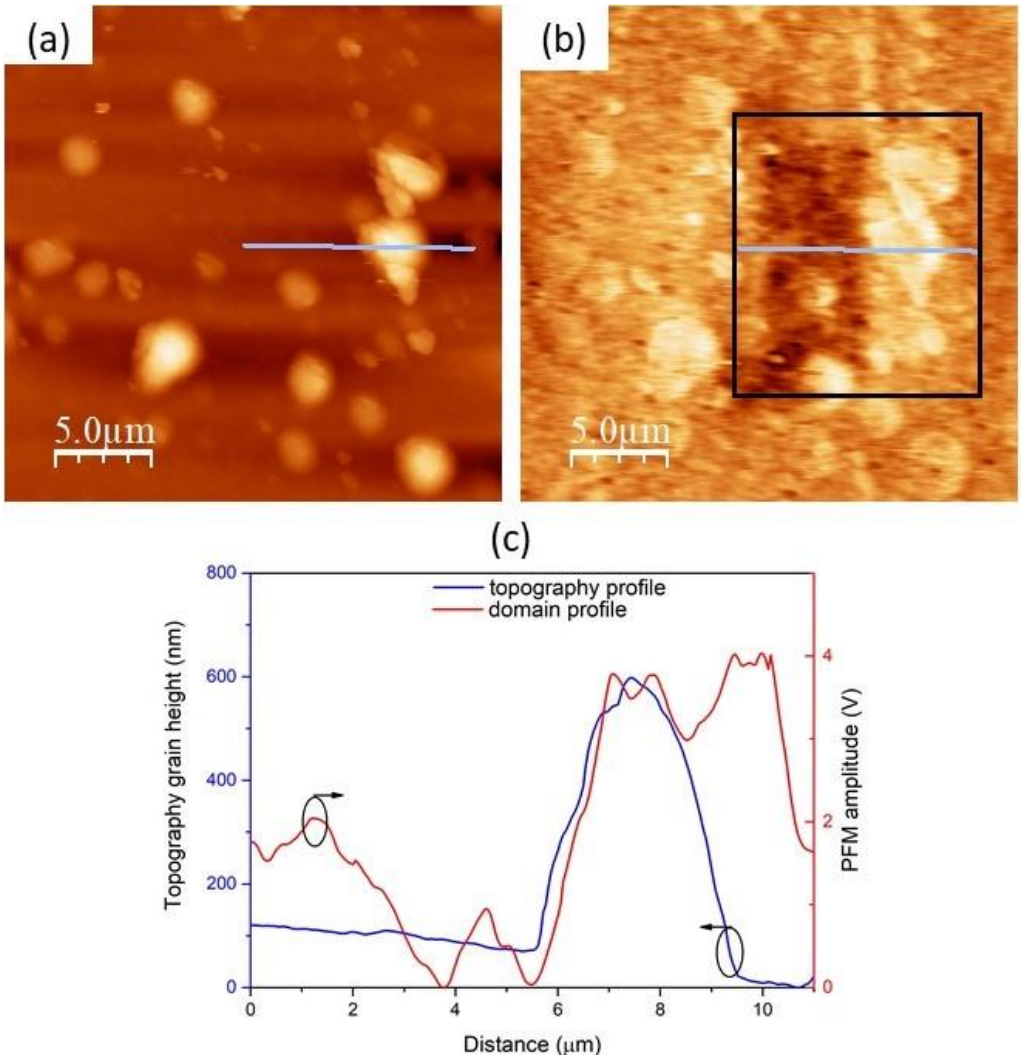

Figure 47- (a) Topography, (b) out of plane PFM signal and simultaneous (c) cross-section of topography and PFM, taken on KNN thin film with 5% excess of potassium and 0.2 M concentration deposited on Al_2O_3/Pt substrate.

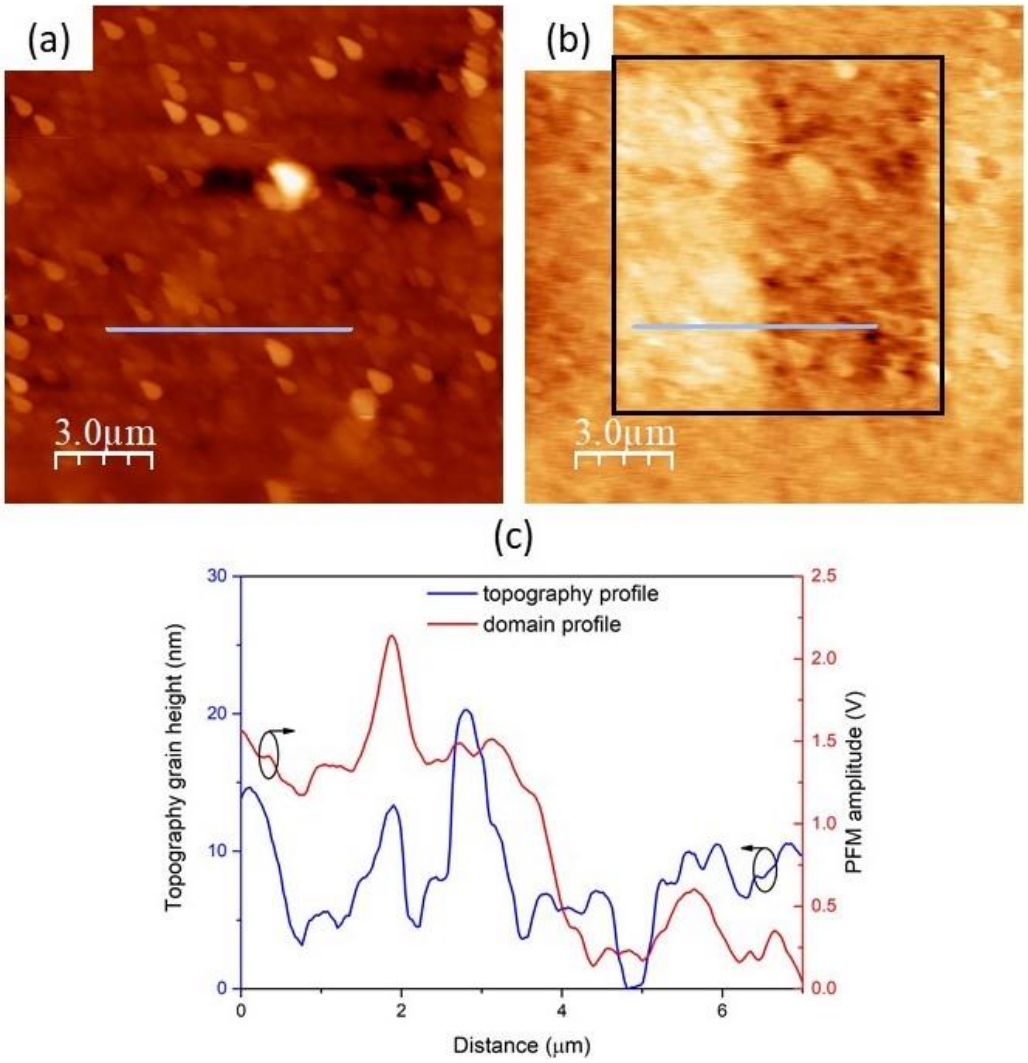

Figure 48- (a) Topography, (b) out of plane PFM signal and simultaneous (c) cross-section of topography and PFM, taken on KNN thin film with 5% excess of potassium and 0.2 M concentration deposited on $SrTiO_3$/Pt substrate.

Figure 49 shows the local piezoresponse hysteresis loops for KNN thin films with 20% excess and 0.2 M concentration deposited on Al_2O_3/Pt substrate, 20% excess and 0.2 M concentration deposited on $SrTiO_3$/Pt substrate, 5% excess and 0.2 M concentration deposited on Al_2O_3/Pt substrate and 5% excess with 0.2 M concentration deposited on $SrTiO_3$/Pt substrate. Thus, all the films are confirmed to possess piezoelectric response.

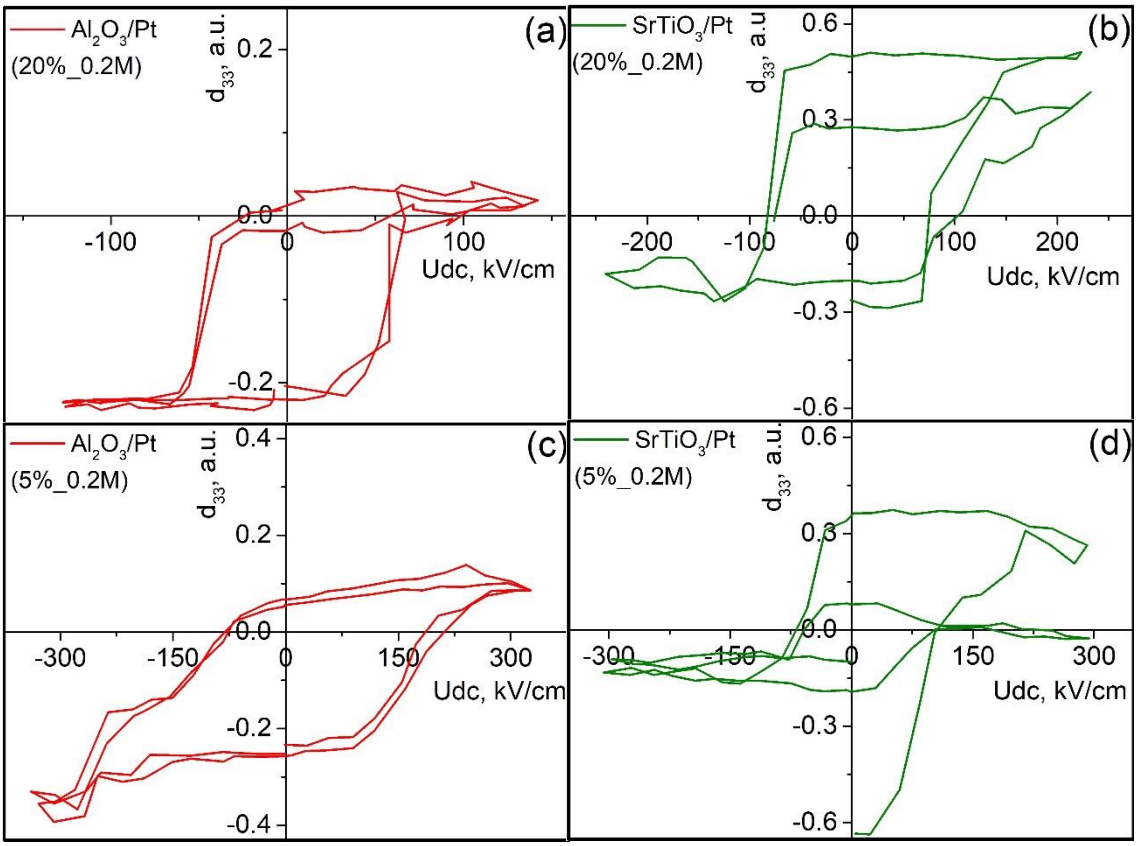

Figure 49- Local piezoresponse hysteresis loops of KNN thin films with (a) 20% excess and 0.2 M concentration deposited on Al_2O_3/Pt substrate, (b) 20% excess and 0.2 M concentration deposited on $SrTiO_3$/Pt substrate, (c) 5% excess and 0.2 M concentration deposited on Al_2O_3/Pt substrate and (d) 5% excess and 0.2 M concentration deposited on $SrTiO_3$/Pt substrate.

4.5. Summary

Table 15 summarizes the properties of KNN thin films prepared in this work. For comparison, the best reported data for KNN thin films fabricated by sol-gel technique are also included. All the films analysed by XRD have a pseudo-cubic structure (a=b=c). In some of the KNN thin films, such as the ones deposited on Al_2O_3/Pt and $SrTiO_3$/Pt substrates, the intensity of the (100) reflection was relatively high because the surface energy of the (100) plane of KNN is relatively low compared to the other planes. Thus, these KNN thin films exhibit a preferred (100) orientation. The KNN films deposited on Al_2O_3/Pt and $SrTiO_3$/Pt substrates have moderate and high compressive stress values, respectively, while the KNN films deposited on Si/SiO_2/TiO_2/Pt substrate have significant tensile total stress values. This happens because Si substrates have a TEC value twice

lower than that of KNN and induce a tensile stress at cooling from the annealing to room temperature. Films that have a compressive stress, as the case of $SrTiO_3$, have TEC values twice higher than that of KNN. Between the compressive films with the same excess of potassium and sodium, the KNN thin films deposited on $SrTiO_3$/Pt substrates have the highest compressive stress. These KNN thin films show the highest thickness, RMS roughness and the lowest average grain size. In contrast, the films with tensile stress on $Si/SiO_2/TiO_2$/Pt substrate have the smallest average grain size.

Regarding the electrical measurements, the highest dielectric permittivity in this work is 585 with loss tangent of 0.182 at 10 kHz, while the lowest loss tangent is 0.093 with permittivity of 389 at 10 kHz obtained for KNN films with 20% alkali excess and 0.2 M concentration deposited on $SrTiO_3$/Pt and $Si/SiO_2/TiO_2$/Pt substrates, respectively. These values are comparable with the literature results (ε_r = 614 with $tan\delta$ = 0.015 at 1 kHz [50]; ε_r = 725 with $tan\delta$ = 0.09 at 1 kHz [51]) presented in Table 15 as well.

The values deduced from the ferroelectric measurements of KNN films used in this study are approximately the same as those reported in the existing bibliography. Values of P_r = 8 μC/cm^2 with E_c = 80 kV/cm [50] and P_r = 9.1 μC/cm^2 with E_c = 80 kV/cm [51] are presented in the literature, while the highest values reported in this study are P_r = 9.57 μC/cm^2 with E_c = 36 kV/cm for KNN films with 20% alkali excess and 0.2 M concentration deposited on $Si/SiO_2/TiO_2$/Pt substrate and P_r = 9.46 μC/cm^2 with E_c = 399 kV/cm for KNN films with 20% alkali excess and 0.2 M concentration deposited on Al_2O_3/Pt.

Comparing the values obtained in the dielectric measurements with the total stress of the films with the same excess and molar concentration, it is possible to verify that the KNN thin films under high compressive strain present higher permittivity and losses when compared to the KNN thin films under tensile or moderate compressive strain.

Comparing the values obtained in the ferroelectrics measurements with the total stress for the films with 5% excess and 0.2 M concentration (with the same applied field, Figure 41 (c)), it is possible to verify that KNN film deposited on $SrTiO_3$/Pt substrate presenting the highest compressive strain has the highest remnant polarization (P_r). Moreover, the ferroelectric measurements presented indicate that all the studied films

on the platinized substrates have ferroelectric characteristics, with the exception of the KNN thin film with 20% excess and 0.4 M concentration deposited on $SrTiO_3$/Pt substrates.

However, observing PFM images, it is verified that this film as well as most of the of KNN thin films exhibit a high percentage of well-defined domains, which is possibly associated to a ferroelectric behaviour. Hysteresis loop measurements carried out by PFM confirm the piezoelectric response of the films. Only the KNN thin films with 20% excess and 0.4 M concentration deposited on both Al_2O_3/Pt and $SrTiO_3$/Pt substrates, which have the highest Lotgering factor values ($f_{(100)}$ = 71.9% and $f_{(100)}$ = 75.09%, respectively), present nanodomains.

Table 15- Properties of KNN thin films prepared in this work and reported in the literature. *Performed at this work.

Excess (%)	Molar concentration	Substrate	Nr. layers	Lattice parameter (Å)	(f_{100})	Total stress (GPa)	Thickness (nm)	RMS roughness (nm)	G (nm)	ε_r at room temperature and 10 kHz	tanδ at 10 kHz	P_r at 50 Hz ($\mu C/cm^2$)	Ec (kV/cm)	Ref.
20+20	0.4	$SrTiO_3$/Pt	5	~4.013 ± 0.002	75.09	-2.55	399	44	493	-	-	-	-	*
20+20	0.4	Al_2O_3/Pt	5	~4.012 ± 0.004	71.90	-0.55	381	35	603	111	0.224	1.61	456	*
20+20	0.4	Si/SiO_2/TiO_2/Pt	5	~3.941 ± 0.015	15.59	3.30	420	19	211	110	0.460	5.24	29	*
20+20	0.2	$SrTiO_3$/Pt	10	~4.028 ± 0.007	54.93	-2.33	329	55	469	585	0.182	1.60	31	*
20+20	0.2	Al_2O_3/Pt	10	~4.017 ± 0.004	38.64	-0.89	312	38	483	167	0.094	9.46	399	*
20+20	0.2	Si/SiO_2/TiO_2/Pt	10	~3.949 ± 0.017	17.40	1.15	214	17	334	389	0.093	9.57	36	*
5	0.2	$SrTiO_3$/Pt	10	~4.006 ± 0.006	15.03	-1.22	382	14	105	211	0.163	4.55	34	*
5	0.2	Al_2O_3/Pt	10	~4.000 ± 0.0009	12.77	-1.02	424	39	112	110	0.364	5.94	60	*
5	0.2	Si/SiO_2/TiO_2/Pt	10	~3.957±0.001	15.85	0.66	333	9	133	162	0.107	6.51	68	*
5	0.4	Si/SiO_2/TiO_2/Pt	5	~3.970±0.007	1.74	0.17	379	18	247	183	0.218	7.32	150	*
5	0.4	Si/SiO_2/TiO_2/Pt	4	-	37	-	250	-	50	614 at 1 kHz	0.015	8 at 1 kHz	80	[50]
2+8	0.35	Si/SiO_2/TiO_2/Pt	4	-	-	-	250	5.36	~300	725 at 1 kHz	0.09	9.1 at 1 kHz	80	[51]

5. Conclusions and Future Work

The main conclusions of this dissertation can be summarized as follows:

- KNN thin films prepared from solutions with i) 20% of K and 20% Na excess and 0.4 M concentration; ii) 20% of K and 20% Na excess and 0.2 M concentration as well as iii) 5% excess of K excess and 0.2 M concentration, were obtained by sol-gel method and found to possess the perovskite structure without secondary phases.
- KNN thin films with 20% of K and 20% Na excess and 0.4 M concentration and KNN thin films with 20% of K and 20% Na excess and 0.2 M concentration deposited on Al_2O_3/Pt and $SrTiO_3$/Pt substrates show (100) preferred orientation with values of $f_{(100)} > 38\%$.
- KNN thin films deposited on Si/SiO_2/TiO_2/Pt substrates have a tensile strain, while KNN thin films deposited on Al_2O_3/Pt and $SrTiO_3$/Pt substrates reveal a compressive strain. Si substrates have TEC values twice lower than that of KNN, naturally inducing a tensile stress at cooling from the annealing to room temperature. Al_2O_3/Pt and $SrTiO_3$/Pt substrates have TEC values higher than that of KNN, therefore inducing a compressive in-plane stress.
- Amongst the films deposited with 20% excess of K and Na and 0.2 M concentration, the KNN films deposited on Si/SiO_2/TiO_2/Pt substrates present the lowest *tanδ* values with the highest P_r values.
- However, among the KNN films deposited with 5% excess of K with 0.2 M concentration, the films with the lowest P_r values are the KNN films deposited on Si/SiO_2/TiO_2/Pt substrates (tensile strain) and the highest P_r values are found in the KNN films deposited on $SrTiO_3$/Pt substrates (highest compressive strain). As a result, variation of the polarization can be achieved by controlling the strain/stress level on the films via the choice of the substrate.

- The PFM images show that KNN films deposited on Al_2O_3/Pt and $SrTiO_3$/Pt substrates have well-defined nanometre scale domains when prepared with 0.4 M concentration and micrometre scale domains when obtained with 0.2 M concentration. The piezoelectric nature of the films is confirmed as well by local measurements.

For future work:

- Study the temperature dependence of the permittivity and loss tangent, of ferroelectric loops for the films and try to establish a correlation between this measurement and the stress obtained.
- Use other deposition techniques such as RF-magnetron sputtering, pulsed laser deposition (PLD) or metal–organic chemical vapour deposition (MOCVD).

References

[1] E. M. Alkoy and M. Papila, “Microstructural features and electrical properties of copper oxide added potassium sodium niobate ceramics,” *Ceram. Int.*, vol. 36, no. 6, pp. 1921–1927, 2010.

[2] T. H. E. E. Parliament, T. H. E. Council, O. F. The, and E. Union, “Directive 2002/95/EC Of The European Parliament And Of The Council,” *Off. J. Eur. Union*, vol. 4, no. September, pp. 9–19, 2003.

[3] R. López Juárez, O. Novelo Peralta, F. González García, F. Rubio Marcos, and M. E. Villafuerte Castrejón, “Ferroelectric domain structure of lead-free potassium-sodium niobate ceramics,” *J. Eur. Ceram. Soc.*, vol. 31, no. 9, pp. 1861–1864, 2011.

[4] J. Wu, D. Xiao, and J. Zhu, “Potassium-sodium niobate lead-free piezoelectric materials: Past, present, and future of phase boundaries,” *Chem. Rev.*, vol. 115, no. 7, pp. 2559–2595, 2015.

[5] J. F. Li, K. Wang, F. Y. Zhu, L. Q. Cheng, and F. Z. Yao, “(K,Na)NbO_3-based lead-free piezoceramics: Fundamental aspects, processing technologies, and remaining challenges,” *J. Am. Ceram. Soc.*, vol. 96, no. 12, pp. 3677–3696, 2013.

[6] Y. Saito *et al.*, “Lead-free piezoceramics,” *Nature*, vol. 432, no. 7013, pp. 84–87, Nov. 2004.

[7] T. R. Shrout and S. J. Zhang, “Lead-free piezoelectric ceramics: Alternatives for PZT?,” *J. Electroceram*, vol. 19, no. 1, pp. 111–124, 2007.

[8] G. H. Haertling, “Ferroelectric ceramics: history and technology,” *J. Am. Ceram. Soc.*, vol. 82, no. 4, pp. 797–818, 1999.

[9] P. M. Vilarinho, “Functional Materials: properties, processing and applications,” in *Scanning Probe Microscopy: Characterization, Nanofabrication and Device Application of Functional Materials*, P. M. Vilarinho, Y. Rosenwaks, and A. Kingon, Eds. Kluwer Academic Publishers, 2005, pp. 3–33.

[10] A. Moulson and J. Herbert, *“Electroceramics materials, properties, applications.”* New York: John Wiley & Sons, Ltd, 2003.

[11] B. Jaffe, *Non-metallic solids*, vol. 3. New York: Academic Press Inc., 1971.

[12] C. Carter and M. Norton, *Ceramic Materials Science and Engineering*, Second Edi. New York: Springer Science+Business Media, 2001.

[13] E. Soergel, "Visualization of ferroelectric domains in bulk single crystals," *Appl. Phys. B Lasers Opt.*, vol. 81, no. 6, pp. 729–752, 2005.

[14] J. Y. Li, R. C. Rogan, E. Ustündag, and K. Bhattacharya, "Domain switching in polycrystalline ferroelectric ceramics.," *Nat. Mater.*, vol. 4, no. 10, pp. 776–781, 2005.

[15] J. Valasek, "Piezo-electric and allied phenomena in Rochelle salt," *Phys. Rev.*, vol. 17, no. 4, pp. 475–481, 1921.

[16] R. López Juárez and F. González, "Lead-Free Ferroelectric Ceramics with Perovskite Structure," *Ferroelectr. - Mater. Asp.*, pp. 305–330, 2011.

[17] G. Francis, *"Structure, Properties and Preparation Of Perovskite-Type Ccompounds."* Pergamon Press, 1969.

[18] T. Hehn and Y. Manoli, *"CMOS Circuits for Piezoelectric Energy Harvesters,"* vol. 38. Springer Science+Business Media, 2015.

[19] I. Patel, "Advances in Ceramics - Electric and Magnetic Ceramics, Bioceramics, Ceramics and Environment," C. Sikalidis, Ed. Croatia: InTech, 2011, p. 133.

[20] F. Rubio Marcos, A. Del Campo, R. López Juárez, J. J. Romero, and J. F. Fernández, "High spatial resolution structure of (K,Na)NbO_3 lead-free ferroelectric domains," *J. Mater. Chem.*, vol. 22, no. 19, pp. 9714–9720, 2012.

[21] F. Söderlind, P.-O. Käll, and U. Helmersson, "Sol–gel synthesis and characterization of $Na_{0.5}K_{0.5}NbO_3$ thin films," *J. Cryst. Growth*, vol. 281, pp. 468–474, 2005.

[22] B. Malič *et al.*, "Sintering of lead-free piezoelectric sodium potassium niobate ceramics," *Materials (Basel).*, vol. 8, no. 12, pp. 8117–8146, 2015.

[23] J. Rodel, W. Jo, K. T. P. Seifert, E. M. Anton, T. Granzow, and D. Damjanovic, "Perspective on the development of lead-free piezoceramics," *J. Am. Ceram. Soc.*, vol. 92, no. 6, pp. 1153–1177, 2009.

[24] J. G. Fisher, D. Rout, K. S. Moon, and S. J. L. Kang, "Structural changes in potassium sodium niobate ceramics sintered in different atmospheres," *J. Alloys Compd.*, vol. 479, no. 1–2, pp. 467–472, 2009.

[25] M. A. Rafiq, M. E. Costa, and P. M. Vilarinho, “Establishing the Domain Structure of ($K_{0.5}Na_{0.5}$)NbO_3 (KNN) Single Crystals by Piezoforce-Response Microscopy,” *Sci. Adv. Mater.*, vol. 6, no. 3, pp. 426–433, 2014.

[26] R. E. Jeager and L. Egerton, “Hot Pressing of Potassium Sodium Niobates,” *J. Am. Ceram. Soc.*, vol. 45, no. 5, pp. 209–213, 1962.

[27] M. Kosec and D. Kolar, “On Activated Sintering and Electrical Properties of $NaKNbO_3$,” *Mat. Res. Bull*, vol. 10, no. 5, pp. 335–340, 1975.

[28] G. H. Haertling, “Properties of Hot-Pressed Ferroelectric Alkali Niobate Ceramics,” *J. Am. Ceram. Soc.*, vol. 50, no. 6, pp. 329–330, 1967.

[29] L. Egerton and D. M. Dillon, “Piezoelectric and Dielectric Properties of Ceramics in the System Potassium Sodium Niobate,” *J. Am. Ceram. Soc.*, vol. 42, no. 9, pp. 438–442, 1959.

[30] E. Ringgaard and T. Wurlitzer, “Lead-free piezoceramics based on alkali niobates,” *J. Eur. Ceram. Soc.*, vol. 25, pp. 2701–2706, 2005.

[31] B. P. Zhang, J. F. Li, K. Wang, and H. Zhang, “Compositional dependence of piezoelectric properties in $Na_xK_{1-x}NbO_3$ lead-free ceramics prepared by spark plasma sintering,” *J. Am. Ceram. Soc.*, vol. 89, no. 5, pp. 1605–1609, 2006.

[32] J. F. Li, K. Wang, B. P. Zhang, and L. M. Zhang, “Ferroelectric and piezoelectric properties of fine-grained $Na_{0.5}K_{0.5}NbO_3$ lead-free piezoelectric ceramics prepared by spark plasma sintering,” *J. Am. Ceram. Soc.*, vol. 89, no. 2, pp. 706–709, 2006.

[33] B. Malic, J. Bernard, J. Holc, D. Jenko, and M. Kosec, “Alkaline-earth doping in (K,Na)NbO_3 based piezoceramics,” *J. Eur. Ceram. Soc.*, vol. 25, pp. 2707–2711, 2005.

[34] R. Zuo, J. Rödel, R. Chen, and L. Li, “Sintering and Electrical Properties of Lead-Free $Na_{0.5}K_{0.5}NbO_3$ Piezoelectric Ceramics,” *J. Am. Ceram. Soc.*, vol. 89, no. 6, pp. 2010–2015, 2006.

[35] Y. Inagaki, K. ichi Kakimoto, and I. Kagomiya, “Crystal growth and ferroelectric property of $Na_{0.5}K_{0.5}NbO_3$ and Mn-doped $Na_{0.5}K_{0.5}NbO_3$ crystals grown by floating zone method,” *J. Eur. Ceram. Soc.*, vol. 30, no. 2, pp. 301–306, 2010.

[36] J. G. Fisher, A. Benčan, J. Holc, M. Kosec, S. Vernay, and D. Rytz, “Growth of

potassium sodium niobate single crystals by solid state crystal growth," *J. Cryst. Growth*, vol. 303, no. 2, pp. 487–492, 2007.

[37] Y. Inagaki and K. Kakimoto, "Dielectric and Piezoelectric Properties of Mn-Doped $Na_{0.5}K_{0.5}NbO_3$ Single Crystals Grown by Flux Method," *Appl. Phys. Express*, vol. 1, no. 6, p. 61602, 2008.

[38] S.-E. Park and T. R. Shrout, "Ultrahigh strain and piezoelectric behavior in relaxor based ferroelectric single crystals," *J. Appl. Phys.*, vol. 82, no. 4, p. 1804, 1997.

[39] S. Gupta and S. Priya, "Ferroelectric properties and dynamic scaling of <100> oriented $(K_{0.5}Na_{0.5})NbO_3$ single crystals," *Appl. Phys. Lett.*, vol. 98, no. 24, pp. 2011–2014, 2011.

[40] D. Lin, Z. Li, S. Zhang, Z. Xu, and X. Yao, "Dielectric/piezoelectric properties and temperature dependence of domain structure evolution in lead free $(K_{0.5}Na_{0.5})NbO_3$ single crystal," *Solid State Commun.*, vol. 149, no. 39–40, pp. 1646–1649, 2009.

[41] Y. Kizaki, Y. Noguchi, and M. Miyayama, "Defect Control for Superior Properties in $Na_{0.5}K_{0.5}NbO_3$ Single Crystals," *Key Eng. Mater.*, vol. 350, pp. 85–88, 2007.

[42] H. Uršič, A. Benčan, M. Škarabot, M. Godec, and M. Kosec, "Dielectric, ferroelectric, piezoelectric, and electrostrictive properties of $K_{0.5}Na_{0.5}NbO_3$ single crystals," *J. Appl. Phys.*, vol. 107, no. 3, p. 33705, 2010.

[43] J. Luo, W. Sun, Z. Zhou, Y. Bai, Z. J. Wang, and G. Tian, "Domain evolution and piezoelectric response across thermotropic phase boundary in (K, Na)NbO - based epitaxial thin films," *ACS Appl. Mater. Interfaces*, vol. 9, no. 15, pp. 13315–13322, 2017.

[44] G. Li, X. Wu, W. Ren, and P. Shi, "Effect of excessive K and Na on the dielectric properties of $(K,Na)NbO_3$ thin films," *Thin Solid Films*, vol. 548, pp. 556–559, 2013.

[45] Y. Nakashima, W. Sakamoto, and T. Yogo, "Processing of highly oriented $(K,Na)NbO_3$ thin films using a tailored metal-alkoxide precursor solution," *J. Eur. Ceram. Soc.*, vol. 31, no. 14, pp. 2497–2503, 2011.

[46] C. Kang, J. H. Park, D. Shen, H. Ahn, M. Park, and D.-J. Kim, "Growth and characterization of $(K_{0.5}Na_{0.5})NbO_3$ thin films by a sol–gel method," *J. Sol-Gel Sci.*

Technol., vol. 58, no. 1, pp. 85–90, 2010.

[47] C. Weng, C. Tsai, C. Hong, and C. Lin, "Effects of Non-Stoichiometry on the Microstructure , Oxygen Vacancies , and Electrical Properties of KNN-Based Thin Films," *J. State Sci. Technol.*, vol. 5, no. 9, pp. 49–56, 2016.

[48] C. W. Ahn, S. Y. Lee, H. J. Lee, J. S. Bae, E. D. Jeong, and J. S. Choi, "The effect of K and Na excess on the ferroelectric and piezoelectric properties of $K_{0.5}Na_{0.5}NbO_3$ thin film," *J. Phys. D. Appl. Phys.*, vol. 42, no. 5, p. 215304, 2009.

[49] L. Wang, K. Yao, G. C. Phoi, and W. Ren, "Volatilization of alkali ions and effects of molecular weight of polyvinylpyrrolidone introduced in solution-derived ferroelectric $K_{0.5}Na_{0.5}NbO_3$ films," *J. Mater. Res*, vol. 24, no. 12, pp. 3516–22, 2009.

[50] A. Kupec, B. Malic, J. Tellier, E. Tchernychova, S. Glinsek, and M. Kosec, "Lead-free ferroelectric potassium sodium niobate thin films from solution: Composition and structure," *J. Am. Ceram. Soc.*, vol. 95, no. 2, pp. 515–523, 2012.

[51] K. Tanaka, H. Hayashi, K. I. Kakimoto, H. Ohsato, and T. Iijima, "Effect of (Na,K) - Excess Precursor Solutions on Alkoxy-Derived (Na,K)NbO_3 Powders and Thin Films," *Jpn. J. Appl. Phys.*, vol. 46, no. 10 B, pp. 6964–6970, 2007.

[52] X. Yan, W. Ren, X. Wu, P. Shi, and X. Yao, "Lead-free (K,Na)NbO_3 ferroelectric thin films : Preparation , structure and electrical properties," *J. Alloys Compd.*, vol. 508, no. 1, pp. 129–132, 2010.

[53] M. Blomqvist *et al.*, "High-performance epitaxial $Na_{0.5}K_{0.5}NbO_3$ thin films by magnetron sputtering sputtering," *Appl. Phys. Lett.*, vol. 81, no. 2, pp. 2000–2003, 2002.

[54] S. Khartsev, A. Grishin, J. Andrèasson, J. H. Koh, and J.-S. Song, "Comparative Characteristics of $Na_{0.5}K_{0.5}NbO_3$ Films on Pt by Pulsed Laser Deposition and Magnetron Sputtering," *Integr. Ferroelectr.*, vol. 55, pp. 769–779, 2003.

[55] J. Ryu *et al.*, "Fabrication and ferroelectric properties of highly dense lead-free piezoelectric $(K_{0.5}Na_{0.5})NbO_3$ thick films by aerosol deposition," *Appl. Pysics Lett.*, vol. 90, no. 152901, pp. 0–3, 2007.

[56] D. G. Schlom, L.-Q. Chen, C.-B. Eom, K. M. Rabe, S. K. Streiffer, and J.-M. Triscone, "Strain Tuning of Ferroelectric Thin Films," *Annu. Rev. Mater. Res.*, vol. 37, no. 1,

pp. 589–626, 2007.

[57] W. Merz, “The Effect of Hydrostatic Pressure on the Curie Point of Barium Titanate Single Crystals,” *Phys. Rev.*, vol. 78, pp. 52–54, 1950.

[58] J. C. Slater, “The lorentz correction in barium titanate,” *Phys. Rev.*, vol. 78, no. 6, pp. 748–761, 1950.

[59] W. Chang *et al.*, “Influence of strain on microwave dielectric properties of (Ba,Sr)TiO_3 thin films,” *J. Appl. Phys.*, vol. 87, no. 6, p. 3044, 2000.

[60] S. T. Zhang, A. B. Kounga, E. Aulbach, H. Ehrenberg, and J. Rödel, “Giant strain in lead-free piezoceramics $Bi_{0.5}Na_{0.5}TiO_3$-$BaTiO_3$-$K_{0.5}Na_{0.5}NbO_3$ system,” *Appl. Phys. Lett.*, vol. 91, no. 11, p. 112906, 2007.

[61] S. Zhang *et al.*, “Lead-free piezoceramics with giant strain in the system $Bi_{0.5}Na_{0.5}TiO_3$–$BaTiO_3$–$K_{0.5}Na_{0.5}NbO_3$. I. Temperature dependent properties,” *J. Appl. Phys.*, vol. 103, no. 3, p. 34108, 2008.

[62] S. E. Park and T. R. Shrout, “Characteristics of relaxor-based piezoelectric single crystals for ultrasonic transducers,” *IEEE Trans. Ultrason. Ferroelectr. Freq. Control*, vol. 44, no. 5, pp. 1140–1147, 1997.

[63] K. Uchino, “Materials issues in design and performance of piezoelectric actuators: an overview,” *Acta Mater.*, vol. 46, no. 11, pp. 3745–3753, 1998.

[64] Y. M. Chiang, G. W. Farrey, and A. N. Soukhojak, “Lead-free high-strain single-crystal piezoelectrics in the alkaline-bismuth-titanate perovskite family,” *Appl. Phys. Lett.*, vol. 73, no. 25, pp. 3683–3685, 1998.

[65] X. Ren, “Large electric-field-induced strain in ferroelectric crystals by point-defect-mediated reversible domain switching,” *Nat. Mater.*, vol. 3, no. 2, pp. 91–94, 2004.

[66] L. Freund and S. Suresh, *Thin Film Materials: Stress, Defect Formation and Surface Evolution*. University of Cambridge Press, 2003.

[67] T. R. Taylor *et al.*, “Impact of thermal strain on the dielectric constant of sputtered barium strontium titanate thin films,” *Appl. Phys. Lett.*, vol. 80, no. 11, pp. 1978–1980, 2002.

[68] C. L. Canedy, H. Li, S. P. Alpay, L. Salamanca-Riba, A. L. Roytburd, and R. Ramesh, “Dielectric properties in heteroepitaxial $Ba_{0.6}Sr_{0.4}TiO_3$ thin films: Effect of internal

stresses and dislocation-type defects," *Appl. Phys. Lett.*, vol. 77, no. 11, pp. 1695–1697, 2000.

[69] I. B. Misirlioglu, A. L. Vasiliev, M. Aindow, S. P. Alpay, and R. Ramesh, "Threading dislocation generation in epitaxial (Ba,Sr)TiO_3 films grown on (001) $LaAlO_3$ by pulsed laser deposition," *Appl. Phys. Lett.*, vol. 84, no. 10, p. 1742, 2004.

[70] M. W. Chu *et al.*, "Impact of misfit dislocations on the polarization instability of epitaxial nanostructured ferroelectric perovskites," *Nat. Mater*, vol. 3, no. 2, pp. 87–90, 2004.

[71] S. P. Alpay, I. B. Misirlioglu, V. Nagarajan, and R. Ramesh, "Can interface dislocations degrade ferroelectric properties?," *Appl. Phys. Lett.*, vol. 85, no. 11, pp. 2044–2046, 2004.

[72] O. Okhay, "Strontium titanate based films for tunable device applications," Universidade de Aveiro, 2009.

[73] N. A. Pertsev, A. G. Zembilgotov, and A. K. Tagantsev, "Effect of Mechanical Boundary Conditions on Phase Diagrams of Epitaxial Ferroelectric Thin Films," *Phys. Rev. Lett.*, vol. 80, no. 9, pp. 2–5, 1998.

[74] N. A. Pertsev, A. G. Zembilgotov, S. Hoffmann, R. Waser, and A. K. Tagantsev, "Ferroelectric thin films grown on tensile substrates: Renormalization of the Curie – Weiss law and apparent absence of ferroelectricity," *J. Appl. Phys.*, vol. 85, p. 1698, 1999.

[75] R. J. Snyder and L. Robert, "Introduction to X-ray Powder Diffractometry." John Wiley and Sons, New York, 1996.

[76] M. E. Fitzpatrick, A. T. Fry, P. Holdway, F. A. Kandil, J. Shackleton, and L. Suominen, "Determination of Residual Stresses by X-ray Diffraction," Teddington, Middlesex, United Kingdom, 2005.

[77] A. Guinier and G. Fournet, "Small-Angle Scattering of X-rays." John Wiley and Sons, New York, 1955.

[78] B. D. Cullity, *Elements of X-Ray Diffraction*, 2nd ed. London: Addison-Wesley, 1978.

[79] P. J. Withers and H. K. D. H. Bhadeshia, "Residual stress Part 1 – Measurement techniques," *Mater. Sci. Technol.*, vol. 17, no. April, pp. 355–365, 2001.

[80] J. B. Noyan, Ismail C. and Cohen, *Residual stress determination by Diffraction-Measurement and Interpretation*. New York, 1987.

[81] P. E. West, *Introduction to Atomic Force Microscopy*. Pacific Nanotechnology, Inc, 2007.

[82] A. B. Milhim, "Development of a Lead − free Piezoelectric (K,Na)NbO_3 Thin Film Deposited on Nickel − based Electrodes," Mechanical and Industrial Engineering University of Toronto, 2016.

[83] A. Techologies I., "Agilent Basics of Measuring the Dielectric Properties of Materials," *Agil. Techologies, Inc.*, 2006.

[84] J. Gao, "Sol-Gel (Ba_xSr_{1-x})TiO_3 Thin Films for Microelectronic Applications," Universidade de Aveiro, 2007.

[85] M. J. Dejneka, C. L. Chapman, and S. T. Misture, "Strong, Low Thermal Expansion Niobate Ceramics," *J. Am. Ceram. Soc.*, vol. 94, no. 8, pp. 2273–2275, 2011.

[86] S. Cheng, N. Ho, and H. Lu, "Transformation-Induced Twinning: The 90^o and 180^o Ferroelectric Domains in Tetragonal Barium Titanate," *J. Am. Ceram. Soc.*, vol. 89, no. 7, pp. 2177–2188, 2006.